8-2016

Additive manufacturing of carbon fiber-reinforced thermoplastic composites

Nicholas M. DeNardo
Purdue University

Recommended Citation

PURDUE UNIVERSITY
GRADUATE SCHOOL
Thesis/Dissertation Acceptance

This is to certify that the thesis/dissertation prepared

By Nicholas M. DeNardo

Entitled
ADDITIVE MANUFACTURING OF CARBON FIBER-REINFORCED THERMOPLASTIC COMPOSITES

For the degree of Master of Science in Materials Science Engineering

Is approved by the final examining committee:

R. B. Pipes
Chair

Jeffrey P. Youngblood

Rodney W. Trice

To the best of my knowledge and as understood by the student in the Thesis/Dissertation Agreement, Publication Delay, and Certification Disclaimer (Graduate School Form 32), this thesis/dissertation adheres to the provisions of Purdue University's "Policy of Integrity in Research" and the use of copyright material.

Approved by Major Professor(s): R. B. Pipes

Approved by: David F. Bahr   6/13/2016

Head of the Departmental Graduate Program   Date

ADDITIVE MANUFACTURING OF CARBON FIBER-

REINFORCED THERMOPLASTIC COMPOSITES

A Thesis

Submitted to the Faculty

of

Purdue University

by

Nicholas M. DeNardo

In Partial Fulfillment of the

Requirements for the Degree

of

Master of Science in Materials Science Engineering

August 2016

Purdue University

West Lafayette, Indiana

Dedicated to my family that made the Purdue journey possible, and the lifelong friends that made it unforgettable.

ACKNOWLEDGMENTS

I would like to express sincere appreciation to my adviser Dr. R. Byron Pipes, a true leader in the composites field with unparalleled insight, intellect, and experience. I am certain that his recent development of the Indiana Manufacturing Institute will become a world class composites research facility and location for industry-academia collaborations. I would also like to thank my committee members Dr. Rodney Trice and Dr. Jeffrey Youngblood, who provided valuable education and instruction during my Purdue years. Special recognition is also given to my team members Anthony Favaloro, Eduardo Barocio, and Bastian Brenken, the most brilliant minds I have ever worked with. Beginning this project and taking it to where we are today was possible only because of the synergies of our team. I know that these three gentlemen will continue to produce fantastic work and excel in their future endeavors. Lastly, I would like to acknowledge Purdue University, where in addition to receiving an extraordinary education, I was able to participate in international community service projects, pursue passions in entrepreneurship and venture capital, and develop advanced additive manufacturing equipment.

TABLE OF CONTENTS

LIST OF TABLES

LIST OF FIGURES

ABSTRACT

DeNardo, Nicholas M. M.S. MSE, Purdue University, August 2016. Additive Manufacturing of Carbon Fiber-Reinforced Thermoplastic Composites. Major Professor: Dr. R. Byron Pipes.

Additive manufacturing, or 3D printing, encompasses manufacturing processes that construct a geometry by depositing or solidifying material only where it is needed in the absence of a mold. The ability to manufacture complex geometries on demand directly from a digital file, as well as the decreasing equipment costs due to increased competition in the market, have resulted in the AM industry experiencing rapid growth in the past decade. Many companies have emerged with novel technologies well suited to improve products and/or save costs in various industries.

Until recently, the applications of polymer additive manufacturing have been mainly limited to prototyping. This can be attributed to multiple factors, namely the high cost of the machines and materials, long print times, and anisotropy of printed parts. In addition, the low unit cost and cycle time of competing processes such as injection molding further skew the economics in favor of other processes. The addition of fiber-reinforcement into polymers used in additive manufacturing processes significantly increases the strength of parts, and also allows larger parts to be manufactured. In 2014, large-scale additive manufacturing of fiber-reinforced polymers was pioneered, and has generated significant attention from both academia and industry. Commercial machines that incorporate high throughput extruders on gantry systems are now available. New applications that require high temperature polymers with low coefficients of thermal expansion and high stiffness are being targeted, for example tooling used in the manufacturing of composite components. The state of the art of

this new paradigm in additive manufacturing as well as the target applications will be discussed in detail.

Many new challenges arise as AM scales and reinforced polymers are incorporated. One of the most notable challenges is the presence of large temperature gradients induced in parts during the manufacturing process, which lead to residual stresses and sometimes detrimental warpage. The current solution to this problem has been to print faster in order to lessen the temperature gradients, however very high extrusion speeds are likely not ideal for achieving optimal material properties. The high shear rates induce further damage to fibers, and entrapped air during the extrusion process may not escape, leading to high void content. Another significant challenge is overcoming the anisotropy in printed parts, which arises due to the stiff reinforcing fibers orienting primarily in the print direction. This complicates the use in demanding applications such as composite tooling, where high stiffness and low CTE are desirable in all directions.

In 2014, a group of graduate students at Purdue University was formed to develop a better understanding of large-scale additive manufacturing processes incorporating high temperature and high fiber content polymer composites. The team spent more than one year designing, developing, and optimizing a lab-scale system that offers full control over all processing parameters, and has begun studying the relevant phenomena and developing models to predict the outcome of printing processes.

This thesis will summarizes the system development process, printing process, composite tooling applications, as well as the mechanical, structural, and viscoelastic properties of printed materials, making it one of the most comprehensive documents written in large-scale additive manufacturing of fiber-reinforced polymers to date. The properties of 50 weight percent carbon fiber-reinforced PPS, a material of high interest in the field, will be presented in detail. The viscoelastic properties will be measured and discussed in the context of both stress relaxation during the printing process and the required performance metrics of composite tooling. A summary of the major results and recommendations can be found in chapter 7.

CHAPTER 1. INTRODUCTION

In this chapter, additive manufacturing is defined, and some of the advantages and disadvantages of the various technologies are briefly outlined. The motivation for adding fiber-reinforcement is discussed, and the decision to ultimately develop an additive manufacturing system for fiber-reinforced polymers based on fused deposition modeling is justified. Next, the state of the art in fused deposition modeling of reinforced polymers is detailed, with previous works in both small-scale and large-scale being summarized. Recent commercial ventures and target applications of large-scale fused deposition modeling are also discussed. Lastly, the motivation for and objectives of a newly developed Purdue University additive manufacturing team are outlined. The group has fully designed and developed a lab-scale fused deposition modeling system and will research and model the relevant phenomena in this exciting new paradigm in additive manufacturing.

1.1 Additive Manufacturing

1.1.1 Motivation

Additive Manufacturing, also referred to as AM or 3D printing, emerged approximately 30 years ago as a technology poised to alter the future of manufacturing. Originally used for prototyping, AM now has far reaching applications, including manufacturing end use products. Unlike traditional manufacturing methods, AM builds complex geometries in the absence of a mold through depositing or solidifying material only where it is needed. In AM, a 3D geometry is converted into a set of directions that a machine follows to build the part in a layer-by-layer process. This capability translates to AM achieving superior economies of scale and scope

compared to traditional manufacturing technologies [1]. A single AM machine can produce nearly any geometry, while doing so economically at low volumes.

The advantages of AM over traditional subtractive manufacturing processes (i.e. machining) include substantially less material waste, greater geometric flexibility, and greater simplicity. Scrap rates as high as 80-90% are not uncommon in machining, making AM very attractive for aerospace and defense applications requiring expensive materials such as titanium [1]. In addition, component designs can be optimized to take advantage of the advanced non-solid infill structures only obtainable using an AM process. Non-solid infills allow the lightweighting of various components, which can be very valuable to certain industries such as aerospace where weight is incredibly costly. By reducing the weight of an aircraft flying international routes by 25 pounds, approximately $440,000 in cost savings can be achieved per year [1].

Injection molding and casting processes require very large capital investments in inflexible tooling having long lead times. The cost of tooling often makes up the largest percentage of the unit cost in a molded part. As a result, minimum order quantities often exceeding one thousand parts are required to make most applications financially feasible. The entire design process from idea generation to final part delivery often exceeds months, primarily due to mold design and manufacturing. As a result, AM is a strong contender for low volume applications where the cost of tooling cannot be distributed over thousands or tens of thousands of parts. In addition, since AM does not require a mold, parts can be manufactured immediately upon order. For this reason, utilizing AM to produce products can result in shorter lead times than a process utilizing injection molding, even though the cycle times in injection molding are far shorter than AM.

1.1.2 Comparison of Polymer Additive Manufacturing Methods

Current AM technologies are compatible with ceramics, metals, polymers, and composites, however this work will focus on AM of composites. A major objective of this work was to design and develop a lab-scale composites AM system capable of

processing high temperature and high fiber content reinforced polymers, summarized in chapter 2. All of the polymer AM methods were first considered prior to designing and developing the system in order to determine which would be most appropriate for this objective. The most prominent polymer AM technologies at the time the system was developed are illustrated in figure 1.1 [2]. Each of these technologies are summarized below, and the ultimate decision to choose fused deposition modeling, or FDM, is justified in section 1.1.3.
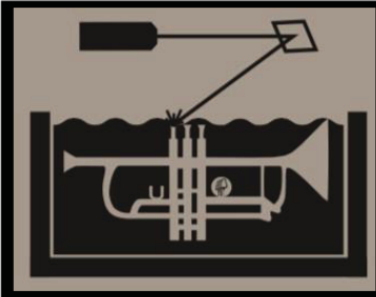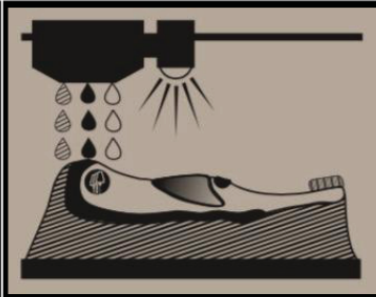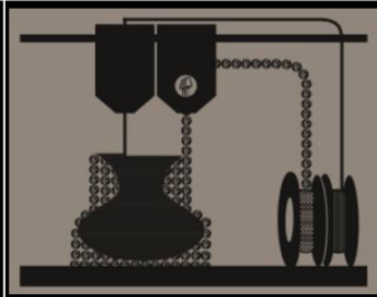
VAT Photopolymerization	**Material Jetting**	**Material Extrusion**
Also called: SLA™, CLIP™	**Also called:** Polyjet™, Projet™	**Also Called:** FFF, FDM™
Process: Select areas are exposed to a light source which initiates polymerization of the photopolymer resin	**Process:** Droplets of UV curable resin or molten polymer deposited in raster pattern	**Process:** Thermoplastic polymer extruded through an orifice and laid in raster pattern
Strengths: • High accuracy • High surface quality	**Strengths:** • High accuracy • Ability to use multiple colors or materials	**Strengths:** • Economical • Highly scalable • Ability to use reinforced materials
Typical Materials: UV-curable resins	**Typical Materials:** UV-curable resins and other polymers	**Typical Materials:** Thermoplastic polymers

Figure 1.1.: Comparison of polymer AM technologies [2].

VAT photopolymerization is a polymer AM process that cures layers of liquid photopolymer resin by exposing specific areas to UV light. Areas exposed to the light source are transformed to solid through a polymerization reaction. Once one layer is cured, additional resin is added to the surface of the part before the next layer is cured. VAT photopolymerization is capable of achieving higher accuracy and

surface quality than competing methods. Drawbacks include the long printing times required for the process and expense of UV-curable photopolymers. However, an emerging new technology known as continuous liquid interface production, or CLIP, has recently been commercialized and offers high resolution and surface finish at times 10 to 100 times faster than existing VAT photopolymerization processes.

Material jetting is a process that involves printing a part layer by layer by depositing droplets of polymer in a computer generated path. Droplets of photocurable resins can be jetted onto the part and cured by UV light. In addition, molten thermoplastic polymer droplets can be jetted onto the part and solidified at the ambient temperature. Material jetting is capable of achieving high accuracy and printing with multiple colors or materials. Drawbacks include the long printing times required for the process and expense of feedstock polymers.

Material Extrusion, commonly referred to as fused deposition modeling or FDM, is the most common polymer AM method due to its low cost and simplicity. The majority of desktop or hobbyist printers utilize this method. Similar to material jetting, FDM involves depositing thermoplastic polymer throughout a computer generated path, however in the form of an extruded bead rather than droplets. Typical FDM printers have layer resolutions in the range of 100-300 µm, resulting in a characteristic layered texture. As a result, FDM parts require post processing in order to achieve a surface comparable to the methods above. FDM can be used with a wide range of thermoplastic polymers and composites and is the most scalable of all AM technologies. In fact, machines that use this method have been used to print houses by extruding concrete.

1.1.3 Additive Manufacturing of Fiber-Reinforced Polymers

Advances in both materials and equipment are required in order to render polymer parts made using AM suitable for applications beyond prototyping or non demanding applications. The limited number of polymers that can be used with current machines lack the mechanical and thermal properties required for load-bearing or high

temperature applications [3]. Reinforcing polymers with fibers of higher strength and stiffness can significantly enhance the properties, and this practice has thus generated interest from the AM community [3, 4, 5, 6, 7, 8]. Fiber reinforcement can be in the form of continuous or discontinuous fibers, however continuous fiber reinforcement is most often reserved for low rate, high cost, and high performance applications. For higher rate applications that utilize melt processing methods (i.e. extrusion, injection molding, compression molding) discontinuous fiber reinforcement is commonplace.

When a fiber is introduced into a polymer matrix, loads are transferred from the weaker matrix to the stronger fiber. Figure 1.2 illustrates the load transfer mechanism, which takes place across the length of the fiber [9]. A critical length L_c exists and defines the length required to complete the load transfer between the fiber and matrix without either fracturing. In the case of perfect adhesion between the fiber and matrix materials, experimental results propose that aspect ratios exceeding 100 are required in order to achieve the maximum strength [10]. When a polymer composite contains fibers shorter than the critical length, the composite is said to be a short fiber-reinforced polymer, or SFRP. When fiber length exceeds the critical length, the composite is a long fiber-reinforced polymer, or LFRP.
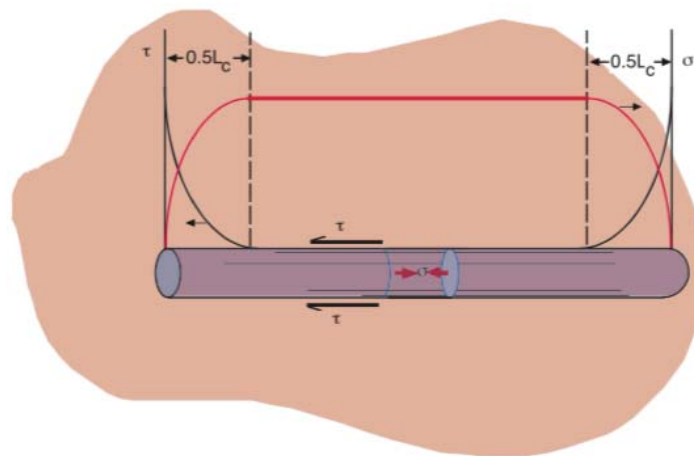
Figure 1.2.:   Illustration of the load transfer mechanism in a fiber-reinforced polymer[9].

To produce discontinuous fiber polymer composites, fibers of a certain length are compounded with polymer to make composite pellets, which serve as the feedstock material in downstream processes. During processing in melt flow applications, the polymer within each pellet melts and the fibers orient with the flow direction. The resulting properties of a part made using discontinuous fiber reinforced polymers are highly dependent on the resulting fiber orientation distribution, and always carry some degree of anisotropy since the orientation distribution is never random. The resulting fiber length distribution also greatly influences the final part properties. The length distribution is affected by fiber-fiber interactions, with greater breakage occurring as fiber loading increases [11]. Fiber breakage can also occur from interaction with equipment surfaces (screws, dies, barrels) and the polymer matrix, therefore the processing equipment and conditions also greatly influence the final fiber length distribution [3], [12].

Of the various polymer AM methods, FDM is most suitable for printing with reinforced polymers. Fibers can be compounded with polymer beforehand and fed into the extruder on a FDM machine. Carbon fibers act as a barrier to UV light, making methods that utilize photopolymerization for printing a challenge. Material jetting is not an ideal method because the viscosity of fiber reinforced polymers is too great.

1.2 State of the Art: Fused Deposition Modeling of Fiber-Reinforced Polymers

Limited literature has been published detailing studies of FDM processes utilizing fiber-reinforced thermoplastic composites. Even less exists detailing the phenomena specifically encountered in large-scale FDM. This section summarizes the major findings of research conducted on small-scale FDM, then introduces the pioneering work in large-scale FDM more related to our work.

1.2.1   Small-Scale Fused Deposition Modeling

Gray et al. [7] reinforced polypropylene (PP) with thermotropic liquid crystalline polymer (TLCP) fibers to produce filament for FDM. A novel dual extrusion process was utilized to plasticate the PP and TLCP separately since different processing conditions were required [7]. The molten TLCP was then injected into the molten PP matrix, and the composite was blended in a series of mixers before being extruded and drawn into filament [7]. Their method resulted in fibers with aspect ratios exceeding 100, which is difficult to achieve using glass or carbon fibers [7]. The modulus and strength of samples having 20-40 weight percent TLCP processed at different temperatures were measured. The tensile modulus and strength of the samples reinforced with 40 weight percent TLCP increased nearly 150% and 100% respectively [7]. A large degree of anisotropy also resulted in the samples due to the high degree of fiber orientation that results in the print direction. Figure 1.3 shows the dependence of tensile modulus and strength on the volume fraction of material laid in the print direction [7].
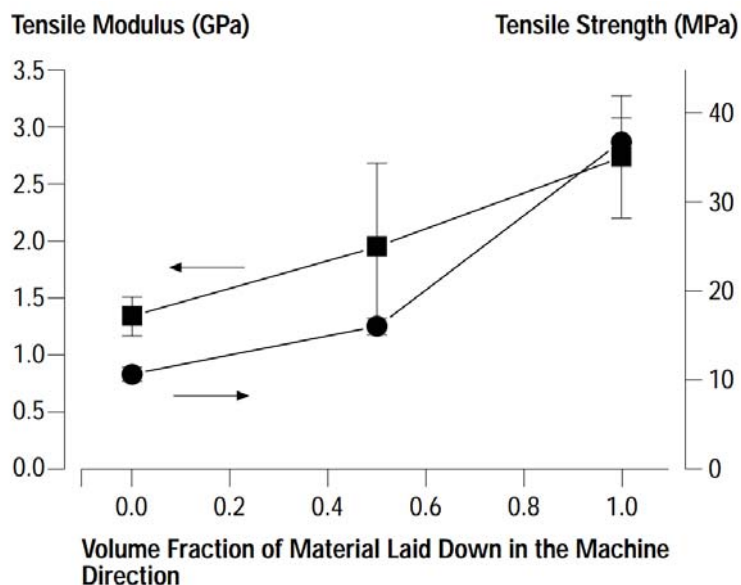
Figure 1.3.: Anisotropy of tensile modulus (■) and strength (●) in 40 weight percent TLCP fiber-reinforced polypropylene FDM samples [7].

Zhong et al. [6] used a two step process to produce glass fiber-reinforced acry-lonitrile butadiene styrene (ABS) feedstock filament having 10-18 weight percent glass fiber. The glass fiber was compounded with ABS in a twin screw extruder and gran-ulated into pellets. These pellets were then fed into a single screw extruder and extruded into a filament having a diameter ranging from 1.75-1.90 mm [6]. The original filaments lacked the required flexibility to be processed in an FDM machine, therefore plasticizers and compatibility agents were added and served to improve both the properties of the materials and the ability to process the filaments through the printer nozzle [6]. A MEM-250 multi-functional FDM machine was then used to print the square geometry shown in figure 1.4 using each of the filaments [6]. Longitudinal and transverse samples 90 mm long x 20 mm wide x approximately 2 mm thick were machined from the square and the tensile strength of each sample was measured. The longitudinal samples had a tensile strength approximately 50% higher than the strength of the neat ABS samples [6]. The transverse tensile strength of the reinforced samples was lower than that of the neat ABS samples [6]. Although not explicitly stated, this decrease in transverse strength could suggest that the diffusivity of the polymer chains was hindered by the presence of glass fibers, decreasing the chain diffusion and entanglement that occurred across the interface between printed layers. However, the transverse tensile strength increased with increasing fiber content in the reinforced samples, and approached that of the neat ABS samples at 18 weight percent fiber [6]. The authors speculate that this could arise from an increased prob-ability of fibers bridging adjacent layers during printing as fiber loading increased [6].
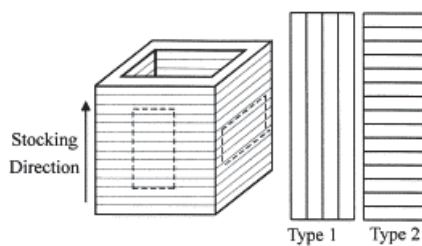
Figure 1.4.: Square geometry for tensile sample preparation [6].

Shofner et al. [5] combined 10 weight percent vapor grown carbon fibers (VGCF) with ABS to produce filaments for FDM and compared the properties of printed samples with those of samples printed from neat ABS. A multi-step process including mixing, compression molding, and extrusion was used to produce the reinforced filaments. Banbury mixing was used to disperse the VGCFs homogeneously throughout the ABS matrix [5]. The mixture was then compression molded into sheets, which were granulated and fed into a single screw extruder to produce FDM feedstock filament [5]. A Stratasys FDM 1600 Modeler was then used to print tensile testing specimens of various bead orientations [5]. The mechanical properties of the VGCF/ABS composite displayed an increase over the neat ABS. The samples having all beads oriented in the loading direction had an average tensile modulus of 0.79 GPa and strength of 37.4 MPa, an increase of 60% and 39% respectively over the neat ABS samples [5]. These samples also displayed a large decrease in ductility, with the elongation to failure decreasing 86% from that of the neat ABS to approximately 5% [5]. The authors attribute the decrease in ductility to poor fiber-matrix adhesion and interlayer bonding [5]. Tensile samples were also printed having alternating layers of beads oriented 10° and 90° from the loading direction. Figure 1.5 shows SEM images of the fracture surfaces of these samples. Clearly, less fusion occurred between the beads in the VGCF/ABS sample, attributed to less swelling of the extrudate and decreased chain mobility due to the presence of fibers [5]. The tensile strength of these samples was approximately 25 GPa, slightly greater than that of the neat ABS samples [5]. The strength contribution of the 10° layers more than compensated for the little to no fusion that occurred at the interfaces between adjacent beads in the 90° layers. When compared to the samples having all beads oriented in the loading direction, the tensile strength dropped approximately 33% [5]. This illustrates the large dependence of mechanical properties on the bead orientation within each layer.

Figure 1.5.: SEM images of fracture surfaces of 10°/90° FDM samples from neat ABS (top) and VGCF/ABS composite (bottom) [5].

Using a similar compounding and filament production process to Zhong et al. [6], Tekinalp et al. [3] produced ABS filament containing 10, 20, 30, and 40 weight percent short carbon fiber as well as neat ABS filament. The filaments were used to manufacture parts utilizing FDM and compression molding to allow for a comparison between the contrasting processes. The resulting fiber length, voids, and tensile

strength of parts made using each process were investigated. To prepare the FDM samples, dog-bone specimens were printed from the filaments using a desktop Solidoodle 3 FDM printer. Nozzle clogging occurred during printing with the 40 weight percent filament, therefore a complete sample could not be printed. To prepare the compression molded samples, the filaments were cut into small pellets and molded into bars, which dog-bone specimens were then machined from.

Fibers were extracted from the samples through matrix dissolution and imaged for length characterization. Figure 1.6 shows the fiber length distributions for the compression molded and FDM samples. In both the compression molding and FDM process, the average fiber length decreased as the fiber loading increased [3]. The average fiber length in the samples was 0.4 mm or lower, compared to 3.2 mm prior to compounding and producing the filaments [3]. The high-shear mixing that occurs during the compounding process results in significant fiber breakage. Fiber-fiber interaction also leads to fiber breakage, causing the average fiber length to decrease as fiber loading increases. During an FDM process, further fiber breakage is induced during flow through the die and turning 90° after exiting, explaining why the average fiber length was typically shorter in the FDM samples.
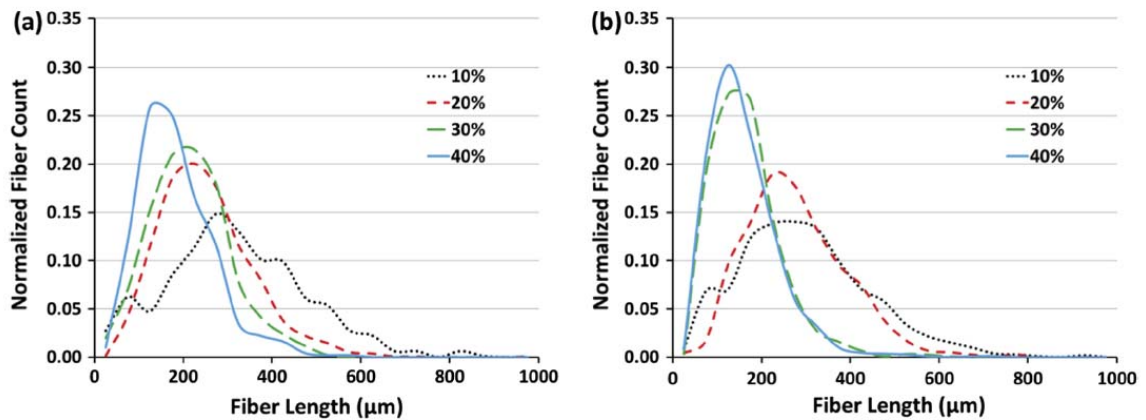
Figure 1.6.: Fiber length distributions for a) compression molded samples and b) FDM samples [3].

The Bay and Tucker stereological technique was used to characterize the resulting fiber orientations [13]. In this method, a fibers orientation angle with respect to the polished plane is defined by the shape of the elliptical cross section. In the FDM samples, a high degree of fiber orientation was observed in the print direction. This is expected and occurs as a result of shear forces in the polymer during the extrusion process. As the fiber content increased, a lower percentage of the fibers were oriented in the print direction, likely arising from the fiber-fiber interactions [3].

No visible voids existed in the compression molded samples, typical of a molding process involving high pressure. However, two types of voids were characterized in the FDM samples: inter-bead and inner-bead voids. Inter-bead void formation is inherent of FDM processes, and is a result of stacking circular or elliptical beads to build a part. Since the packing factor can never reach one for round bead cross sections, these voids are unavoidable. Inter-bead voids are actually channels that run parallel to the print direction, with their cross section depending on the difference between the step height and bead diameter in the process (extent to which a bead is pressed down during deposition). The size of the inter-bead voids was found to decrease as fiber loading increased, attributed to decreasing die swell and increasing thermal conductivity with increasing fiber content [3]. A decrease in die swell resulted in smaller bead cross sections which could be packed tighter, resulting in smaller inter-bead voids [3]. Higher thermal conductivity results in previous beads softening to a greater extent when hot beads make contact [3]. The softening increased the contact area, and although not mentioned by the authors also likely increased the interface growth driven by a reduction in surface energy. Although improved packing and smaller inter-bead voids were observed with increasing fiber content, an increase in inner-bead voids, or voids forming within each bead, was also observed [3]. Inner-bead voids formed along the edges and ends of fibers, attributed to poor fiber-matrix adhesion [3]. The competing effects of inter-bead and inner-bead voids resulted in the overall void fraction ranging between 16-27%, showing no trend linked to fiber content [3].

Tensile testing was conducted to measure the strength and modulus of the samples and compare the outcomes of the two manufacturing processes. The resulting tensile strength and modulus values are plotted in figure 1.7. The properties increased as fiber loading increased for both the FDM and compression molded samples. However, the gain in mechanical properties for the FDM samples seemed to diminish as loading increased, attributed to the decrease in fiber length and increase in inner-bead voids [3]. Although the compression molded samples contained no voids and typically greater fiber lengths, the strength was only slightly greater and the stiffness values were similar when compared to the FDM samples. The high degree of fiber orientation that results in the print direction during FDM compensated for the high void content and decreased fiber length [3]. However, anisotropy was not even mentioned in this study, even though it certainly existed and still remains one of the greatest disadvantages of FDM. In addition, the compression molded samples were likely also anisotropic since the fibers orient with the direction of flow during processing. A part having isotropic properties in-plane could possibly be produced using FDM if the print path followed the orientation of a quasi-isotropic laminate, however the out-of-plane properties would still lag and strongly depend on fusion across bead interfaces.
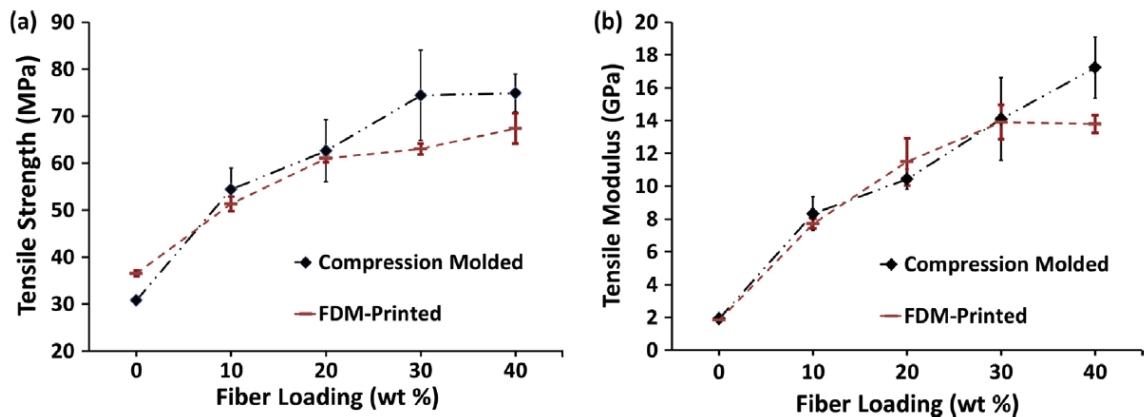
Figure 1.7.: Comparison of the tensile a) strength and b) modulus for compression molded and FDM samples [3].

1.2.2 Large-Scale Fused Deposition Modeling

The aforementioned studies all focused on small-scale AM (build volumes under a cubic foot), because this scale is easily attainable on most commercial FDM machines or DIY kits. In February of 2014, Oak Ridge National Lab (ORNL) embarked on a project with the objective to scale AM to build volumes and rates an order of magnitude greater than the existing technologies. The objective was to print fiber-reinforced polymers at deposition rates exceeding 50 cubic cm/min outside of a temperature controlled atmosphere. The work has resulted in a Cooperative Research and Development Agreement (CRADA) between ORNL and Cincinnati Inc., and a large-scale AM system, known as Big Area Additive Manufacturing or BAAM, has been commercialized. The first generation BAAM machine was capable of a deposition rate exceeding 250 cubic cm/min and build volume of over 7 cubic meters, increasing the print speed of FDM by a factor of 1000 and possible build volume by a factor of 15 over the largest commercial FDM system attainable at the time [8]. This machine generated a great deal of interest in large-scale AM both from industry and academia.

A BAAM system, shown in figure 1.8, consists of an extruder mounted on a 3 axis gantry system and a heated table capable of an additional 36 inches of vertical travel. During the printing process, polymer pellets are dried and conveyed to a single screw extruder having a screw custom designed for high extrusion rates. The reinforced polymer is extruded through a die having a diameter of approximately 5-10 mm and deposited along the print path, similar to small-scale FDM. The ability to process polymer pellets from various suppliers instead of pre-extruded and dried filament reduced the feedstock polymer cost from \$50-\$100/kg to under \$10/kg [8]. The cost of the feedstock polymer is highly dependent on the amount of carbon or glass fiber within the pellets, and exceeds \$10/kg when high fiber content exists.

Figure 1.8.: Big Area Additive Manufacturing or BAAM system developed by Oak Ridge National Lab (ORNL) and Cincinnati Incorporated (CI) [14].

As AM scales, the value proposition of fiber-reinforced materials becomes greater. In fact, printing at BAAM's scale is often not possible with non reinforced, or neat polymers. During an FDM process, hot layers are deposited onto previously deposited layers, which have already begun cooling and contracting due to thermal contraction and/or crystallization if printing with semicrystalline polymers. This nonuniform shrinkage caused by the temperature gradients in FDM leads to residual stresses and warpage in printed parts. Figure 1.9 shows bars printed by ORNL from both neat ABS and 20 weight percent short carbon fiber-reinforced ABS. Clearly, the bar printed from reinforced ABS shows no observable warpage, while the neat ABS bar warped to a great extent. The addition of carbon fiber lowers the coefficient of thermal expansion (CTE), which minimizes the thermal contraction that occurs after deposition. The fiber-reinforcement also significantly increases the stiffness, which suppresses the warpage and therefore induces residual stresses in printed parts. Cer-

tain commercial FDM machines have heated build envelopes that serve to minimize and relax the stresses developed during printing. However, at BAAMs scale, a heated envelope would require a great deal of energy and significantly increase the cost. Therefore, the motivation exists to develop materials, processes, and equipment that allow large-scale AM outside of a heated envelope.

Figure 1.9.: Decreased warpage in carbon fiber-reinforced printed bar [15].

However, when printing very large parts, the addition of 20 weight percent carbon fiber is sometimes not enough to inhibit warpage. Figure 1.10 shows one of the first attempts at a 3D printed car. As the upper layers contracted on top of previously contracted layers, significant warpage and delamination resulted [15]. This photo illustrates the need for improvements in printing materials, speeds, and simulation tools to optimize the design of printed parts and processing parameters.

Figure 1.10.: Layer delamination that occurred in an early attempt to 3D print a car [15].

ORNL investigated the mechanical properties of neat and 20 weight percent carbon fiber-reinforced ABS. Plates 20 x 20 x 1 inch were printed in three orientations: 0°, 90°, and +45°/-45°. The plates were machined flat and dog bones were cut out using a water jet. The dog bones were dried at 50°C for 48 hours, placed in a desiccant chamber at 23°C for 15 hours, and tensile tested per ASTM D638. Table 1.1 shows a summary of the results. The stiffness and strength are anisotropic, varying by as much as a factor of 4 in different directions. The presence of carbon fiber significantly increased the strength and stiffness in the 0° samples due to the high degree of fiber orientation in the load direction. The strength in the 90° and +45°/-45° reinforced samples decreased. The stiffness in the 90° sample remained unchanged, and increased approximately 50% in the +45°/-45° samples. This degree of anisotropy illustrates the challenges in designing and predicting the final properties of large scale AM

components. A need for extrusion dies that produce a more random fiber orientation distribution exists.

Table 1.1: Mechanical properties of printed neat and carbon fiber-reinforced ABS.

	Modulus (GPa)			Strength (MPa)		
	0°	**90°**	**45°/-45°**	**0°**	**90°**	**45°/-45°**
Neat ABS	2.25	2.20	2.20	34.0	27.0	33.5
20 wt% CF	8.20	2.25	3.20	53.0	12.0	20.0

1.3   Project Outcomes

The objective of the Purdue University AM research group advised by Dr. R. Byron Pipes was to develop a lab-scale AM system capable of printing discontinuous fiber-reinforced polymers and to investigate the FDM process and its outcomes. At the start of the project, only amorphous SFRPs with processing temperatures up to 250°C had been printed. The system developed at Purdue was to be capable of processing high temperature LFRPs, including polyphenylene sulfide (PPS), polyetherimide (PEI), and polyetheretherketone (PEEK). Table 1.2 compares the properties of these LRFPs with the most commonly printed SFRP. The properties were obtained from the respective datasheets for the materials. Glass transition temperature (T_g) values are not given in the table, as the reported values in the datasheets are sometimes of the neat polymers and do not reflect the apparent T_g of the composites. The increased elastic modulus (E), tensile strength (UTS), temperature stability, and lower CTE make LFRPs attractive for future AM applications.

After the AM system was completed, a multi-year project investigating the FDM process with fiber-reinforced polymers began. The ultimate goal is to develop simulation models capable of predicting the outcome of and improving the process. The following areas will be studied in literature and through experimentation:

1. Optimal processing parameters/conditions for extrudate quality, print path, and overall part quality

2. Resulting fiber length and orientation

3. Mechanical properties of printed structures

4. Thermal analysis and residual stress formation in laid-down material and effect on warping or deviation from intended shape

5. Viscoelastic properties and stress relaxation in printed parts

6. Interface formation between adjacent layers during a printing process and effect on inter-layer strength

7. Crystallization kinetics and effects on resulting properties

8. Void formation

Learnings and experimental results will be used to develop simulation tools to model and predict the following phenomena:

1. Melting process and flow through extruder

2. Flow through the die and resulting fiber orientation

3. Solidification process and evolution of crystallinity

4. Temperature gradients during printing and evolution of residual stresses

5. Modulus dependence on temperature

6. Stress relaxation in printed parts

Table 1.2: Property comparison for current and potential future carbon fiber-reinforced polymers for FDM AM processes.

Trade Name / Supplier	Polymer / Fiber wt%	E (GPa)	UTS (MPa)	Processing Temp (°C)	CTE	Cost ($/lb)
Electrafil / Techmer	ABS / 15	11	100	230	1.8E-5	4
THERMOCOMP EC008APQ / SABIC	PEI / 40	39.4	268	380	3.0E-6	30
THERMOCOMP LC008E / SABIC	PEEK / 40	33.1	241	380	2.7E-5	70
CELSTRAN PPS-CF 50-02 / Celanese	PPS / 50	41.7	155	330	2.3E-5	18

CHAPTER 2. LAB-SCALE ADDITIVE MANUFACTURING SYSTEM DESIGN AND DEVELOPMENT

2.1   Introduction

Oak Ridge National Lab (ORNL) and Cincinnati Incorporated (CI) pioneered the field of large-scale AM of polymer composites and uncovered early applications of the technology, most notably the manufacturing of composite tooling outlined in chapter 4. ORNL and CI also uncovered the need to better understand the various phenomena involved in AM and to develop materials, processing equipment, and simulation models capable of improving the process. As explained and illustrated in section 1.2.2, the residual stresses caused by non-uniform thermal contraction can lead to detrimental warpage and/or delamination during a printing process. Therefore, a greater understanding of the relevant phenomena and ability to predict process outcomes is essential to further facilitate the transition of the technology to the marketplace. This is the motivation behind the efforts of our group.

In the fall of 2014, the effort began to develop a lab-scale AM system capable of processing high temperature and high fiber content thermoplastic polymers. The system was to be unique in that it would not serve as a production machine, but instead a research instrument that would offer full flexibility regarding component selection, processing conditions, material selections, controller options, operating software, sensor implementations, build volume, speed, and more. A system capable of meeting these requirements is obviously unattainable in the market, and had the be developed in its entirety. In one year, a diverse and cross functional team successfully designed and developed the system. The team consisted of Eduardo Barocio, Anthony Favaloro, Bastian Brenken, and myself Nicholas DeNardo, and was advised by Dr. R. Byron Pipes. The system has been the first capable of printing carbon

fiber-reinforced polymers having fiber loading up to 50 weight percent, the strongest polymer composites printed to date. The ability to plan and execute a full design and development cycle for an advanced piece of equipment was an invaluable experience and one that few are fortunate enough to experience during a graduate program.

2.2   Configuration and Component Selection

2.2.1   Ideation

The process began with an ideation phase, where the group spent approximately one month studying AM and determining what type of system would be appropriate for the project. For the reasons discussed in section 1.1.3, a system incorporating FDM was determined to be ideal.

Traditional FDM systems consist of a stationary table and moving extruder, or table that moves in the x-y plane and extruder that moves in the z direction. The large-scale system developed by ORNL and CI consists of a 3 axis gantry mounted extruder and motion table capable of lowering to increase the possible build height. This set-up is ideal in terms of achieving the largest build volume for a given machine footprint. In addition, keeping the part stationary in the x-y plane during printing allows for higher speed printing. If the table instead moved in the x-y plane, the inertial forces associated with rapidly moving a hot and heavy part could lead to deformation and/or the part separating from the table. The disadvantages of the ORNL and CI configuration include the high cost of a gantry system and the limitation of extruder selection to a relatively compact and lightweight design.

After evaluating the possible configurations, one incorporating a stationary extruder and 3 axis servo controlled table was decided upon. This set-up provides the greatest flexibility in extruder selection, and allows easier monitoring of the extrusion process. Since the machine is meant to serve as a research instrument, high speed printing and a large build volume are not critical and can be sacrificed.

The major components in the system are the extruder, the motion controlled table, and the controller. The features for each major component were prioritized to aid in selecting from the many options.

2.2.2   Feature Prioritization

2.2.2.1. Extruder

The extruder is the most important component as it determines what materials can and cannot be printed by the system. Most extruders on the market are very large, weighing over 500 lbs and impractical for use in an AM system. In addition, most are not ideal for processing fiber-reinforced polymers. Fibers are abrasive and can lead to premature wear of equipment surfaces. During processing, fiber interaction with equipment surfaces and other fibers results in fiber breakage, decreasing the overall fiber length and thus mechanical properties.

The feature prioritization for the extruder is shown in table 2.1. First, the extruder had to be capable of processing highly viscous long fiber-reinforced polymers with melt temperatures up to 400°C. Second, the extruder had to preferably have a screw designed in such a way to limit fiber breakage and maximize the resulting length. Third, the extruder had to be relatively compact and able to be mounted on a steel frame above a moving table. Fourth, the controls of the extruder had to be compatible with a LabVIEW interface. Lastly, the extruder had to have interchangeable dies to allow for die customization. Cost was not of primary concern in extruder selection due to the importance of the extruder to the overall system and research objectives.

Ultimately, A Randcastle RCPH-1000 Microtruder was decided on. Although not ideal, the Microtruder met the requirements better than any alternative. The extruder has a 1 inch 24:1 length to diameter ratio screw and is made from heat-treated abrasion resistant D2 steel. The extruder also features a cooled feed section,

vacuum venting, and patented surge protection to achieve a more constant flow. The output ranges between 5-15 lbs/hr, depending on the polymer being processed.

The major disadvantage of the Microtruder is the two mixing sections in the screw design, which are not necessary for pre-compounded materials and lead to extensive fiber breakage. In addition, the AC drive motor powering the Microtruder does not allow for quick stop and start actions during printing. However, although important in a production machine, quick stop and start capability is not essential in a research instrument. Lastly, feed issues result when using pultruded reinforced thermoplastic pellets as feedstock, therefore an auger pellet feeder must be used to starve feed the extruder.

Table 2.1: Feature prioritization for extruder and comparison with Microtruder RCPH-1000.

Feature (Priority)	Ideal	Microtruder RCPH-1000
Process high temperature and high viscosity polymers (1)	Up to 400°C and 50 wt % carbon fiber	✓
Screw designed to maximize fiber length (2)	No mixing sections	X
Compact design (3)	Under 350 lbs	✓
Controller compatibility (4)	LabVIEW	✓
Interchangable dies (5)	Threaded die receiver	✓

2.2.2.2. Motion Controlled Table

As stated, printing would be made possible through the use of a moving table rather than a moving extruder. The extruder would be mounted above the table, which would have unrestricted motion in x, y, and z. Most turnkey motion tables have very limited motion and are very expensive. In addition, many have a closed-frame construction, which would make it difficult to add on sensors, cameras, or heating accessories.

The feature prioritization for the table is shown in table 2.2. First, the table had to have the capability to move in the x, y, and z directions and achieve a build

volume of approximately 700 mm x 700 mm x 500 mm. Second, the table had to have high resolution and repeatability, and ideally be controlled by servo motors. Third, an open-frame construction was desired since this construction provides greater flexibility for adding peripheral devices and heaters in the table surface. Lastly, the table had to be capable of achieving a minimum in-plane speed of at least 80 mm/sec.

Due to the highly specific configuration and capabilities that were required, a custom table was designed and built. All of the components needed to construct the table were obtained from Velmex Inc. The table has a span of 648 mm x 648 mm in the x-y plane and is capable of elevating 465 mm. The table has a completely open-frame construction, with ample space for accessories and the ability to add a heated plate to the table surface. Preassembled screw driven linear guides incorporating high precision lead screws with +/- 4 µm repeatability were used to construct each axis. Each guide can support dynamic normal loads up to 1.3 KN, and exert maximum thrust forces of 450 N. The spatial resolution and velocity is given by the servo motor-screw pitch combination. The screw pitch selected is 0.2 in/rev for the x and y axis, and 0.1 in/rev for the z axis. An aluminum stand for the table was also purchased from Velmex.

DC servomotors were installed in the Nema-34 housings on the linear guides. The maximum achievable velocities with the selected screw-motor combination are 250 mm/s in the x-y plane, and 50 mm/s in the z axis. The maximum thrust force achievable is 900 N for the x and y axes and 1.8 KN for the z axis. The maximum spatial resolution is 6.35 µm for the x and y axes, and 3.175 µm for the z axis, but these can be reduced to 0.8 µm and 0.4 µm by changing the encoder configuration in the same motor.

Table 2.2: Feature prioritization for motion controlled table and comparison with Velmex table.

Feature (Priority)	Ideal	Velmex Table
3 axis motion with large build volume (1)	700x700x500 mm approx. build volume	✓
High resolution/repeatability (2)	Servo control with <10 µm resolution & repeatability	✓
Open-frame construction (3)	No enclosures and maximum open space	✓
Medium-high speeds (4)	>80 mm/sec	✓

2.2.2.3. Controller

The feature prioritization for the controller is shown in table 2.3. Many CNC controller options would be suitable for this system. First, the controller had to be compatible with G-code, Second, the controller had to be controllable from a computer interface. Lastly, the controller had to be able to receive signals from peripheral devices, including limit switches and emergency stop buttons.

A Dynomotion computer-based controller (Model: KFLOP) was selected. The controller board translates the G-code commands into a step-direction protocol that is sent to the servomotors in an open-loop fashion. The controller board receives the G-code from a computer USB port and executes the G-code in real time. A LabVIEW interface was built to operate the controller. Additionally, external signals, such as from limit switches and emergency stop buttons, can be acquired by the controller board and fed back to the computer.

Table 2.3: Feature prioritization for controller and comparison with Dynomotion solution.

Feature (Priority)	Ideal	Dynomotion
G-code compatible (1)	Translate to step-direction protocol	✓
Controlled from interface (2)	LabVIEW	✓
Receive signals from peripherals (3)	Acquires and feeds signals to computer	✓

2.3   System Design and Assembly

After selecting and ordering the equipment, the detailed configuration of the final system was designed. Figures 2.1, 2.2, and 2.3 show renderings and dimensions of the system including all of the major components. A table-style frame was designed to hold the extruder and starve feeder. The frame incorporates 3.5 inch steel profiles in order to minimize deflections and vibrations during usage. The legs of the frame are telescopic to provide a low print height setting, which allows easier observation of the extrusion and printing processes. The motion table sits under the frame and has completely unrestricted motion. A large fume hood was also fabricated to be mounted over the system and remove the fumes given off during printing.

When the major components arrived, assembly of the system began. The fume hood was first mounted above the system's location. Next, the table was assembled and wired beneath the hood. A heated bed was constructed on the table surface, and is capable of reaching 350°C. After being fabricated and powder coated, the steel frame was positioned over the table. Lastly, the extruder and feeder were mounted to the frame. The final assembly of the system involved hundreds of feet of wiring and thousands of minor components, resulting in months of build time and extensive learning. Upon completion, months were spent developing the controls and learning the optimal parameters for running the extruder and printing parts.
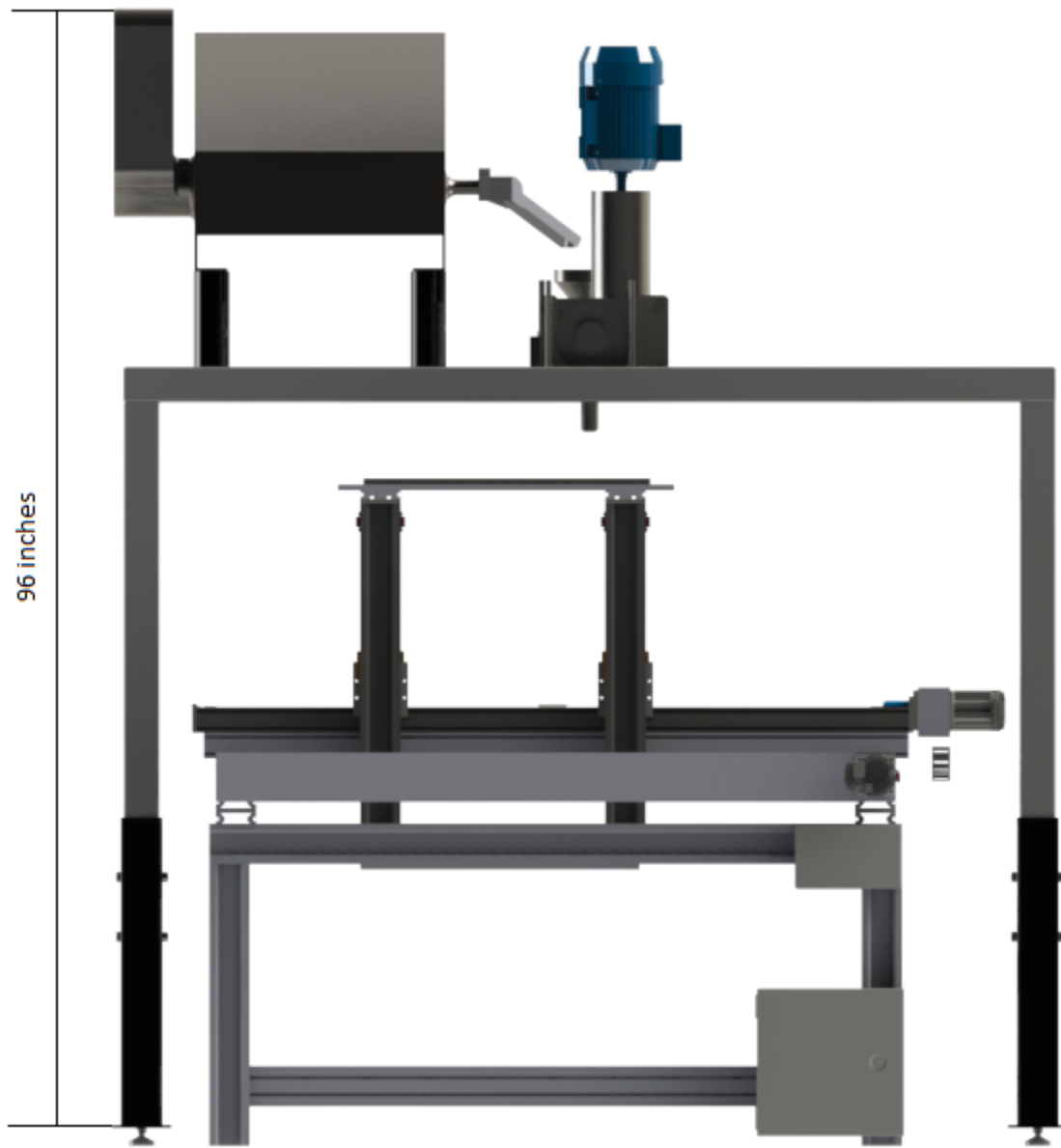
Figure 2.1.:   Side view of lab-scale FDM system.
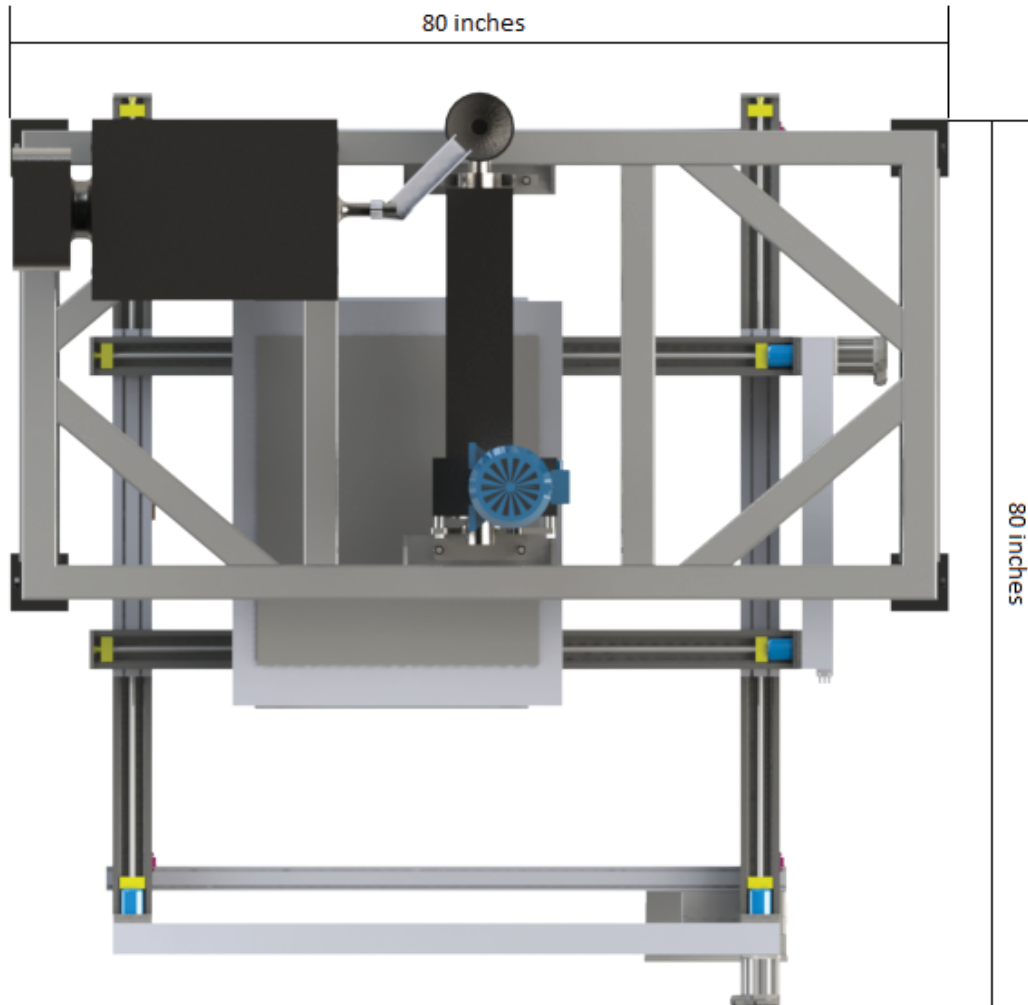
Figure 2.2.: Top view of lab-scale FDM system.
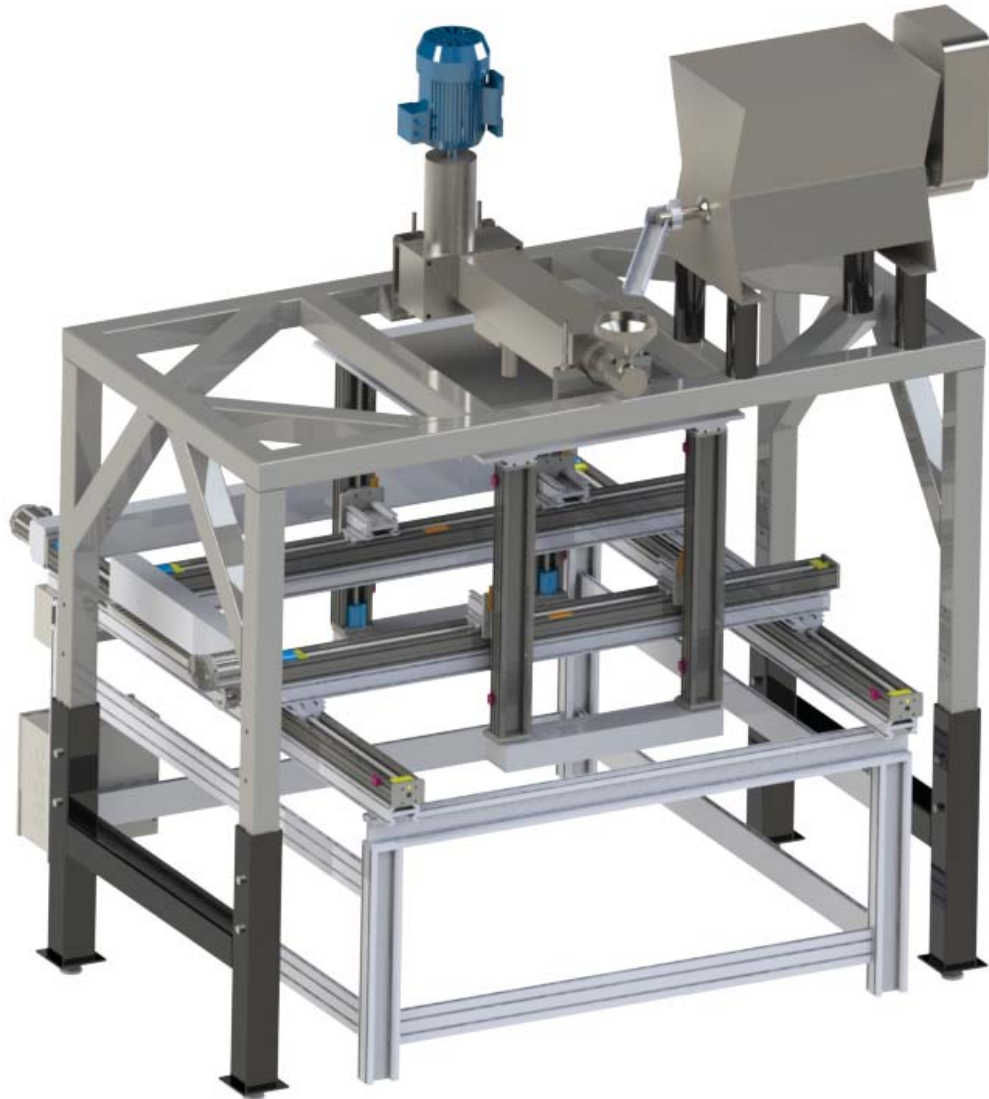
Figure 2.3.: Iso view of lab-scale FDM system.

CHAPTER 3. PRINTING PROCEDURE AND RESULTING MICROSTRUCTURE

As with other processes that convert a raw material to a final part, the processing conditions used during large-scale AM have a large effect on the resulting structure and properties of printed components. This chapter outlines the printing process for our system, provides insight into the microstructure of printed parts, and characterizes resulting properties.

3.1 Feedstock Material

The feedstock material most commonly processed in our FDM system is carbon fiber-reinforced PPS pellets produced using pultrusion. Pultrusion, shown in figure 3.1, is a well established process utilized to produce polymer pellets having highly oriented long fibers. In a pultrusion process, tows of fibers are drawn from a roll, bundled together, and pulled through a system of rollers, some of which are submerged in a resin [16]. The rollers impregnate the fibers and attempt to disperse the resin evenly throughout. The bundle is then pulled through a shaping die, cured (thermosets) or solidified (thermoplastics), and chopped to the desired length. Our pellets, shown in figure 3.2, contain 50 weight percent carbon fiber and are approximately 12 mm in length. Therefore, the initial length of the fibers before processing in the extruder is approximately 12 mm. Advantages of using pultruded pellets in our process included long initial fiber length and good resin impregnation. Disadvantages include the high cost and pellet geometry that is difficult for extruder screws to consistently convey from the hopper into the barrel.
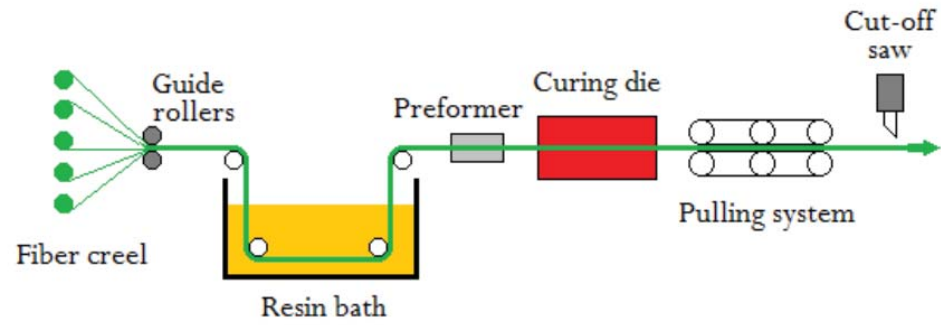
Figure 3.1.: Schematic of a pultrusion process [16].

Figure 3.2.: Long discontinuous carbon fiber-reinforced PPS pellets produced using pultrusion.

<div align="center">3.2   Printing Process</div>

AM processes are unique in that they are capable of converting a digital file of a desired part directly into a net-shape or near net-shape part. In AM processes that utilize FDM, the first step involves generating the path that the extruder will follow to build the part. To accomplish this, a solid file is processed in a slicing program, which divides the solid part into layers and generates a print path, as shown in figure 3.3. The user chooses the desired slicing parameters, including the number of perimeters, infill patterns, infill percentage, support structure, layer height, and step-over length. The slicing program outputs the G-code that controls the table during the printing process.
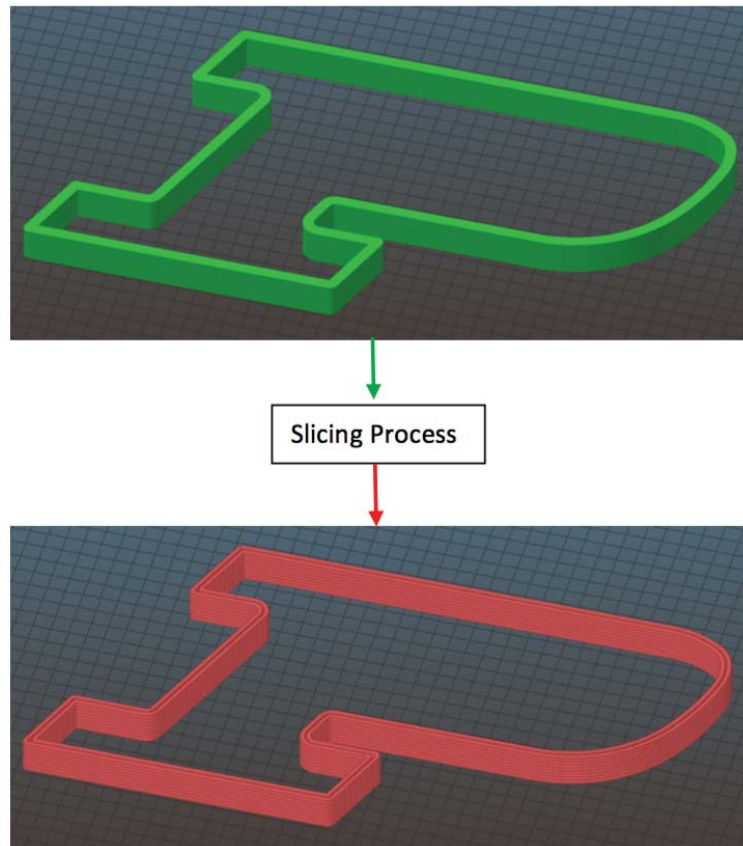
Figure 3.3.: A slicing program divides a solid CAD model into layers and generates a print path.

The die on our extruder is 3.17 mm in diameter and minimal die swell is observed when processing the fiber-reinforced PPS. Decreased die swell in fiber-reinforced thermoplastics has also been reported by [17, 18, 19]. During printing, a step-over length of 2.8 mm was found to be ideal and allows some overlapping of beads during printing. The optimal layer height for our system was found to be 2.2 mm. By using a layer height less than the extrudate diameter, newly extruded beads are pressed onto previous beads during printing, resulting in more contact area between beads and smaller inter-bead voids.

Determining the ideal infill structure in large-scale AM is quite challenging and involves extensive trial and error. During a small-scale FDM printing process, it is common for the extruder to stop and start many times during the print, typically when moving from one area to another. This is possible because small-scale FDM machines can stop and start extruding filament nearly instantaneously. However for the extruders used in large-scale FDM machines, interrupting the flow and cutting off the highly viscous filament to move to another location is challenging. Stopping the extruder requires a couple seconds, and bead quality is not immediately consistent upon restarting. Therefore, it is highly desirable to tune infill structures and parameters in a way that results in a continuous printing path with no stop and starts involved. However, it is rare to achieve zero stop and starts, and when it is required for the extruder to jump from one area to another, our system is programmed to make the table movement very rapidly. This draws the bead into a thin filament which can be easily removed during post-processing.

Prior to printing, the polymer pellets are dried and the extruder barrel and die temperatures are raised to approximately 325℃. When ready to print, the extruder is run for approximately 1-2 minutes to achieve consistent flow and bead quality. An auger feeder conveys the pellets to the extruder hopper (starve feeding) at the rate the extruder screw conveys pellets into the barrel. A screw speed of 95 RPM results in a high quality, consistent bead, and gives an output of approximately 5 lb/hr. The table is run at approximately 5500 mm/min, slightly drawing the beads during

printing. The heated table surface is typically raised to over 200°C to serve multiple purposes, including lessening the temperature gradients that could lead to warpage, helping parts adhere better to the table surface, and furthering the development of crystallization and stress relaxation in printed parts by keeping them at an elevated temperature. Figure 3.4 shows the part above being printed.
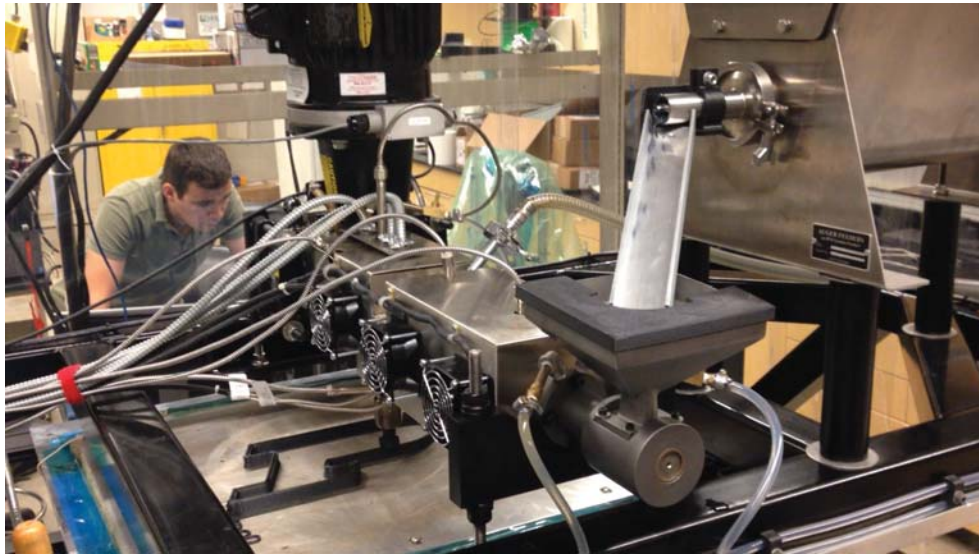
(a)
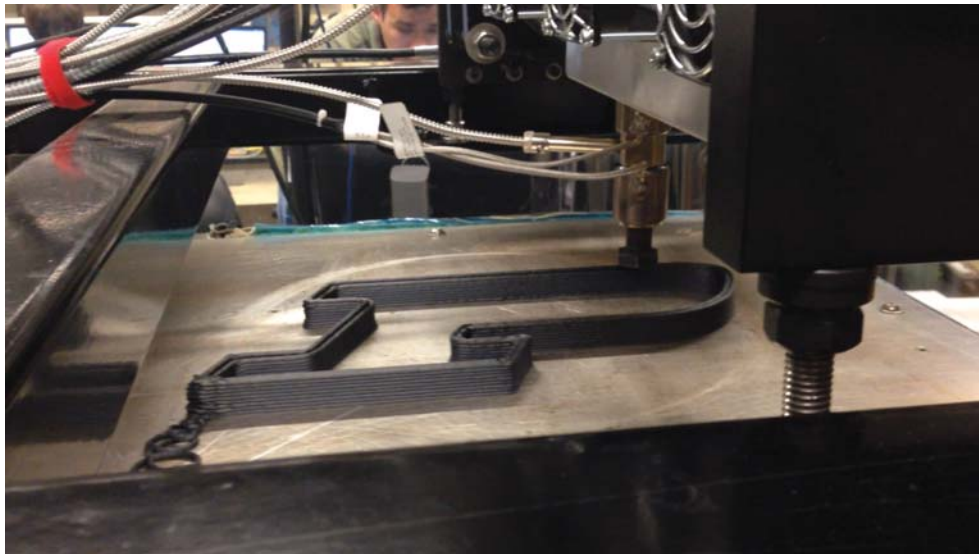
(b)

Figure 3.4.: View of FDM system during printing (a) and closeup of printed part (b).

As discussed in section 1.2.2, large temperature gradients and non-uniform shrinkage result during printing, leading to residual stresses and potential warpage. Figure 3.5 shows an in-situ thermographic from a FLIR model A655sc thermal camera of the part above being printed. The aluminum surface on the heated table resulted in a reflection appearing in the image. The superimposed black lines illustrate where the bottom of the part begins. The top layers had the highest temperatures since they were most recently deposited. The lower layers had more time to cool and were therefore lower in temperature. The temperature difference from the top of the part to the 3rd layer was approximately 130°C. The bottom two layers were actually higher in temperature than the 3rd layer due to the heated bed. This image illustrates that rapid cooling from the melt occurs, and that large temperature gradients can exist, even in a part having a layer time of 24 seconds. Faster layer times lead to less extreme temperature gradients and more uniform cooling and contraction during printing. As a result, commercial large-scale AM equipment manufacturers are targeting very high extrusion throughput (100 lb/hr) and high speeds.
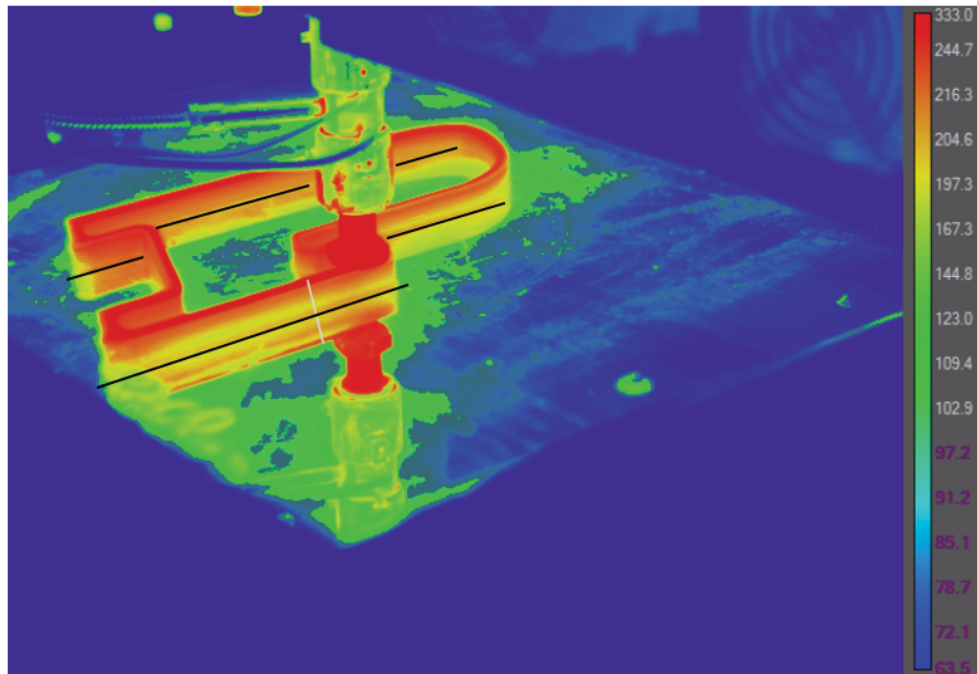
Figure 3.5.: In-situ thermographic of a printed part.

3.3 Structure

3.3.1 Crystallinity

The properties of printed structures are highly dependent on the crystallinity developed within the part during the printing process, therefore an understanding of the thermal history introduced during printing is required. PPS crystallizes fairly rapidly when cooled from the melt, and also undergoes cold crystallization between the crystallization and glass transition temperatures [20, 21, 22]. Results show that cold crystallization at 130°C occurs in a matter of minutes, however samples quenched and crystallized through cold crystallization do not reach the same levels of crystallinity as those crystallized from the melt. Kenny et al. [22] compared both melt and cold crystallization of neat and continuous carbon fiber-reinforced PPS. The presence of continuous fibers slightly slowed down both crystallization from the melt and cold crystallization. Further, the authors concluded that the mass fraction of crystallinity developed in the composite was approximately 10% less than that developed in the neat PPS. The authors attribute these findings to the impingement effects introduced on the crystals by the fibers. The authors also reported that the nucleation process occurs slightly faster in the composite PPS, where the fiber surfaces serve as nucleation sites.

During the printing process, heat from the table surface and new layers conducts into the part. Heat escapes the part at the surface through convection, however the relatively low thermal conductivity of the polymer limits the rate at which heat transfers to the surface. Due to the rapid crystallization kinetics of PPS, it was predicted that printed parts would develop max crystallinity, or a mass fraction near the max. Differential scanning calorimetry (DSC) was used to measure the degree of crystallinity within printed parts. DSC samples were cut from outer beads at the mid height of a part which took approximately 30 minutes to print. Figure 3.6 shows a representative DSC thermograph for the samples. Clearly, no exothermal peak resulted during the temperature ramp, indicating that no cold crystallization

occurred. This result proves that the max crystallinity attainable in the polymer can indeed be developed during the printing process. However, to be certain that the max crystallinity exists within regions of the part that may have cooled very rapidly, a short annealing cycle is recommended.

The crystallinity mass fraction X_{mc} is given by the ratio of the heat absorbed during melting H_m to the heat of fusion H_f of pure crystalline PPS, assumed to be 77.5 J/g [22]. H_m can be found by taking the integral of the endothermal peak, giving 16.09J/g. Since the PPS contains 50 weight percent carbon fiber, double the H_m should be used in the calculation for X_{mc}. Taking the ratio gives a X_{mc} of 0.42 (42%), a value in strong agreement with those reported in literature [22]. It is important to note that this value represents the mass fraction of the polymer that consists of crystalline regions. In the composite as a whole, the mass breakdown is as follows: 21% crystalline polymer, 29% amorphous polymer, and 50% carbon fiber.
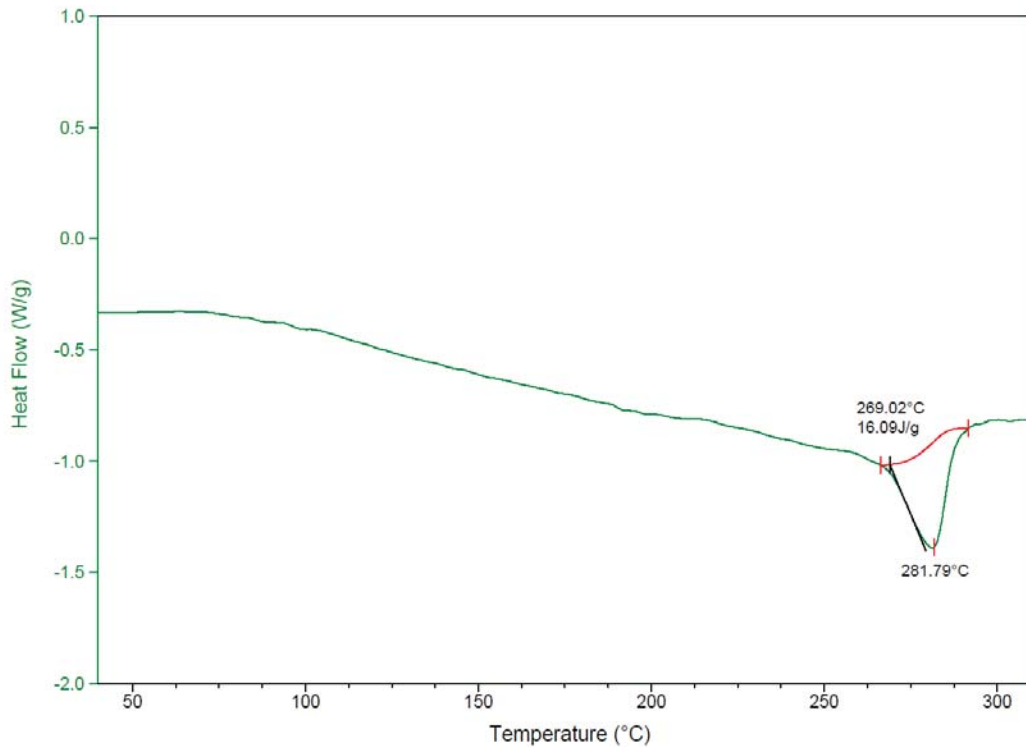
Figure 3.6.: DSC thermograph of a sample from a printed part.

3.3.2 Optical Microscopy

Microscopy was used to observe the fiber length and orientation, as well as to quantify the void content. Longitudinal and transverse cross sections were taken from an extruded bead, as shown in figure 3.7, and polished prior to imaging. Figure 3.8 shows a micrograph of the center of a longitudinal cross section taken at 20X. The image shows the high degree of fiber orientation that results in the print direction, evident by the vast majority of fiber cross sections appearing as circles or slightly angled ellipses. Very few fibers orient toward the transverse direction. Figure 3.9 shows a micrograph of the center of a transverse cross section taken at 10X. Again, the high degree of fiber orientation in the print direction is evident. This image shows the severe fiber length degradation that occurs in the extruder, an unfortunate result. Fibers enter the extruder having a length of 12 mm, and have resulting fiber lengths under 300 µm. The average resulting fiber length has not been measured, but appears to be between 100-200 µm.
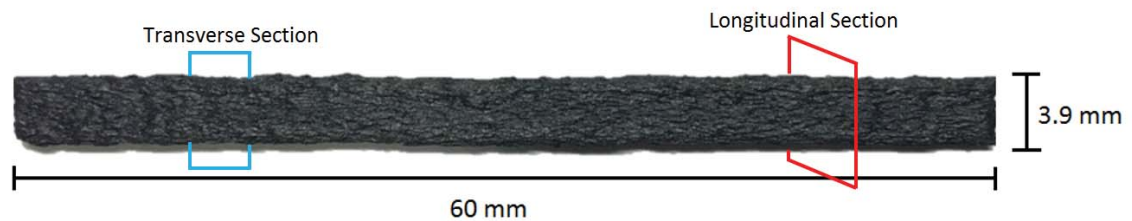
Figure 3.7.: Longitudinal and transverse cross sections observed under optical microscopy.
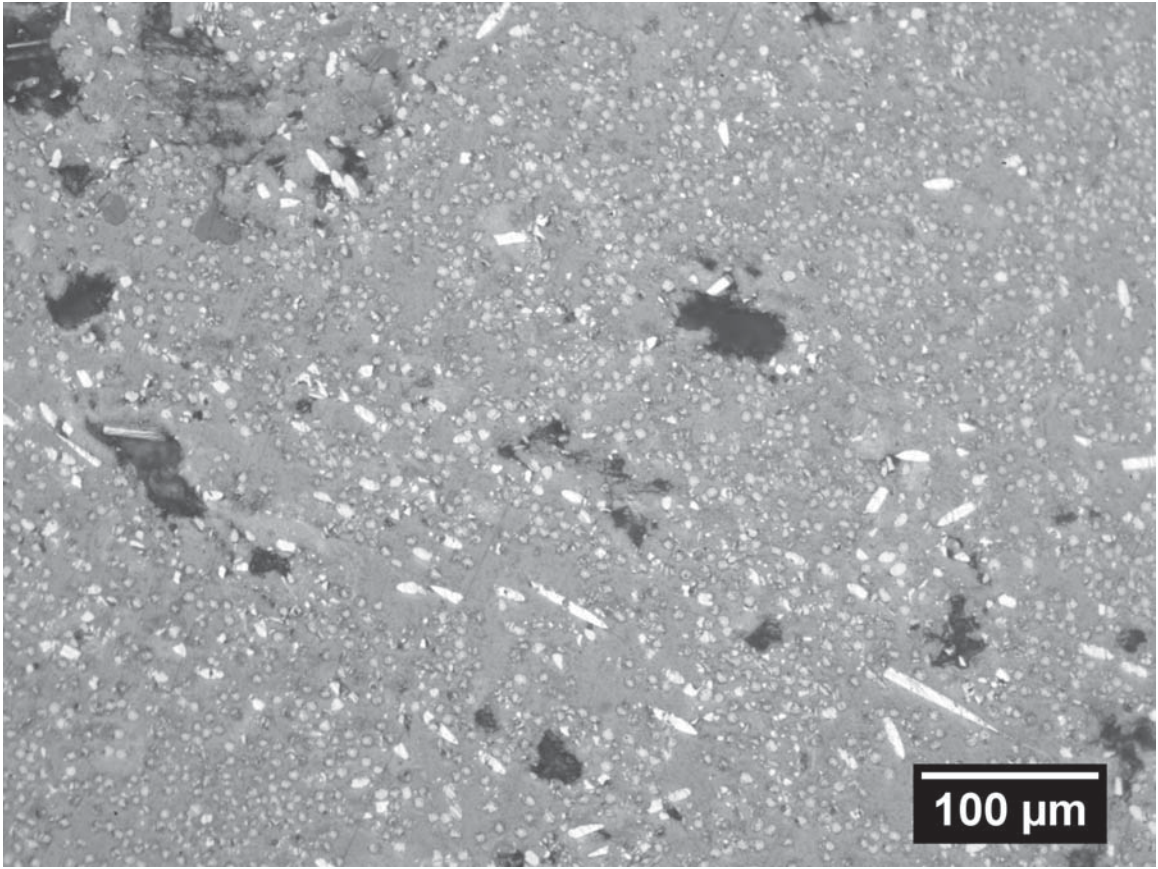
Figure 3.8.: 20X optical micrograph of a longitudinal cross section.
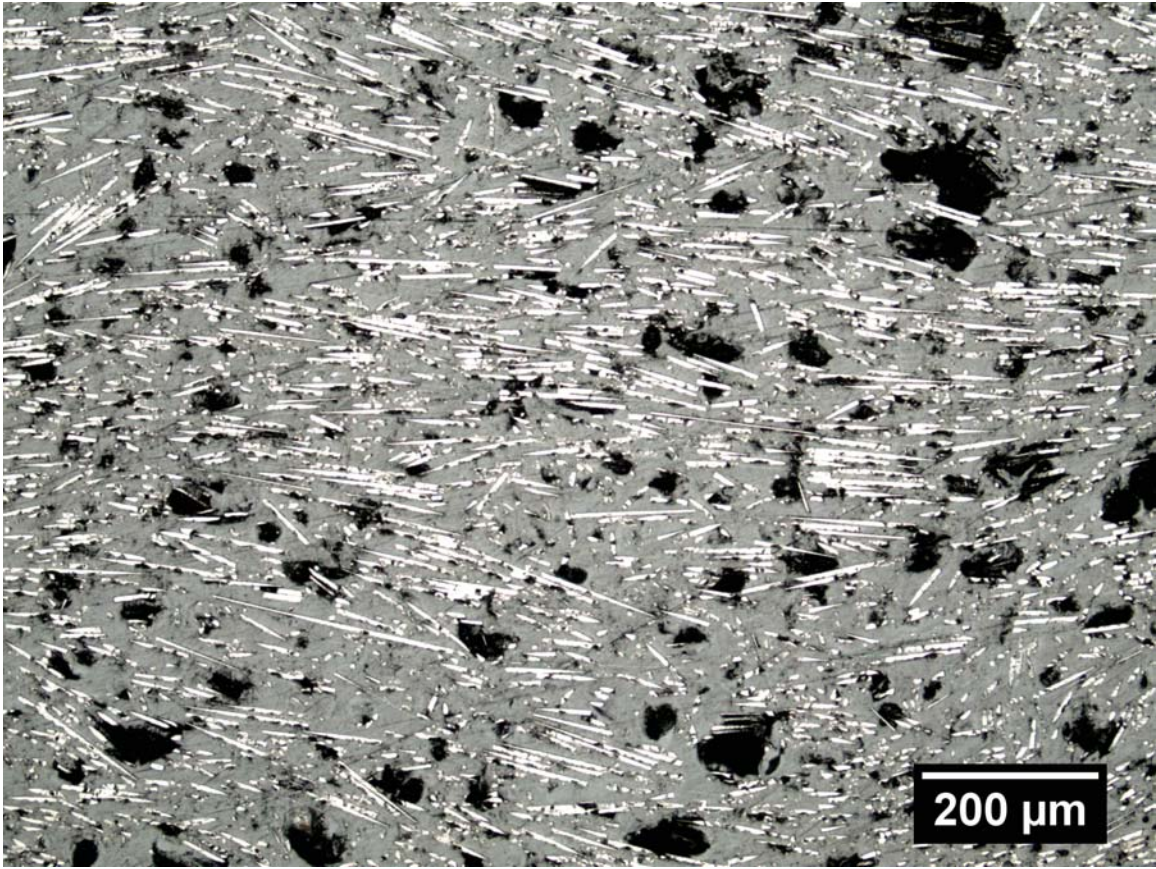
Figure 3.9.: 10X optical micrograph of a transverse cross section.

Another obvious result in the micrographs is the high inner-bead void content. The voids are expected to arise partially due to the entrapped air in the feedstock pultruded pellets, and partially due to a non-optimal extrusion process. As stated, the extruder is starve fed, and pellets are delivered to the hopper in small batches every few seconds. This inconsistent feeding could result in entrapped air that can not escape the highly viscous polymer during the extrusion process. The vacuum vent was not operated when extruding these samples due to inconsistent clogging issues which could introduce sample variability. However, significant void content still results when venting. The optimal extrusion control settings and screw design for minimizing voids are under investigation.

ImageJ was used to threshold voids in micrographs and measure their area fraction. Figure 3.10 shows a micrograph of a longitudinal cross section taken at

10X and the thresholded voids amounting to 0.074 area fraction. Figure 3.11 shows a transverse cross section at 5X, with thresholded voids amounting to 0.171 area fraction. The higher void fraction in the transverse section illustrates that voids elongate in the print direction, meaning the actual void volume fraction is between the two measured values. However, the large difference in void fraction between the two samples likely cannot be completely attributed to the elongated voids in the transverse sample. It appears that this sample had more voids to begin with, meaning the voids may not be evenly dispersed throughout the extrudate.
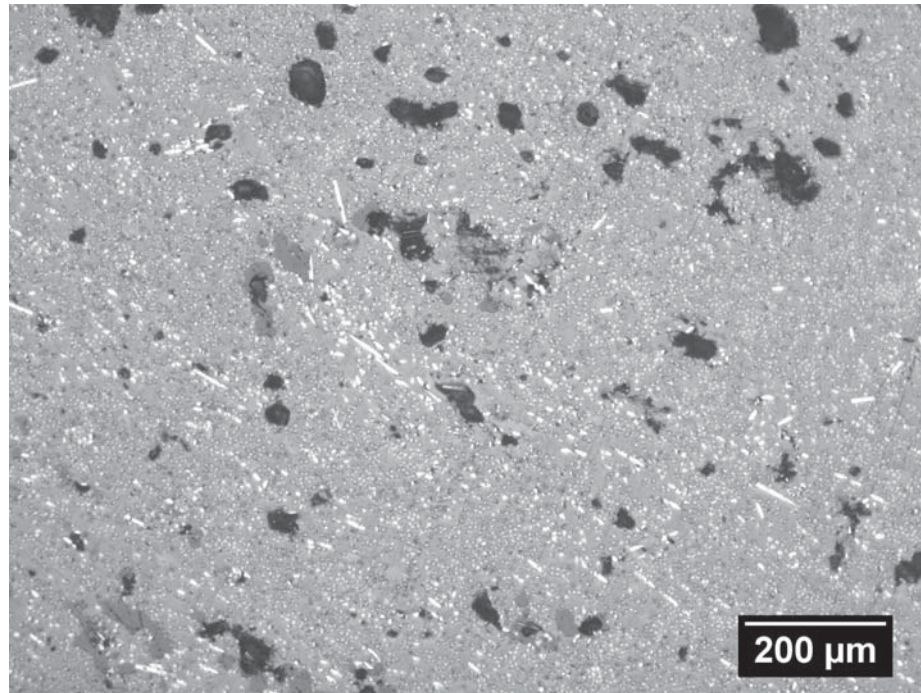
(a)
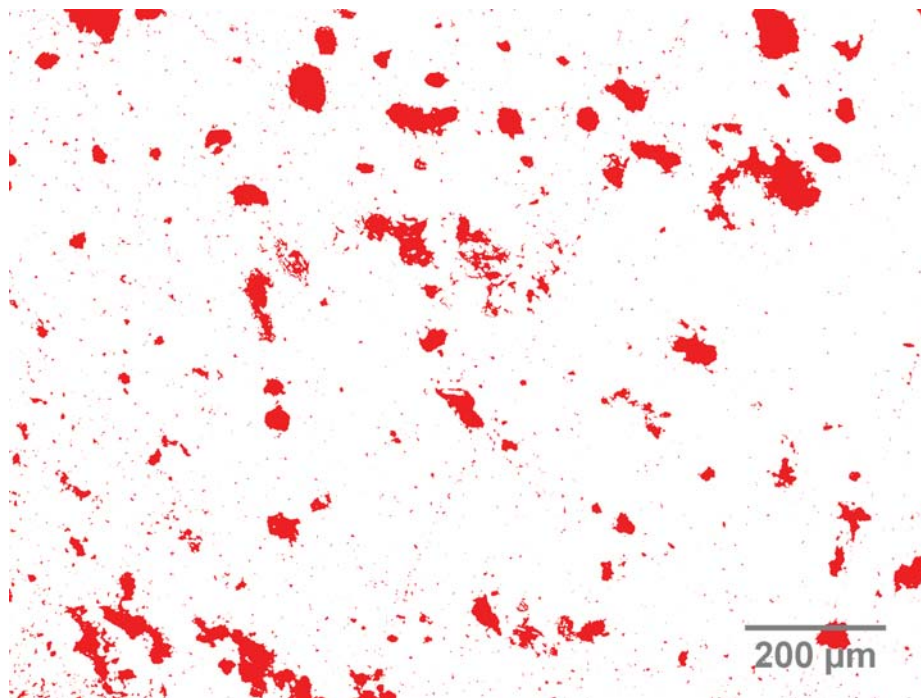
(b)

Figure 3.10.: (a) 10X optical micrograph of a longitudinal cross section and (b) thresholded voids making up 0.074 area fraction.
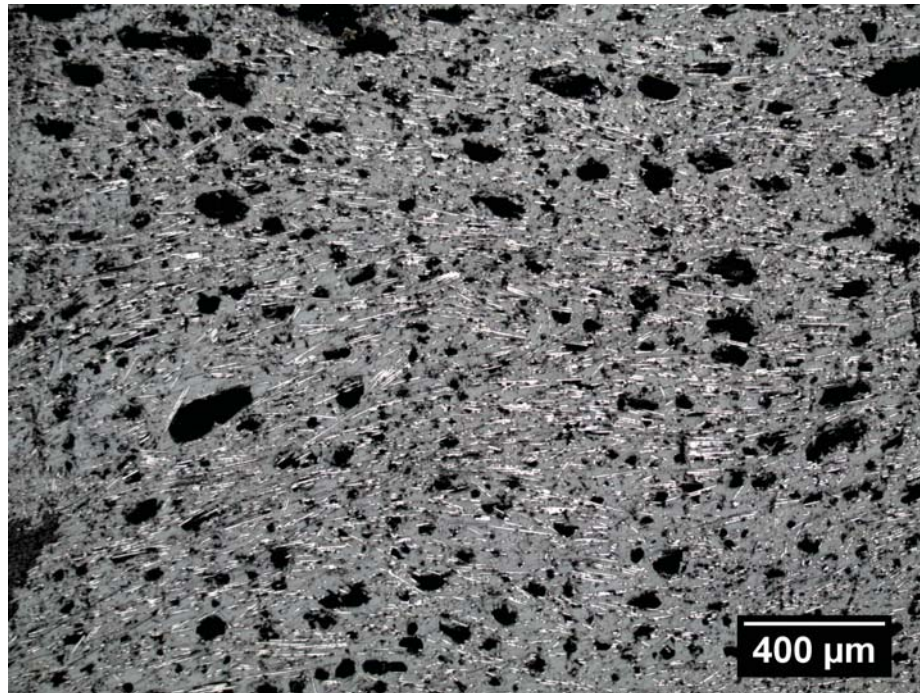
(a)
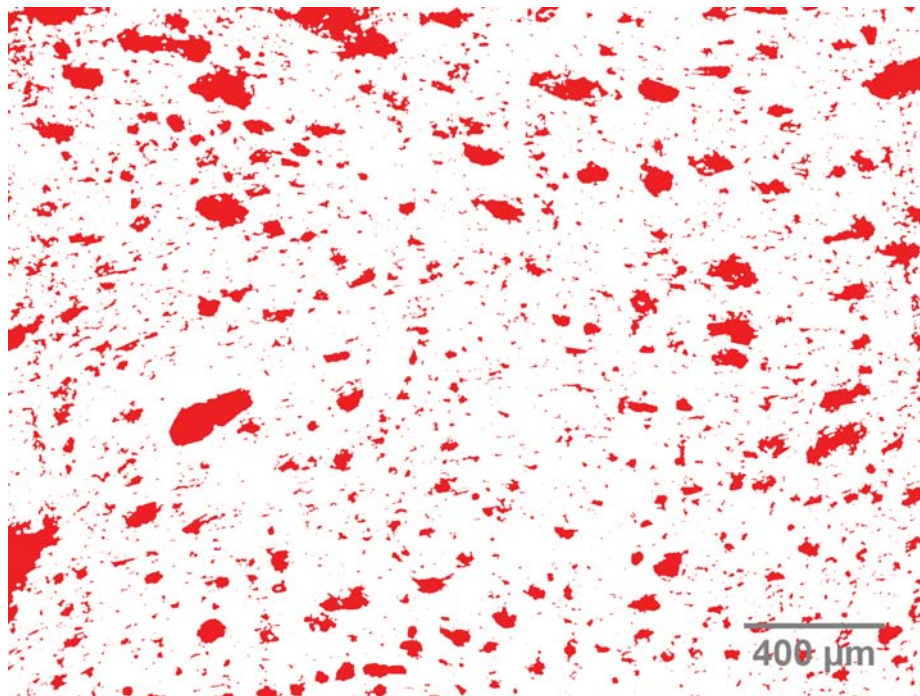
(b)

Figure 3.11.: (a) 5X optical micrograph of a transverse cross section and (b) thresholded voids making up 0.171 area fraction.

3.4   Mechanical Properties

3.4.1   Anisotropy

As illustrated in section 1.2, the inherent nature of the FDM process results in severely anisotropic properties. For parts printed from neat polymers, the print direction is the strongest direction. The two transverse directions have decreased strength due to the presence of inter-bead voids and weak bead-to-bead interfaces. These two features of the microstructure are highly influenced by the slicing parameters, extruder settings, and temperature history of the printed part.

For parts printed from fiber-reinforced polymers, the degree of anisotropy is even greater. The presence of fibers dramatically increases the mechanical properties in the print direction, but has little effect on the transverse properties. The high stiffness and strength in the print direction is a result of the high degree of fiber orientation that occurs due to the high shear forces in the polymer during extrusion through a die. Transverse to the print direction, the stiffness is dominated by the matrix properties, and the strength depends on the inter-bead size and bead-to-bead interfaces. Extruder dies capable of altering the flow field and achieving a broader fiber orientation distribution are desirable and under development by the group. This could achieve greater stiffness and strength in the transverse directions. As stated in section 1.2, the presence of fibers decreases chain mobility and hinders chain entanglement across bead-to-bead interfaces. In addition, crystallinity within the polymer likely also decreases chain mobility, and could further hinder chain entanglement across interfaces.

3.4.2   Sample Preparation

In order to investigate the mechanical properties and quantify the degree of anisotropy, tensile specimens were prepared and tested. Three square structures approximately 20 cm x 20 cm x 10 cm and 2 layers wide, shown in figure 3.12, were printed from the 50 weight percent carbon fiber-reinforced PPS. The corners were

removed using a band saw, leaving flat plates that longitudinal and transverse tensile samples could be machined from, shown in yellow and red respectively in figure 3.12. The ends of the plates were sanded, an adhesive was applied, and fiberglass epoxy tabs were bonded. Lastly, the tensile samples were machined from the tabbed plates. The dimensions of the samples are given in tables A.1 and A.2 in the appendix. Due to an error in sample preparation, both wide (W) and slender (S) transverse samples were prepared and tested, however the samples had equivalent properties.
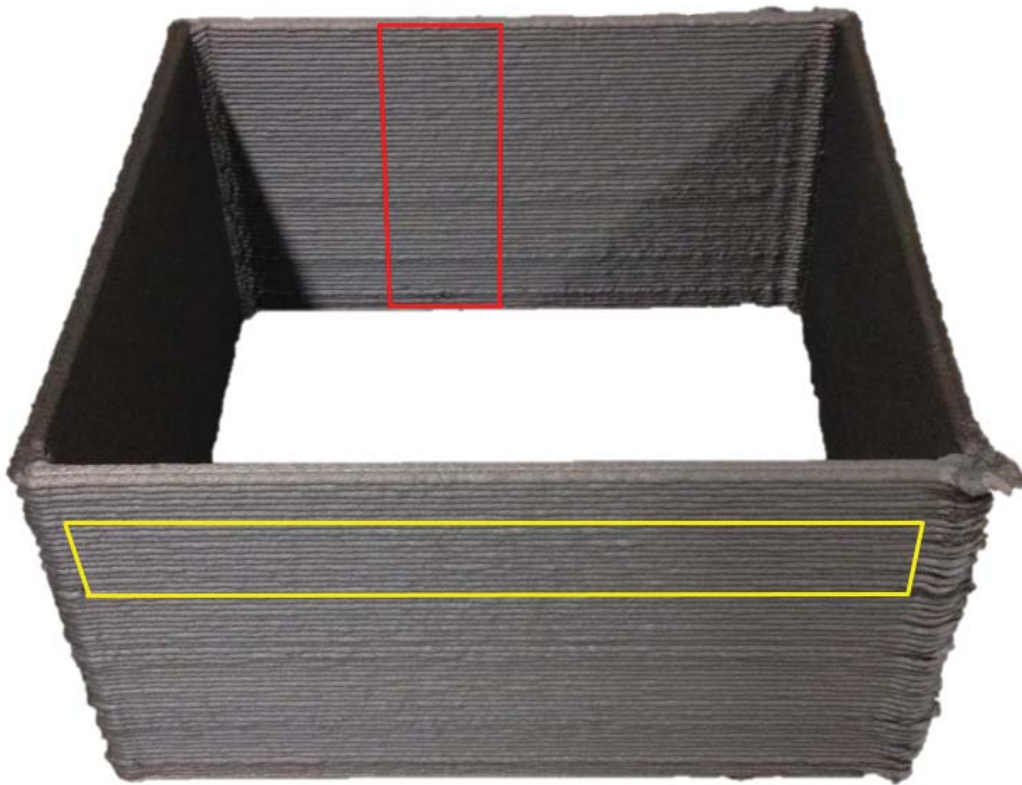
Figure 3.12.: Square structure from which longitudinal (yellow) and transverse (red) tensile samples were machined.

3.4.3 Tensile Testing

The tensile samples were tested to failure at a constant displacement of 1 mm/min. An extensometer was used to monitor strain since samples were expected to fail at low displacements. Figures 3.13 and 3.14 show longitudinal and trans-

verse samples during testing and after failure. The stress-strain curves for typical longitudinal and transverse samples are shown in figure 3.15. In both orientations, brittle behavior was observed with very low strains to failure. The mean stiffness and strength values are shown in table 3.1, and the results of the individual tests are given in tables A.1 and A.2 in the appendix. The stiffness and strength in the longitudinal direction are approximately an order of magnitude greater than in the transverse directions, attributed to the high degree of fiber orientation. The low transverse properties indicate that interlayer bonding needs improvement. The supplier spec sheet properties obtained by tensile testing injection molded dogbones (ISO 527-2/1) are also reported in table 3.1 to allow for a comparison. The stiffness and strength of the longitudinal printed samples were 37% and 40% lower than the spec sheet values, respectively. This result can likely be attributed to both the inter-bead voids which are effectively empty channels in the loading direction, and the inner-bead voids discussed in section 3.3.2. The transverse mechanical properties were not reported on spec sheet, however, they were likely greater than those of the transverse printed samples. Molded samples typically have minimal void content, and also have a broader fiber orientation distribution which provides at least some property enhancement in the transverse direction.
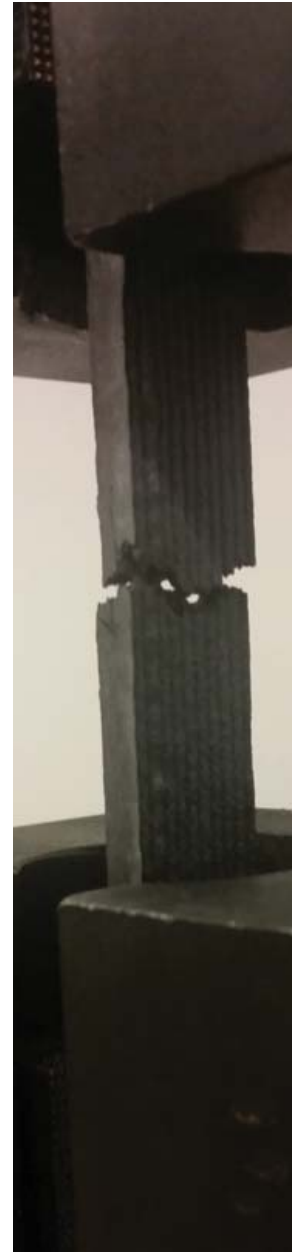
(a) (b)

Figure 3.13.: Testing of a longitudinal tensile sample (a) and sample after failure (b).

(a)   (b)

Figure 3.14.: Testing of a transverse tensile sample (a) and sample after failure(b).
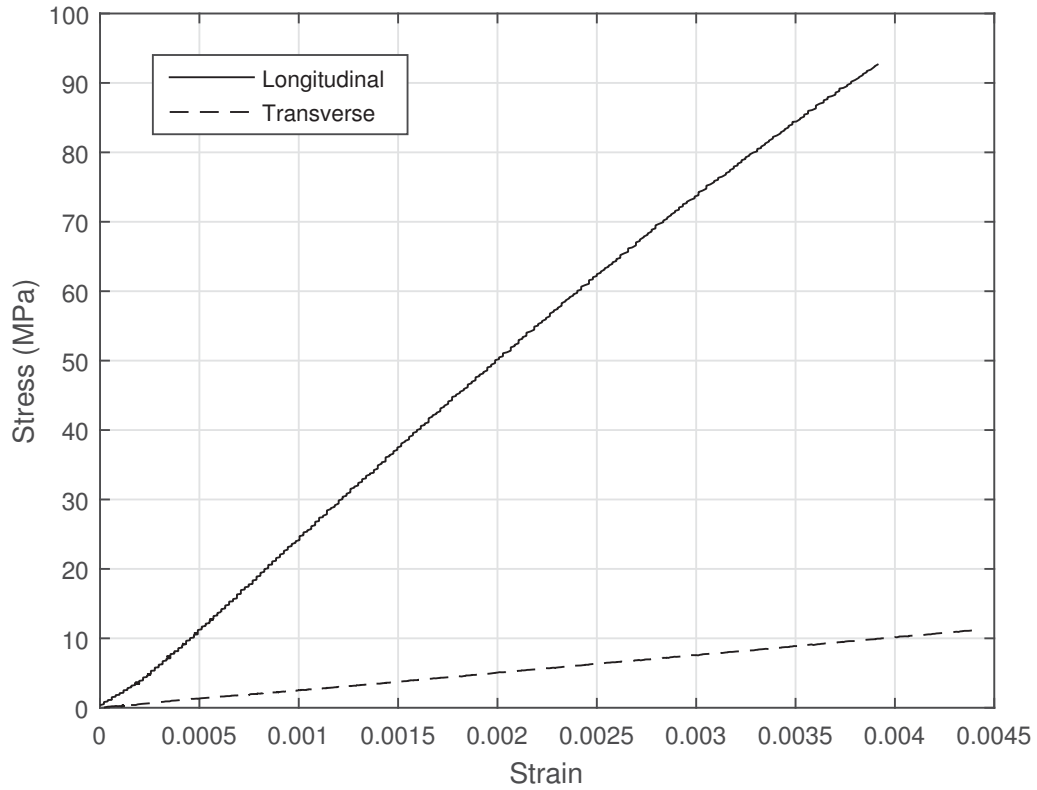
Figure 3.15.: Typical stress-strain curve for a longitudinal and transverse printed sample.

Table 3.1: Mechanical properties of longitudinal and transverse printed samples compared to spec sheet values.

	Modulus (GPa)		Strength (MPa)	
	Mean	St. Dev.	Mean	St. Dev.
Printed Longitudinal	26.38	1.18	93.22	11.27
Printed Transverse	2.60	0.23	9.72	1.44
Supplier Spec Sheet	41.7	NA	155	NA

CHAPTER 4. PROCESS AND ECONOMICS OF MANUFACTURING COMPOSITE TOOLING USING ADDITIVE MANUFACTURING

In this chapter, the target application for large-scale AM of fiber-reinforced composites, manufacturing of composite tooling, is described in detail. Composite tooling is plagued by high costs and long lead times. As a result, FDM of reinforced polymers is an attractive tool manufacturing method if the material properties meet the performance metrics and the cost savings are great enough. This chapter is a standalone section written for submission to industry conferences.

4.1   Abstract

A growing and promising application of additive manufacturing (AM) is the production of tooling [23]. Since tooling is often produced in low volumes and custom geometries for specific products, AM is very attractive. Tooling used in the manufacturing of composite parts in particular stands to largely benefit from advances in AM technologies.

The manufacturing of composite tooling usually involves wasteful subtractive processes and labor intensive steps, resulting in long lead times and high costs. Utilizing new AM technologies to manufacture composite tooling has the potential to produce significant savings in both time and cost. The past two years have seen rapid advancements in large-scale AM, most notably the development of Big Area Additive Manufacturing (BAAM) by Oak Ridge National Lab (ORNL) and Cincinnati Incorporated (CI). The large build volumes and high throughput extrusion system now attainable with a commercial gantry system make AM an attractive new method for manufacturing composite tooling. The polymers utilized in the current generation of large-scale AM machines possess lower glass transition temperatures and are

likely most suitable for tooling masters or low temperature composite prototypes. Re-searchers at Purdue University have successfully printed with carbon fiber-reinforced Polyphenylene Sulfide (PPS), which is potentially suitable for production tooling with 350°F autoclave cure cycles. In the following, the process for manufacturing the composite tool shown in Figure 4.1 using AM will be discussed and the economics will be compared to a traditional tool manufacturing process. The cost savings achieved utilizing AM to manufacture this tool were approximately 50%. As tool size and complexity increase, cost savings are expected to become even greater.
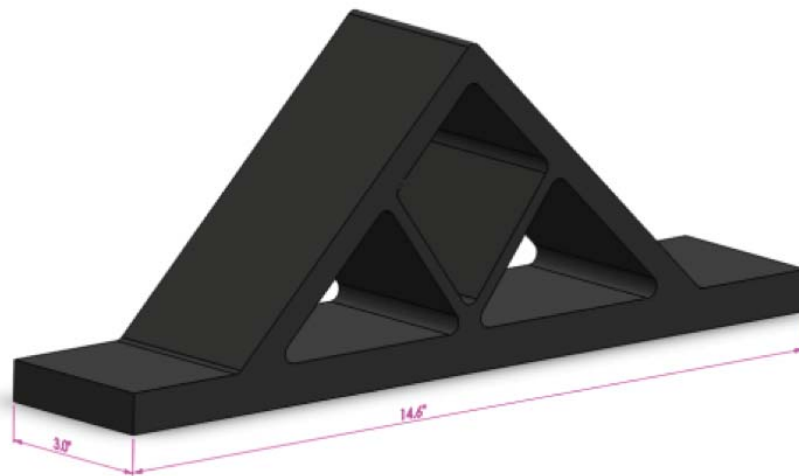
Figure 4.1.: Design of an A-frame tool to be manufactured using AM of 30 weight percent carbon fiber-reinforced polyphenylene sulfide (PPS) [24].

4.2 Introduction

4.2.1 Composite Tooling

The quality of a composite part is highly dependent on the tool that was used to manufacture it. Composite tooling must be durable, rigid and possess a coefficient of thermal expansion (CTE) matching the composite parts being produced. Typically, carbon fiber/polymer composite materials have a CTE of virtually zero in the plane of lamination. Of the metallic materials, only Invar meets these requirements. There is no shortage of new tooling technologies which claim to cut costs and meet performance

characteristics. However, contemporary practitioners have been slow to adopt these technologies, partly because the cost savings associated with them may not be great enough to motivate change.

The materials and methods used to produce tooling for composite parts vary widely depending on the type of part being produced and the production volumes. The two primary tooling materials for high performance applications are metals and composites. Metal tools are often chosen for high rate applications due to their durability and lifetime. Aluminum and steel alloys are sometimes employed, but their use is limited due to their high CTE, especially for carbon fiber parts. As stated earlier, the Nickel-Iron alloy, Invar has a CTE near that of carbon fiber and has become an industry standard for high rate production tooling. However, tools made from Invar are very costly and require long lead times, limiting their use to high rate or very expensive parts. For small parts, a metal tool is machined from a billet, and for large parts, tools incorporate a formed facesheet and backup structure.

Composite tooling can also be produced from composites. This is the ideal case for thermal expansion because the tool CTE more closely matches the part CTE. Composite tools often have inferior durability to metal tools, and are susceptible to surface damage during tool cleaning, part removal, or thermal cycling. For a very small part, a composite tool may be machined from a block of cured tooling prepreg, but more commonly composite tools also include a facesheet and backup structure similar to that of a metal tool. The process for making a composite tool has multiple cost components: master, facesheet, backup structure, and machining.

4.2.2   Additive Manufacturing of Tooling

Additive manufacturing (AM) has emerged as a new technology attractive for composite tooling applications. Well commercialized small-scale fused deposition modeling (FDM) AM technologies have been demonstrated in case studies on prototype or low rate composite tools [25]. One limitation of producing composite tooling using these technologies is the limited build volume. However, tools can be printed

in sections and then bonded together. Another limitation of contemporary AM is the inability to achieve a very low CTE because these machines are capable of printing only non-reinforced amorphous polymers. Lastly, these machines require the use of expensive polymer filament preform supplied by the manufacturer.

Big Area Additive Manufacturing (BAAM), pioneered by Oak Ridge National Lab (ORNL) and Cincinnati Incorporated (CI) has made significant advancements in the past several years [15]. Commercial machines are available with build volumes exceeding 20 x 6 x 5 feet and extruders currently capable of processing approximately 20 weight percent carbon fiber-reinforced Acrylonitrile Butadiene Styrene (ABS) and Polyphenylene Sulfide (PPS) at rates up to 100 pounds per hour [14]. These machines can process polymer pellets in various forms and from various material suppliers. Figure 4.2 shows an example of a composite layup tool printed on a BAAM machine at ORNL. Clearly, this tool consists of a facesheet and backup structure that were printed simultaneously. Secondary surface machining and coating steps followed to produce a high quality tool surface.

Figure 4.2.: Large composite tool printed from carbon fiber-reinforced-ABS on a BAAM machine developed by ORNL and CI.

Researchers at Purdue University have designed and developed an AM machine capable of processing high temperature reinforced semi-crystalline PPS with up to 50 weight percent carbon fiber. The groups goal is to further the science of AM with composites and develop models capable of predicting the various phenomena involved

in a printing process. Shown in Figure 4.3 are the initial stages of printing the support structure and surface layers for a hemispherical tool geometry.

Figure 4.3.: Parts printed from 50 weight percent carbon fiber-reinforced PPS on an AM machine developed at Purdue University.

4.2.3 Feasibility of AM Tooling

For the production of thermoset glass or carbon fiber composite parts that cure at ambient or low temperatures, tooling dimensional control may not be critical. The tooling materials for these uses may include wood/plaster, foams, fiberglass and low cost alloys. Although these are relatively low cost materials, the processes used to make tools from them require multiple labor intensive and lengthy steps. AM with low cost carbon fiber-reinforced ABS ($4 per pound) is attractive for these applications, and could rapidly produce tooling suitable for prototypes or short rate production. For high performance autoclave composites curing at 250-350°F, reinforced ABS will not be a suitable material due to its lower glass transition temperature T_g. However, printing masters from reinforced ABS and then making a traditional composite tool

from that master is likely cost effective in certain applications. In contrast, carbon fiber-reinforced PPS possesses suitable properties to serve as a tool for a high temperature autoclave cured carbon fiber parts in the 250°F range, and possibly at greater temperatures.

The following sections outline the process for making a composite tool from carbon fiber-reinforced PPS with AM. The tool geometry chosen was an A-frame as shown in Figure 4.1. The performance of the tool was evaluated by out-of-autoclave curing a carbon fiber/epoxy prepreg composite part at 225°F on the tool. This tool may be suitable for an autoclave cure as well since the softening temperature of carbon fiber-reinforced PPS is adequate to meet these needs. The economics of manufacturing the tool using this method are presented and compared to a traditional tool manufacturing process in the following.

4.3   Procedure

4.3.1   Manufacturing of the Tool

Three steps are involved when utilizing AM to manufacture a composite tool:

1. Design

2. Print

3. Machine

4.3.1.1. Design

The process for designing a tool to be manufactured using AM will vary depending on the desired part geometry. Although the tool geometry illustrated is largely planar, the process below is general to many part geometries and is sufficient for illustrating a broad-ranging method.

Typical AM processes build in a layer by layer fashion with solid layers at the surfaces and partially infilled layers providing the support structure. Boundary, surface, and infill parameters are specified in the slicer program. The slicer program

converts the three-dimensional geometric file to the G-code that drives the process. Although suitable when printing final parts, this method may not succeed in every case when printing a part that requires a final machining process. This is because the slicer applications do not yet offer enough flexibility around infill settings. In most cases, it is not possible to ensure that a solid infill would exist in all areas that are to be machined, which could lead to machining through the surface. Therefore, the current best practice when printing tooling is to print the tool with its surface perpendicular to the print bed. This gives the most flexibility in surface thickness and backup structure. Figure 4.4 shows the orientation of the tool on the print bed and the printing path generated by the slicer for the tool. The tool must be printed in scaled up dimensions to ensure that the surface resides somewhere near the middle of the beads after machining.
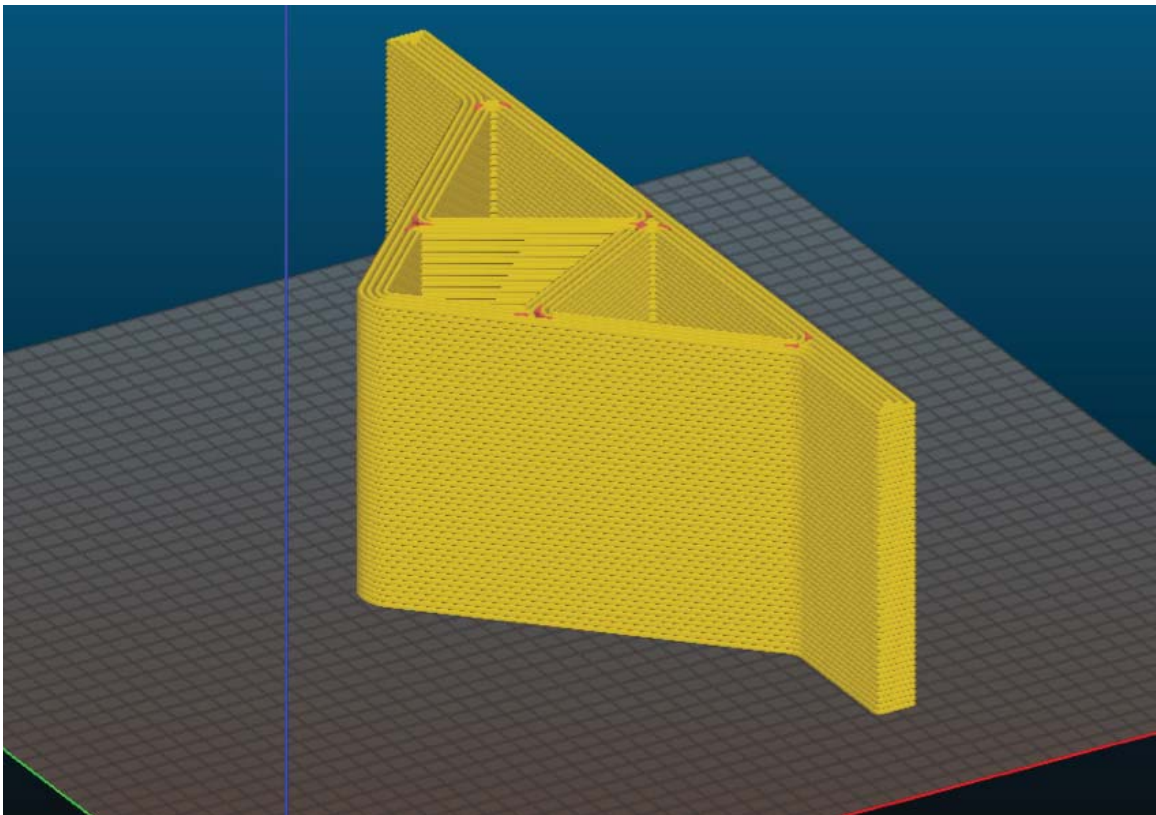
Figure 4.4.: Tool orientation and print path generated by the slicer prior to printing.

4.3.1.2. Printing

The tool was printed on a system designed and developed by the Purdue University AM research group. The machine features a single screw extruder with a max temperature of 750°F. The feedstock material was 30 weight percent carbon fiber-reinforced PPS pultruded pellets supplied by Celanese. The tool was printed onto a heated bed at 464°F and the material was extruded at 610°F and at a rate of 6 pounds per hour. A printing speed of 200 inches per minute led to a total print time of approximately 15 minutes.

4.3.1.3. Machining

Machining the tool first required creating a tool path for a 5-axis CNC using CAM-Works. A single-step finishing tool path was generated using a inch diameter ball mill engineered for machining composites. In order to achieve a gouge-free surface, a step-over of 0.2 mm and a cut depth of 1.5 mm were used in the tool path. The printed surface was machined down to the center of the deposited beads, producing a surface free from large inter-bead voids. A smooth surface finish was achieved using the cutting speeds recommended by the tool manufacturer. The feed speed was set to 350 inches per minute which gave rise to a machining time of approximately 20 minutes.

4.3.2   Manufacturing of the Carbon Fiber Bracket

4.3.2.1. Tool Preparation

In practice, the surface of a tool produced using AM may require a filling compound and coating to fill any surface voids and ensure a perfect tool surface finish. The coating would also protect the tool from surface damage resulting from tool cleaning, de-molding, or weave pattern print-through. For this experiment, the tool was only lightly coated with an epoxy and sanded to fill any large voids.

4.3.2.2. Layup and Cure Process

Prior to layup of the prepreg on the tool, a liquid PTFE mold release was applied. The AX-5204 prepreg system from Axiom Materials was used to manufacture an angle bracket. Eight plies were laid up in a balanced and symmetric laminate on the tool surface and the tool was envelope bagged. The bracket was out-of-autoclave cured at 225°F for 2 hours on the AM tool and was easily removed after the cure. The tool showed no signs of damage or deformation after the cure process. However, weave print-through (thermoset resin remained on the tool surface in the weave pattern) was observed on the tool. Figure 4.5 shows the tool and part after the cure. The difference in CTE inplane and through thickness for the tool resulted in the bracket curing in a closed in angle.

Figure 4.5.: top) The bracket prior to removal from the tool; bottom) Observed gap between tool and part surface.

4.4   Economics

4.4.1   Direct Cost Comparison

The cost to produce this tool was $630, as will be described in the following. To make this tool using a traditional carbon fiber tool manufacturing process, the tool would have cost approximately $1,252. Section 4.4.1.1 illustrates the process and cost breakdown for each method. Utilizing AM for composite tool making results in direct cost savings due to decreased material costs, reduced machine time, and reduced labor. As tool size increases, the cost savings are expected to become greater.

4.4.1.1. Process Descriptions

Manufacturing the tool using AM required three steps: design, print, and machine. The 3 hours of design time includes generating the tool geometry, print path, and machining tool path. Although the print time was approximately 15 minutes, one hour of machine time is used in the analysis to allow for set-up time. It is assumed that machine time on an AM machine capable of processing carbon fiber-reinforced polymers can be purchased for $200 per hour. This is an estimate and may not currently be the case since very few of these machines exist in the marketplace. However, it is judged to be a good working number. One hour of machining time at $250 per hour is used and leaves adequate set-up time.

The process for making the same A-frame tool from carbon fiber involves four steps: design, prepare tooling board, machine the master, and layup and cure tool. The 5 hours of design time includes generating the tool geometry and machining tool path. One hour is given for cutting and bonding tooling board estimated to cost $1400 per cubic foot. Machining the master is estimated to take 1.5 hours at $250 per hour. Laying up and curing the tool are assumed to take 4 hours at $50 per hour utilizing 3/4 pound of tooling prepreg at $100 per pound. This last step likely underestimates the real cost as autoclave cure cycles are costly, and a post cure is often required for carbon fiber tools. In addition, it is assumed that no backup structure is required for this tool. For larger tools, backup structure must be machined and bonded to

the facesheet, adding significant costs. Figure 4.6 and tables 1 and 2 summarize the two methods and compare the final costs. Cost savings of approximately 50% were achieved by utilizing AM to manufacture the tool.

Additive Manufacturing

Design
3 hrs @ $50/hr:
Total: $150

Print
1 hr @ $200/hr
Feedstock: 1.5lbs @ $20/lb
Total: $230

Machine
1 hr @ $250/hr
Total: $250

Traditional Process

Design
5 hrs @ $50/hr
Total: $250

Tooling Board
1 hr @ $100/hr
.18 cu ft @ $1400/cu ft
Total: $352

Machine Master
1.5 hrs @ $250/hr
Total: $375

Layup & Cure Tool
4 hrs @ 50/hr
.75 lb tooling prepreg @ $100/lb
Total: $275
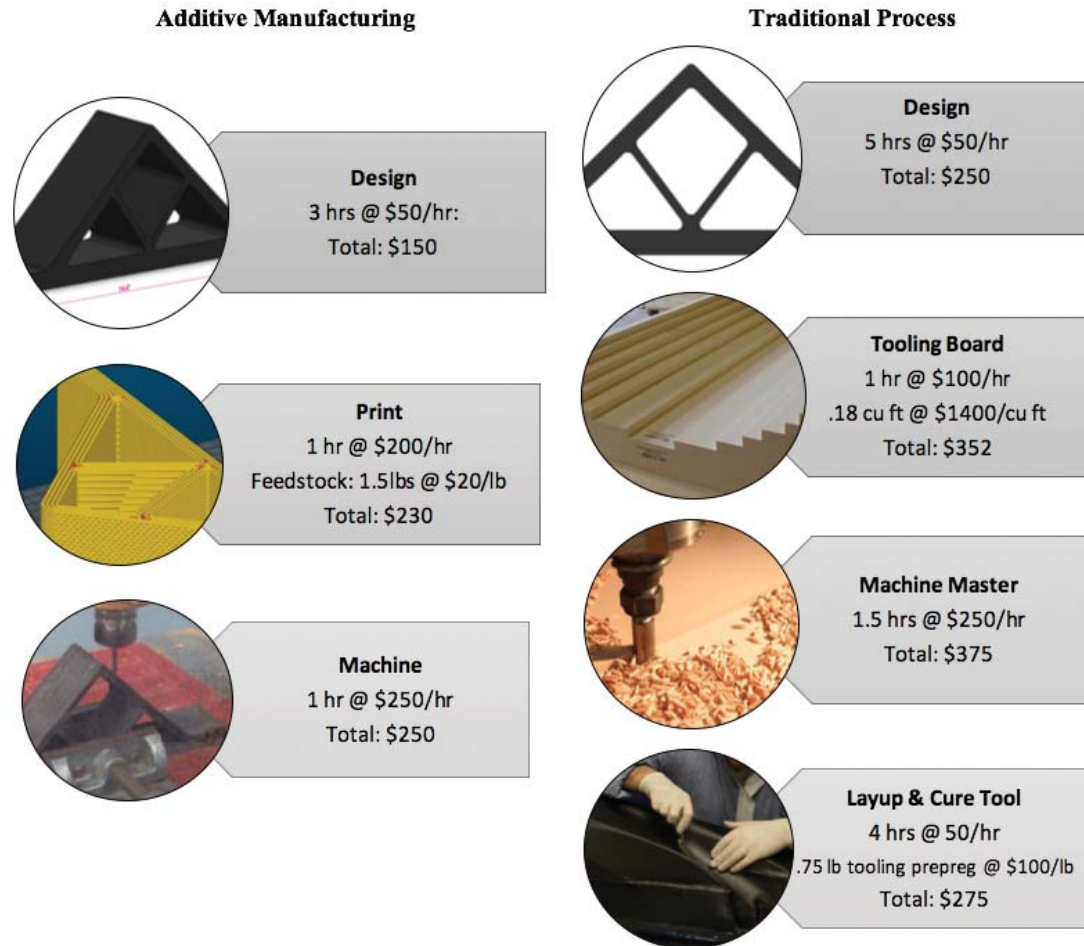
Figure 4.6.: Process steps and inputs for manufacturing the A-frame tool using AM and a traditional carbon fiber tool manufacturing process.

4.5   Other Benefits of AM Tooling

In addition to the direct cost savings that can be achieved using AM to produce tooling, AM offers additional significant advantages. Current lead times for composite tooling often span weeks or months if tooling is not produced in-house. AM offers the ability to drastically decrease lead times, which translates to shorter delivery times

and accelerated product development cycles. In fact, lead time reductions of up to 90% have been reported as a result of AM made tooling [23]. For companies that produce tooling in-house, purchasing a large-scale AM machine could still drastically reduce tool manufacturing times. Current tool making processes require many material inputs and extensive labor. If a tool was to be made from Invar or tooling boards, it may take weeks for the correct sized blocks to arrive. An AM machine can readily print any shape with little to no set up time and supervision.

The high cost of composite tooling restricts composites to expensive or high volume applications. The cost savings and reduced lead times achievable with large-scale AM could drastically alter the economics of composites manufacturing. New applications previously not financially feasible could suddenly emerge as contenders for composites. Economic order quantities could greatly decrease if tools cost 1/10th the price, making low volume applications attractive, even down to individual custom parts. The high-mix low-volume composites environments would thrive if this paradigm shift in tool making could take place.

4.6   Current Limitations of AM Tooling

As with any emerging technology, problems still remain to be solved prior to acceptance beyond early adopters. The extrusion of fiber-reinforced polymers in this AM process typically results in significant fiber orientation in the direction of deposition. Thus, the final CTE of the extrudate and the tool are highly anisotropic. This can present issues when matching tooling CTE to that of the part being manufactured. In the future, tools may be printed in multiple sections, such as printing backup structure first and then a tool surface of varying bead orientations on top of it. The A-frame tool made from 30 weight percent carbon fiber-reinforced PPS experienced slight expansion through thickness during the cure process. Where tight tolerances are required, greater fiber content materials and increased backup structure should be used.

Temperature gradients that develop during printing give rise to sometimes detrimental residual stresses when printing large parts [15]. An ideal solution would involve designing smart print paths in a way to lessen these effects. Models are under development and must advance in order to make smart print path generation a reality.

4.7   Conclusion

The cost savings that can be achieved by utilizing AM in the production of composite tooling were demonstrated and estimated to be 50% for a small tool. The savings are expected to become greater as tool size and complexity increases. The current materials that large-scale commercial machines can print are likely suitable for indirect rapid tool making, or making masters that will be used to make tools. The technology is advancing quickly and the commercial machines will soon be moving to third generation customized AM extruders. These machines will likely be printing high fiber content and high temperature polymers suitable for autoclave tools in the near future. The objective of this paper is to motivate both early adopters in industry and researchers around the world to continue to uncover new applications and contribute to this exciting field with much promise and potential.

CHAPTER 5. VISCOELASTIC PROPERTIES OF POLYMERS

This chapter serves to summarize the fundamentals and mechanisms behind viscoelasticity. The effects of time and temperature on the behavior of polymers will be emphasized. Although important in many applications, the effect of the frequency of an applied load on the behavior of the polymer is not applicable in this research. Dynamic mechanical analysis, creep, and stress relaxation tests will be described, and used to characterize carbon fiber-reinforced PPS in chapter 6.

5.1   Overview

The two main classifications of ideal materials are elastic solids and viscous liquids. An elastic solid is a material with a definite shape, which can be deformed by external forces to take on a new shape. Elastic solids are capable of storing all energy imparted by the external loads, and thus the original shape is restored when the external forces are removed. On the contrary, viscous liquids have no definite shape, and external forces result in irreversible flow. Polymers are unique in that they can exhibit a range of properties between elastic solids and viscous liquids, depending on the timescale, temperature, and frequency of applied loads [26]. This form of behavior that combines both liquid-like and solid-like characteristics is termed viscoelasticity.

In engineering, designs are often based on the stiffness properties of the materials in use. Young's modulus is used to ensure elastic deformations remain below some critical limit specified in the design. The modulus of metals and ceramics does not show a strong temperature, frequency, or time dependence at moderate temperatures. However, this is not the case with polymers, which exhibit some viscoelastic behavior at all temperatures [27]. The stiffness properties of polymers are highly dependent on

temperature, frequency, and time, therefore these effects must be taken into account in the design and performance evaluation of polymer components.

To evaluate the use of a polymer in a composite tooling application, an understanding of the temperature and time dependence of the polymer's behavior is of paramount importance. Composite tools are subjected to high temperatures and pressures, and maintaining dimensional stability is critical in order to produce the desired part geometry. An understanding of the viscoelastic properties is also required to accurately predict the outcome of large-scale AM processes. As stated in previous sections, residual stresses arise during FDM printing processes, and can lead to warping and/or detrimental layer delamination. Due to their viscoelastic nature, polymers can undergo stress relaxation, a phenomena which is desirable in large-scale AM. Predicting the degree to which stress relaxation can occur allows for optimization of the printing process, improved design for additive manufacturability, and determination of post-printing procedures required for printed parts that will serve as tooling.

5.2   Mechanisms

The time and temperature dependence of properties in polymers is a direct result of their long molecular chain structure. Under an applied load, a polymer can deform by one or both of two mechanisms. In the first mechanism, the lengths and angles of chemical bonds can be stretched to a position of higher internal energy [28]. This mechanism results in small deformations in quick timescales. The second mechanism involves a rearrangement of atoms, either through side group motion, chain conformations, or chain extensions, some of which will decrease entropy [28]. The rate of this mechanism has a strong dependence on the mobility of the molecules. The mobility is affected by multiple factors, namely the structure of the molecule and the temperature [28]. The "free volume" or space within the polymer not occupied by molecules, increases with temperature, thereby allowing greater molecular motion [29].

The temperature dependence of the rate of molecular motion can be approximated by an Arrhenius-type expression in the form of

$$rate \propto exp\frac{-E^{\dagger}}{RT} \tag{5.1}$$

where $E^{\dagger}$ is activation energy, R is the Gas Constant, and T is temperature [28].

A graphical representation of the expression is shown in figure 5.1. At temperatures far below the T_g, a polymer is referred to as "glassy." In this region, the free volume is small, and chains are essentially frozen. Conformations and rearrangements of chains, as well as relative motion between adjacent chains is inhibited [29]. If placed under load, a polymer in this region can only deform through the first mechanism, stretching of bonds, which occurs at high rates and is quickly reversed when the load is removed [28]. A polymer is most brittle and has the highest modulus in its "glassy" state. The region centered around the T_g, known as the "leathery" region, is where viscoelastic behavior is most prominent. In this region, temperature increases lead to greater increases in free volume, which enables greater chain mobility. If placed under a load, this chain mobility gives rise to a time dependent viscous component in addition to the elastic response, resulting in the observed viscoelastic behavior. At temperatures far above the T_g but below the T_m, a polymer becomes "rubbery," where free volume and chain mobility increase further. Under an applied load, large but recoverable deformations occur, giving rise to a lower modulus.
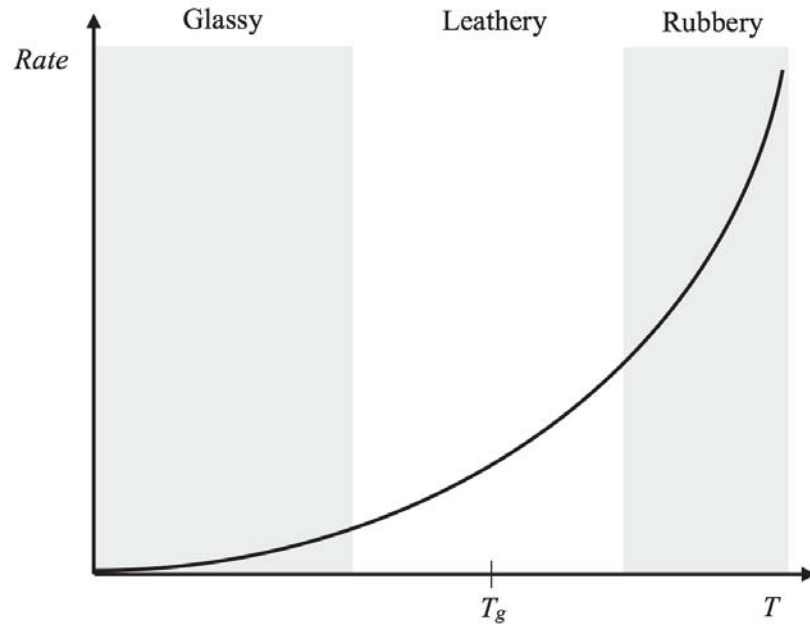
Figure 5.1.: Rate of molecular motion versus temperature [28].

As stated, the modulus of a polymer has a strong temperature dependence that must be understood and accounted for in design and engineering. Figure 5.2 shows a plot of the 10 second relaxation modulus of polystyrene versus temperature (the 10 second relaxation modulus can be used to characterize the modulus dependence on temperature and will be defined in section 5.4.3). The same regions shown in figure 5.1 are illustrated, and the temperature range is extended to show the two additional regions, giving the five regions of viscoelastic behavior: glassy, leathery or transition, rubbery, rubbery flow, and liquid flow. The 3 curves represent different structures of polystyrene: crystalline (A), lightly cross-linked (B), and amorphous (C).
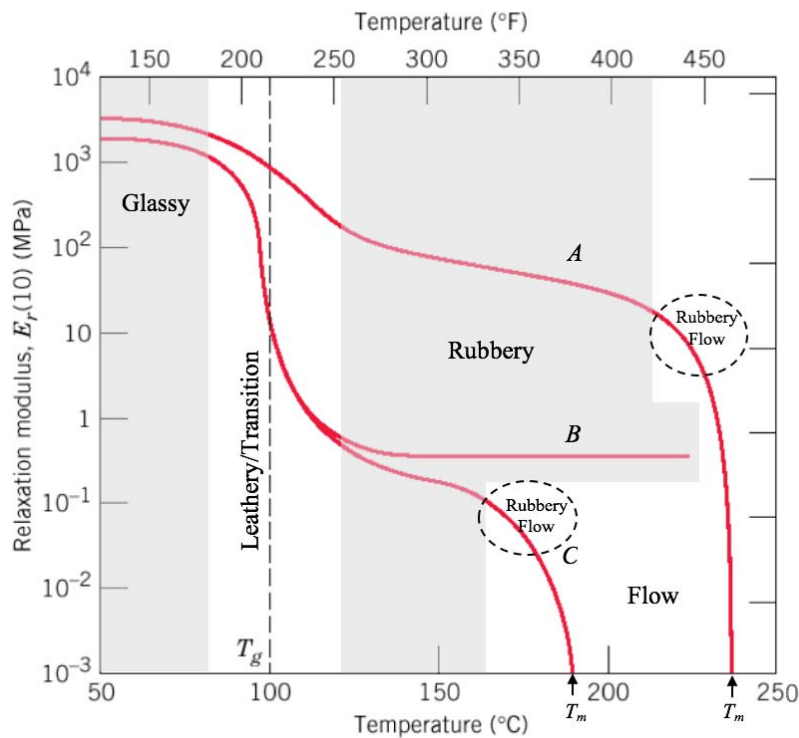
Figure 5.2.: Temperature dependence of the 10 second relaxation modulus for (A) crystalline, (B) cross-linked, and (C) amorphous polystyrene [29].

The structure of a polymer strongly influences its modulus dependence on temperature. Since the T_g is a phenomena observed in amorphous regions of polymers, the change in properties observed at the T_g is highly dependent on the degree of crystallinity in the polymer. The modulus of the crystalline polystyrene does not experience the same dramatic drop in the transition region as the other two structures. The modulus still decays, but plateaus at a higher value than the amorphous structure. Spherulites increase the modulus above the T_g through at least two mechanisms [30]. In the first, the spherulites tie sections of molecules together, similar to cross-links. In the second, the spherulites with their high stiffness act as rigid fillers in the rubbery amorphous regions. The effects of spherulites last until the T_m is approached, where irreversible flow behavior takes over. The T_m generally increases as the degree of crystallinity increases [31].

As observed in the crystalline polystyrene, the modulus of crystalline polymers typically continues to decay slightly in the rubbery plateau region. This can be attributed to small and/or imperfect spherulites melting before the T_m, reducing the cross-link and rigid filler mechanisms [31]. Thermal expansion also serves to increase free volume, and therefore contributes to the slight decrease in modulus as well [31].

A plateau at a lower modulus results in the amorphous polymers, as shown in the amorphous polystyrene sample. The plateau arises due to molecular entanglements which serve to hinder chain mobility. Upon further heating the rubbery flow region is reached, where irreversible molecular motion begins. As the T_m is approached, the secondary bonds between chains diminish, allowing chains to move freely [27].

Although crystallinity can greatly affect the modulus above T_g, the modulus below the T_g remains mostly unchanged [31]. Crystallinity also typically has little effect on the T_g. However, if crystallized under specific conditions, certain polymers exhibit a higher T_g [31, 32, 33]. This is believed to be due to amorphous segments existing only as short sections between spherulites or stresses induced on amorphous segments from the crystallization process. In both of these scenarios, mobility is hindered, requiring higher temperatures to restore it.

The lightly cross-linked polystyrene also displays a rubbery plateau, attributed to the cross-links hindering chain motion. The rubbery plateau remains until the material is raised to a temperature where degradation occurs, which appears similar to a flow region if plotted [29].

5.3   Influence of Fillers

Figure 5.3 illustrates the effect of the addition of fillers on the modulus-temperature curves for amorphous and crystalline polymers. In general, the fillers increase the modulus of the polymer across all temperatures, leaving the shape of the curves mostly unchanged. An important performance metric to consider when evaluating the use of reinforced polymers for composite tooling applications is the heat distortion temperature (HDT), an ASTM standard which specifies the temperature at which a material

will deflect under a specific load. Reinforcing polymers with fibers greatly increases the HDT [34, 35, 36], another reason for the attractiveness of fiber-reinforcement in tooling. Similar to the increase in the T_g depicted in figure 5.3, the increase in the HDT tends to be greater in reinforced crystalline rather than amorphous polymers, with the HDT sometimes approaching the melting point in crystalline polymers [37]. In amorphous polymers, the increase in the HDT is an apparent rather than actual increase since it is due to the decreased creep rate arising from the higher modulus, as opposed to truly increasing the softening or glass transition temperatures [31]. The HDT increase observed in crystalline polymers is mainly a result of the increased modulus.
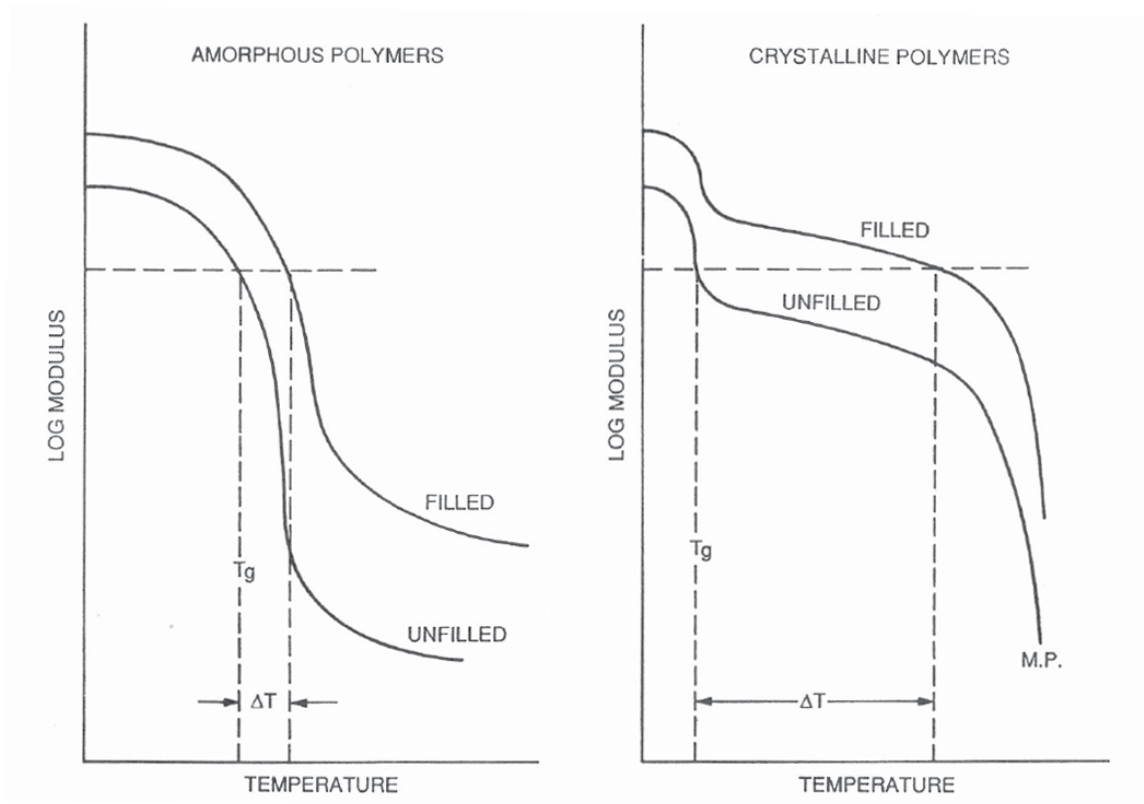
Figure 5.3.: Effect of fillers in amorphous and crystalline polymers [31].

5.4   Viscoelastic Property Characterization

The previous sections introduced viscoelasticity and the time and temperature dependent properties of polymers. Multiple approaches utilized to characterize these properties will be outlined in the following sections.

5.4.1   Dynamic Mechanical Analysis

5.4.1.1. Overview

The sinusoidal oscillatory test, or Dynamic Mechanical Analysis (DMA), is a common method used to analyze the viscoelastic properties of polymers. An instrument applies an oscillating strain or stress to a specimen and measures the sinusoidal response. For a linear viscoelastic material, this response lags behind a certain amount, depending on how elastic and/or viscous the behavior of a particular polymer is at the given conditions. The results of a DMA test can be separated into the elastic and viscous components, providing insight into the structure and performance of a polymer. DMA tests can be conducted over various temperatures, frequencies, and times.

Figure 5.4 demonstrates DMA tests in which alternating stresses are applied to an elastic, viscous, and viscoelastic material and the resulting strains are measured. For a perfectly elastic material (A), the stress and strain are in phase, giving a phase lag δ of 0°. For the purely viscous material (B), the strain lags behind the stress a δ of 90°. For the viscoelastic material (C), the δ is between 0° and 90°. A low δ corresponds to a highly elastic material and a high δ corresponds to a highly viscous material. Most polymers have δ values in the range of a couple degrees, but at temperatures in the glass transition region, δ values can reach 30°.
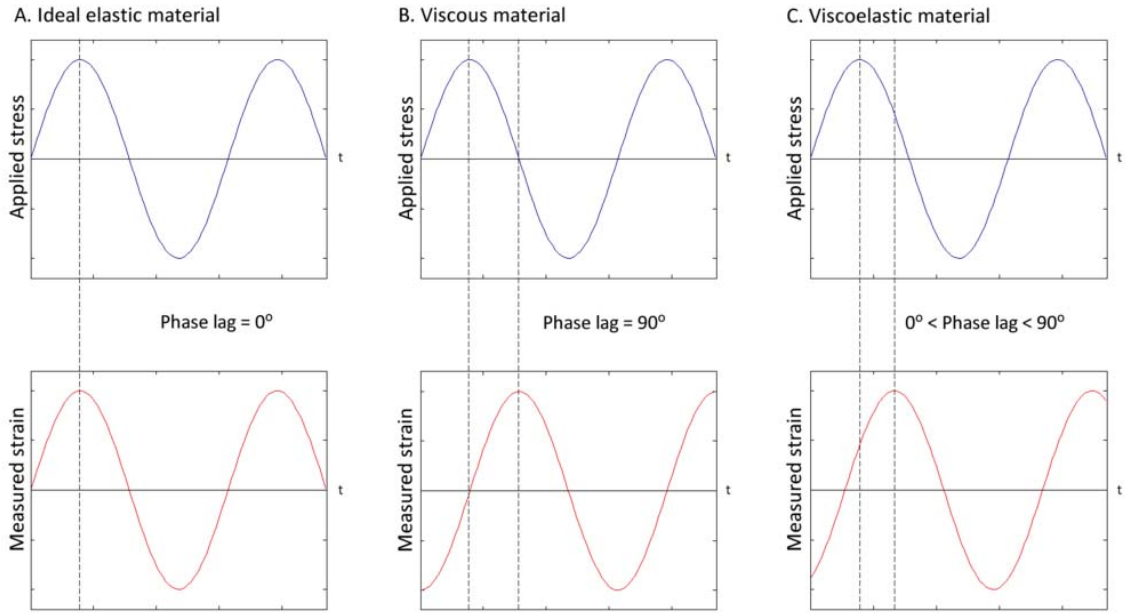
Figure 5.4.: DMA tests showing applied stress (above) and measured strain (below) for an elastic, viscous, and viscoelastic material.

In a DMA experiment where an alternating strain is applied and the resulting stress is measured, the strain e and stress σ can be represented by

$$e = e_0 sin(\omega t) \tag{5.2}$$

and

$$\sigma = \sigma_0 sin(\omega t + \delta) \tag{5.3}$$

where e_0 is the max strain, σ_0 is the max stress, ω is angular frequency, and δ is the phase lag [26]. Expanding 5.3 gives

$$\sigma = \sigma_0 sin(\omega t)cos(\delta) + \sigma_0 cos(\omega t)sin(\delta), \tag{5.4}$$

showing that stress consists of two components: one that is in phase with the strain $(\sigma_0 cos(\delta))$ and one that is $90°$ out of phase $(\sigma_0 sin(\delta))$ [26]. This stress-strain relationship can then be defined using E' and E'' giving

$$\sigma = e_0 E' sin(\omega t) + e_0 E'' cos(\omega t), \tag{5.5}$$

where

$$E' = \frac{\sigma_0}{e_0} cos(\delta) \tag{5.6}$$

and

$$E'' = \frac{\sigma_0}{e_0} sin(\delta). \tag{5.7}$$

$E' e_0$ represents the in phase component of the stress and $E'' e_0$ represents the $90°$ out of phase component. Figure 5.5 is a phasor diagram showing that E' and E'' define a complex modulus E^*.
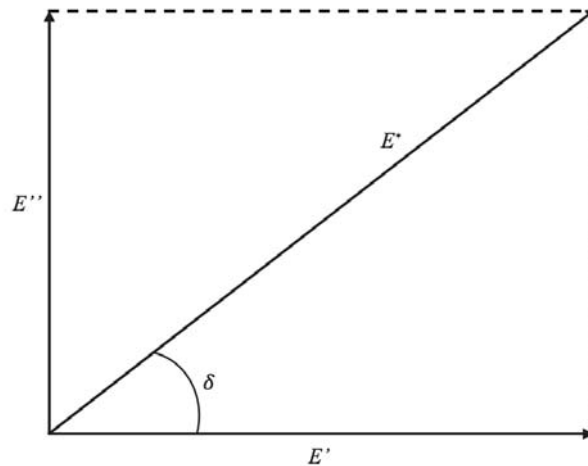
Figure 5.5.: Phasor diagram for complex modulus.

If

$$e = e_0 exp(i\omega t) \tag{5.8}$$

and

$$\sigma = \sigma_0 exp[i(\omega t + \delta)], \tag{5.9}$$

then

$$E^* = \frac{\sigma}{e} = \frac{\sigma_0}{e_0}exp(i\delta) = \frac{\sigma_0}{e_0}(cos(\delta) + isin(\delta)) = E' + iE'' \qquad (5.10)$$

E' and E'' are called the storage and loss modulus respectively and are related to the energy that is stored and lost during a load cycle. The storage modulus is the elastic component and represents the ability of the material to store energy in elastic strain. The loss modulus is the viscous component and represents the ability of the material to dissipate energy through heat arising from friction during molecular motion. The loss tangent, written

$$tan(\delta) = \frac{E''}{E'} \qquad (5.11)$$

is the ratio of E'' to E' and represents the index of viscoelasticity. The elastic component dominates at low $tan(\delta)$ values and the viscous at high values.

5.4.1.2. Typical DMA Experiments and Results

Temperature and frequency sweep experiments are common DMA tests to determine the effects of temperature and frequency on the performance of a material. In general, the effects seen at low temperatures are analogous to the effects seen at high frequency, and vise versa [29]. The temperature sweep test is most relevant to our research since it is capable of measuring polymers properties across a wide temperature spectrum. This is necessary when evaluating whether or not print materials are suitable for composite tooling applications. As explained in chapter 4, composite tools must retain their precise geometry when exposed to elevated pressures and temperatures in an autoclave cure process, therefore identifying temperatures where any changes in mechanical properties result is essential to determine use limits.

In a temperature sweep test the frequency and amplitude of the applied stress or strain are held constant, and the temperature is increased either in a stepwise fashion or continuously. The variation of the storage modulus, loss modulus, and $tan(\delta)$ are plotted against temperature, providing insight into the properties of the material. This method is often used to determine the T_g or other transitions, observe changes in structure with temperature, and evaluate the effects of cross linking or

crystallinity. An example temperature sweep DMA test is shown in figure 5.6 for illustrative purposes.
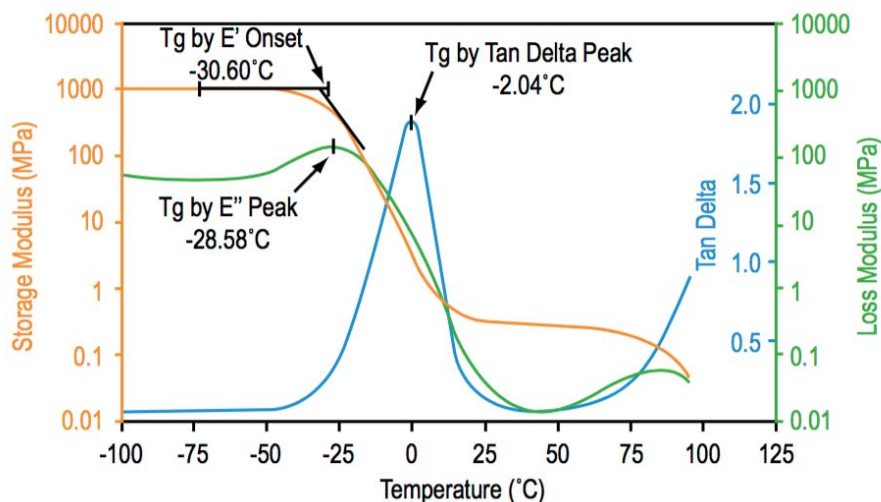
Figure 5.6.: Variation of storage modulus, loss modulus, and $tan(\delta)$ with temperature [38].

Initially, the storage modulus remains mostly unchanged due to the polymer being in a glassy state. Slight dips in the modulus can result if minor transitions occur, such as side group motion being enabled. In the glass transition region, the storage modulus drops dramatically since much less energy can be stored in elastic strain due to molecular motion being enabled. In the next region, the storage modulus levels, with the magnitude and duration of this plateau influenced by chain entanglements, cross-links, and crystallinity. Upon further heating, the crystalline regions melt and the polymer begins to flow, causing the storage modulus to decay further.

Similar to the storage modulus, the loss modulus typically remains mostly unchanged until the glass transition range. When molecular motions are initially enabled, they occur with difficulty, and the friction dissipates much of the energy as heat. This explains the increase in loss modulus through the glass transition region. Upon further heating, molecular motions occur with less friction, dissipating less energy and thus leading to a decrease in loss modulus. The temperature at which the

loss modulus peaks is often taken as the T_g of the material, however the temperature at which the storage modulus begins to dramatically decrease or where $tan(\delta)$ peaks is also sometimes used to identify the T_g.

5.4.2 Creep

In addition to DMA, the creep test is another common viscoelastic characterization method and is used to measure the time dependent strain of a polymer under a load. Understanding the creep behavior of a polymer is essential to ensure it will perform as expected in load bearing applications. In a creep test, shown in figure 5.7, a load σ_0 is applied, and the time dependent strain $\epsilon(t)$ is monitored, defining a quantity known as the creep compliance,

$$D(t) = \frac{\epsilon(t)}{\sigma_0}. \tag{5.12}$$

For thermoset polymers, the strain tends to a constant strain value after an extended period of time. In contrast, the strain for thermoplastic polymers continues to rise with no bound. Figure 5.7 also shows the creep recovery test, where strain is recovered upon removal of the load. For an ideal thermoset, all of the strain is recovered after a long period of time, while for an ideal thermoplastic, some residual strain remains [29]. However, McCrum [27] emphasizes that although all polymers used in engineering creep, the creep does not occur indefinitely and a complete recovery occurs after removal of the load.
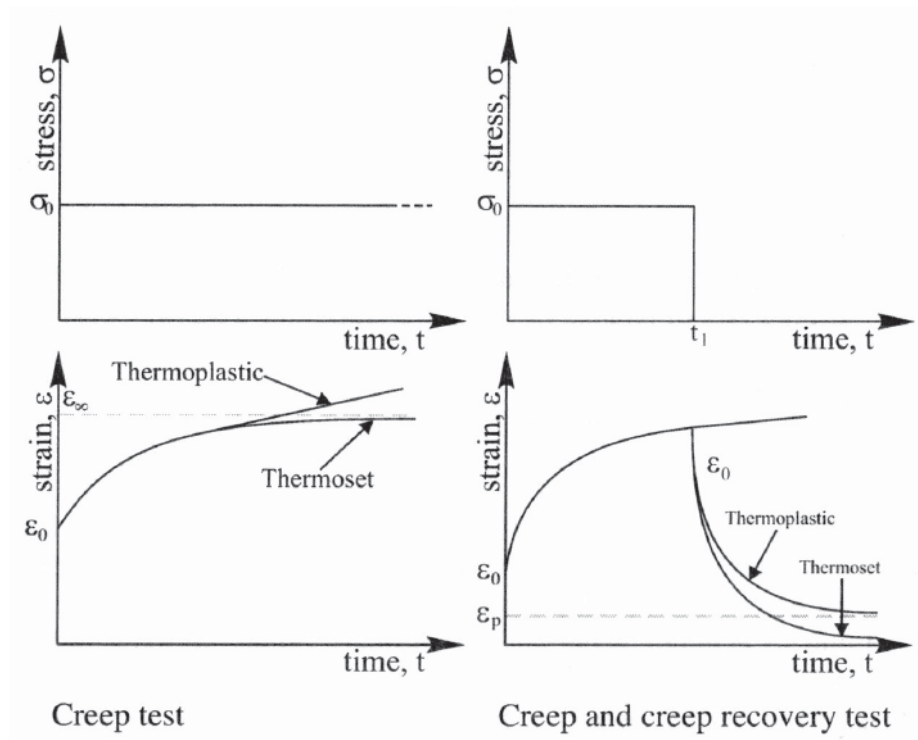
Figure 5.7.: Creep and creep relaxation test for an ideal thermoplastic and thermoset polymer [29].

Polymers undergo creep as a result of their long molecular chain structure. Under an applied load, the mobile sections of the chains undergo time dependent strain as the molecules rotate and unwind [27, 29]. Creep is limited to the segments of molecules between entanglements in thermoplastics and to the segments between cross-links for thermosets. Since spherulites have a similar effect to cross-links, creep is generally limited to the segments between spherulites [30]. Therefore, it is reasonable to believe that creep can be suppressed with increases in crystallinity. As creep occurs, back stresses build up, and lead to the strain being recovered if the load is removed. Creep ceases when the back stresses equal the magnitude of the applied stresses [27, 29]. Increases in temperature can highly expedite the rate of creep, therefore the max operating temperature a polymer could be subjected to in its use is an essential parameter used in material selection.

5.4.3 Stress Relaxation

Lastly, the stress relaxation test is used to observe time dependent stress in a polymer. In a stress relaxation test, shown in figure 5.8, a constant strain ϵ_0 is applied, and the time dependent stress $\sigma(t)$ required to maintain the strain monitored, defining a quantity known as the relaxation modulus,

$$E(t) = \frac{\sigma(t)}{\epsilon_0}. \tag{5.13}$$

In an ideal thermoplastic, the stress decays to zero after a long period of time, while in an ideal thermoset the stress tends to a non-zero value. Similar to creep, the mechanism behind stress relaxation is linked to the long molecular chain structure of polymers [29]. When the strain is applied, chain motion does not immediately occur. However, as time passes, chains rotate and unwind to accommodate the stress, decreasing the magnitude initially required to maintain the strain. Chain motion is again limited to the segments between entanglements, cross-links, and spherulites.
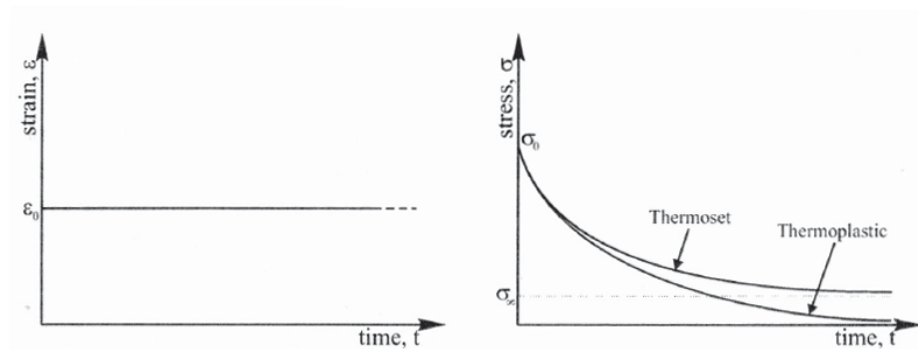
Figure 5.8.: Stress relaxation test for an ideal thermoplastic and thermoset polymer [29].

Stress relaxation tests can also be utilized to characterize the modulus dependence on temperature. An isochronous modulus versus temperature plot is often generated by taking the ratio of stress to strain at a specific time from a series of

isothermal stress relaxation tests. The 10 second modulus E(10s), 30 second modulus E(30s), etc. can be plotted against temperature to generate the plot in figure 5.2.

As explained in previous sections, residual stresses arise during an FDM process, with the magnitude of stresses becoming greater as FDM scales. During most large-scale printing processes as well as in our lab-scale system, the part remains at an elevated temperature due to the heated print bed, relatively low thermal conductivity of the polymer, and heat conducted into the rest of the part upon the addition of newly extruded layers. As a result, it is reasonable to believe that the residual stresses in the part could relax to some extent. Relaxation occurring throughout the printing process could lessen warpage and/or prevent layer delamination, and is therefore highly desirable. Certain geometries may not even be printable if stress buildup becomes too great, and for this reason predicting the degree to which stresses can relax during a printing process would be conducive. If it is known that stresses could not relax during the printing process, a post processing step involving the printed part being held at an elevated temperature in an oven may be required to relax out remaining stresses.

For printed parts that may be used in tooling applications, the presence of residual stresses could render the part unsuitable for the application. Residual stresses could lead to warping or creep at elevated temperatures, resulting in the tool not meeting the tight dimensional stability requirements for the application.

5.5 Summary

This chapter has introduced viscoelasticity, as well as methods used to characterize the time and temperature dependence of properties. Unlike metals and ceramics, the properties of a polymer can vary dramatically with moderate temperature increases. If a printed part is to serve as a composite tool, the performance at high temperatures must be well understood to ensure the tool will perform as needed. If a tool is used above the T_g of the material it is made from, deflections beyond tolerance limits could occur under the pressure of an autoclave if the modulus decays signifi-

cantly. Creep could occur under the high pressures of an autoclave, or as a result of residual stresses induced during the print process. Stress relaxation is a highly desirable viscoelastic effect. In fact, printing certain geometries may prove impossible if conditions conducive to relaxation are not utilized.

In the following chapter, the results of DMA, creep, and stress relaxation tests on 50 weight percent carbon fiber-reinforced PPS will be presented. To accurately predict the degree to which residual stresses within a printed part relax during and after the printing process, a nonisothermal stress relaxation model will be developed.

CHAPTER 6. VISCOELASTIC PROPERTIES OF REINFORCED PPS

In this chapter, the viscoelastic properties of 50 weight percent carbon fiber-reinforced PPS are characterized and discussed in the context of large-scale FDM and the target application of composite tooling. A TA Instruments Q800 DMA was used to conduct DMA, creep, and stress relaxation experiments on extruded filaments taken from a printed structure. Prior to any experiments, the material was tested to confirm linear viscoelasticity at low strains. Temperature sweep DMA experiments were then conducted to measure the T_g and identify the general behavior of the modulus with increasing temperature. A sample having max crystallinity as well as a quenched sample was tested, revealing the significant increase in high temperature properties arising from the crystallinity. A creep test was conducted at 180°C, the industry standard cure temperature for high performance composites, to determine if the reinforced PPS is suitable for high temperature composite tooling applications. Lastly, stress relaxation was measured across a wide range of temperatures, both to obtain isochronal relaxation modulus curves and to test the hypothesis that residual stresses introduced during printing could be relaxed. Generalized Maxwell models were fit to the relaxation experiments, and a linear interpolation method was used to generate relaxation modulus and normalized relaxation modulus surface plots over time and temperature. These surfaces can be used to predict nonisothermal stress relaxation that occurs as a printed part cools. In addition, the surfaces contain the required modulus versus time and temperature data that would be required to predict deformations that could arise from residual stresses.

6.1   Linear Viscoelastic Range

6.1.1   Definition

Prior to any viscoelastic property characterization, identifying the linear viscoelastic region, or LVR, is required. In the LVR, the rate at which viscoelastic responses occur are independent of the applied stress or strain. Therefore, to ensure the reproducibility of results, tests must be conducted within the LVR. Most polymers are linearly viscoelastic up to strains of 0.005 (0.5%) [27].

Multiple methods exist for determining the LVR, including strain-sweep DMA tests, creep tests, and stress relaxation tests. Prior to conducting the experiments presented in this chapter, a series of stress relaxation tests were carried out to confirm the reinforced PPS was linearly viscoelastic at low strains. A strain sweep test was then used to confirm the results and determine the limits of the LVR range. Below, the process for using stress relaxation tests to find the LVR is illustrated, which also helps to clearly define the phenomena of linear viscoelasticity.

As stated, in a stress relaxation test, a constant strain is applied, and the stress required to maintain that strain is recorded for some period of time. Suppose a strain ϵ_1 is applied to a sample, and the time dependent stress $\sigma_1(t)$ required to maintain ϵ_1 is measured, as illustrated in figure 6.1 (A). After some elapsed time, the strain is removed and the sample allowed to recover. Next, a larger strain ϵ_2 is applied, and the stress $\sigma_2(t)$ required to hold ϵ_2 constant is measured, as shown in figure 6.1 (B). Next, isochronal stress relaxation plots are generated from the data taken in the two tests. In an isochronal plot, the stress required to maintain the strain at a given time is plotted. Note that this data cannot simply be obtained from a standard stress-strain plot, but instead must be taken at time intervals from separate stress relaxation tests. Shown in figure 6.1 (C), $\sigma_1(t)$ and $\sigma_2(t)$ are plotted against ϵ_1 and ϵ_2 for t_a. The same is then repeated for t_b. If the isochronals are linear, the polymer is in the LVR, that is the degree of stress relaxation is independent of the applied strain [27]. In this region,

$$\frac{\sigma_1(t)}{\epsilon_1} = \frac{\sigma_2(t)}{\epsilon_2}$$

and therefore the relaxation modulus $E(t)$ can be defined by

$$E(t) = \frac{\sigma(t)}{\epsilon} \tag{6.1}$$

using any arbitrary strain value in the LVR. At strains where isochronals become non-linear, stress values can not be extrapolated because stress relaxation is occurring to a greater extent. In this region, the material is said to be non-linearly viscoelastic, and individual relaxation tests would be required to find the time dependent stress $\sigma(t)$.

The relaxation modulus $E(t)$ values found across decades of time can be used to generate the plot shown in figure 6.1 (D). E_U and E_R represent the unrelaxed and relaxed $E(t)$ respectively, and show little time dependence. The sigmoid-shape in between will not appear entirely if relaxation is not measured over enough decades of time. In the following section, the results from a series of stress relaxation tests used to test for linear viscoelasticity as well as a strain sweep test to identify the limits of the LVR are presented.
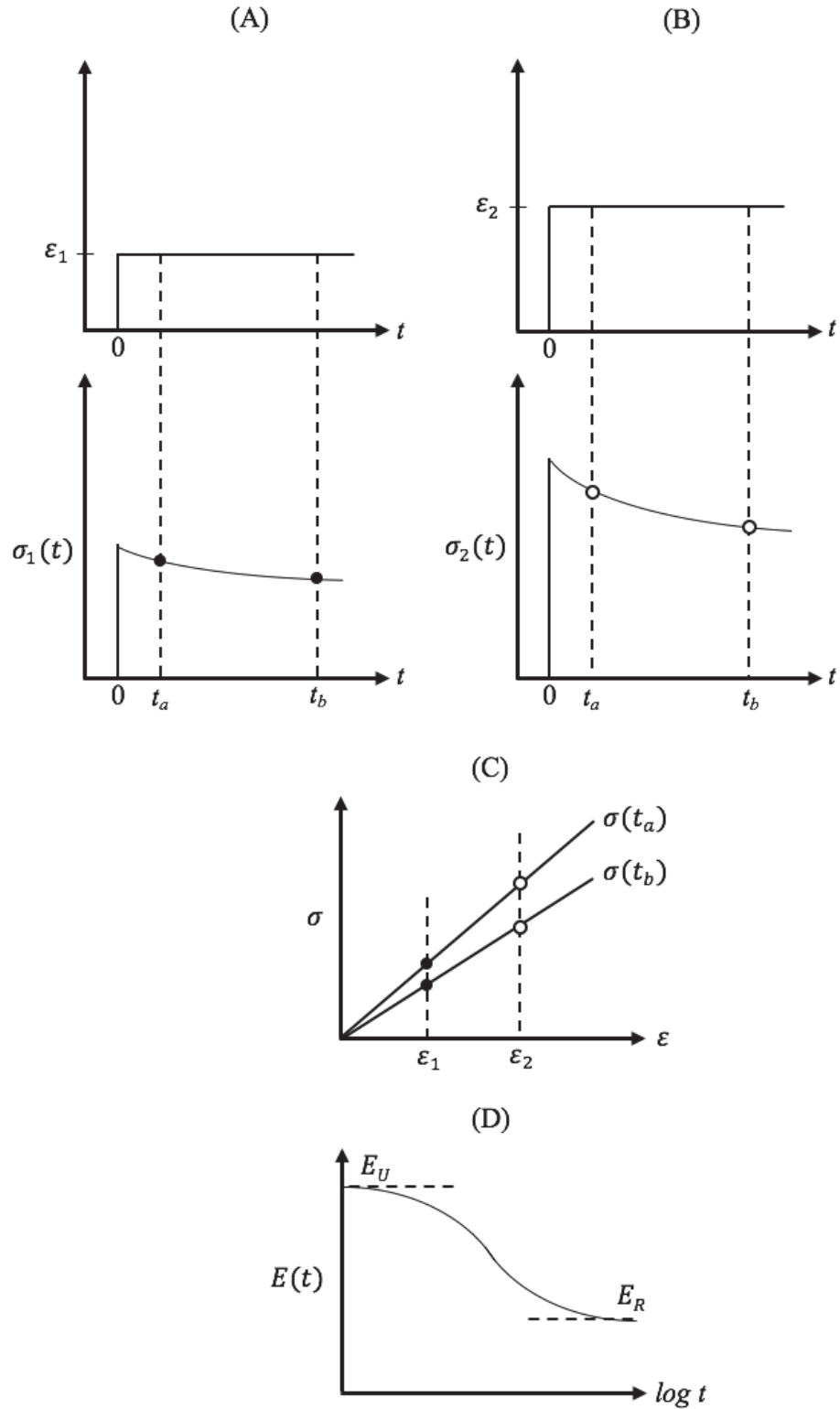
Figure 6.1.: Linear Viscoelasticity: (A) & (B) stress relaxation plots; (C) linear isochronal plots identifying the LVR; (D) dependence of $E(t)$ on time [27].

6.1.2 Identification of the LVR for Carbon Fiber-Reinforced PPS

To confirm the 50 weight percent carbon-fiber reinforced PPS was linearly vis-coelastic at low strains, relaxation tests were conducted at 50°C for strains ranging from 0.025% - 0.125%, expected to be within the LVR. The test samples were printed filaments prepared using the procedure outlined in section 6.4.1.1. The resulting isochronals are shown in figure 6.2. Due to the linearity, the material is within the LVR at these strains. Therefore, results from any viscoelastic tests conducted within this range will be reproducible at other arbitrary values of strain within the LVR.
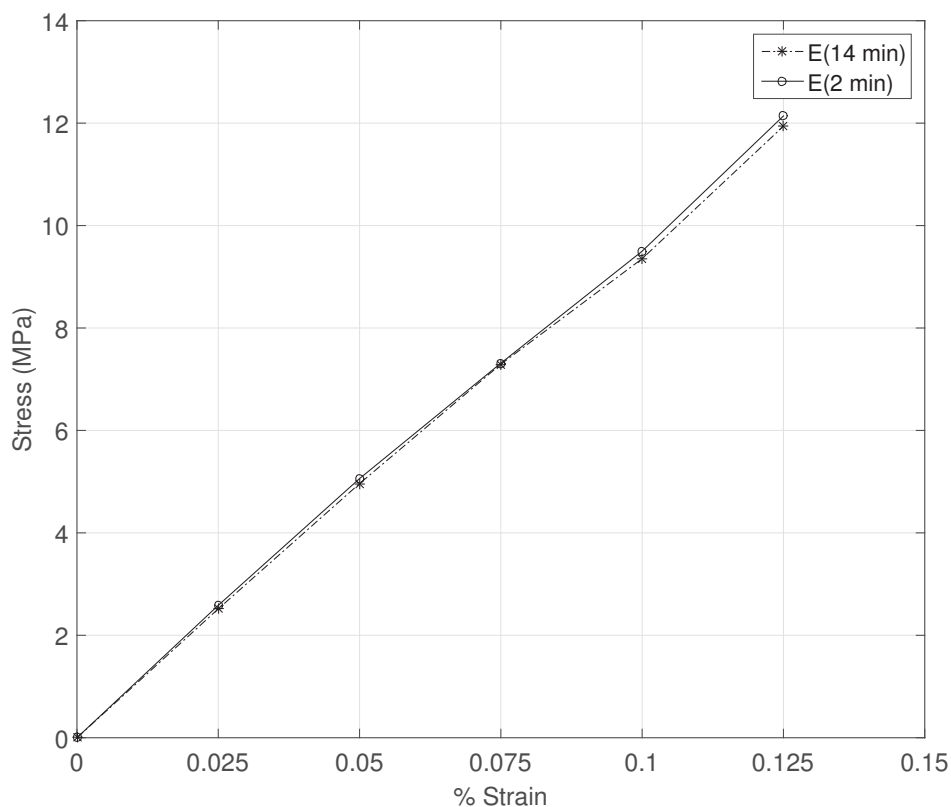
Figure 6.2.: Isochronals illustrating linear viscoelasticity.

A dynamic strain sweep test was then conducted to find the limits of the LVR. Displacements ranging from 0 to 200 µm were applied at a frequency of 1 Hz and a

temperature of 50°C. Figure 6.3 shows the normalized storage modulus versus strain percent. The LVR is said to extend to the strain percent where the storage modulus has lost 5% of its initial value [39, 40]. Therefore, the LVR extends to approximately .175 strain percent.
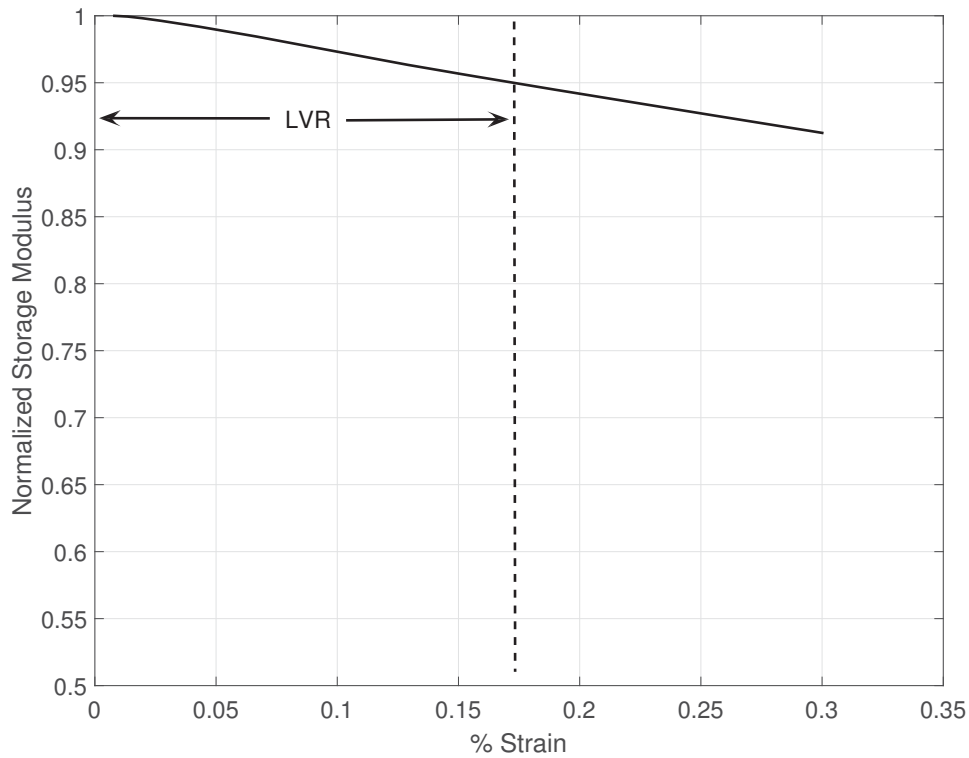
Figure 6.3.: Strain sweep test to identify the LVR.

6.2 Dynamic Mechanical Analysis of Carbon Fiber-Reinforced PPS

As stated in earlier chapters, the properties of polymers show a strong dependence on temperature. Section 5.4.1 introduced DMA as a method for characterizing modulus versus temperature behavior, as well as separating the elastic and viscous components. In addition, DMA is the most sensitive test for identifying the glass transition temperature [38]. Therefore, DMA experiments are a useful tool for evaluating the reinforced PPS for high temperature tooling applications.

6.2.1 Sample Preparation

Extruded filament samples approximately 60 mm long x 3.9 mm wide x 1.6 mm thick, shown in figure 6.4, were prepared for the DMA experiments. The samples were taken from a grid structure that was printed onto a 240°C heated table surface using the standard printing conditions. Since the layer height is smaller than the extrudate diameter, filaments were slightly pressed against the table, resulting in a cross section most similar to a rectangle.

Figure 6.4.: Extruded bead of carbon fiber-reinforced PPS used in viscoelastic tests.

Even when cut into 60 mm samples, the extruded filaments had slight width and thickness variability, mainly due to the unevenness of the table surface the grids were printed on. Therefore, 16 measurements were used to determine the dimensions of each sample to ensure representative measurements were obtained. Samples with large dimensional variability, especially in thickness measurements since tests were conducted in bending modes, were not used.

To evaluate the effect of crystallinity on the properties of the material, both a sample having the max crystallinity as well as a quenched sample were tested. The first sample was annealed at 150°C for one hour to ensure the max crystallinity was developed. A DSC thermograph of this sample is shown in figure A.4 (a) in the appendix. The crystallinity mass fraction X_{mc} was found to be 0.42 (42%) of the polymer (21% of the composite), similar to the results of the sample from a printed part tested in section 3.3.1. To prepare the quenched sample, a filament was first placed in an oven at 300°C for several minutes to melt, then rapidly removed and quenched in water. The DSC thermograph of this sample is shown in A.4 (b) in

the appendix. Clearly, an exothermic peak existed in the thermograph in the cold crystallization range. However, comparing the the heat of crystallization H_c with the heat of melting H_m reveals that crystallinity existed in the sample prior to testing, even with a rapid quench. The crystallinity mass fraction X_{mc} was found to be 0.12 (12%) of the polymer (6% of the composite). Therefore, approximately one quarter of the max crystallinity can develop when quenching from the melt, again illustrating the rapid crystallization kinetics in PPS. Of course a printed sample would never have a crystallinity fraction this low, however comparing the two extremes in DMA tests provides great insight into the effects of crystallinity.

6.2.2   Experimental Procedure

A temperature sweep DMA test was performed on the samples using a TA Instruments Q800 DMA. Samples were tested using the 35 mm span double-cantilever clamp shown in figure 6.5. An oscillating displacement of 25 µm was applied at a frequency of 1 Hz. The temperature was ramped at 3°C/min from 40°C to 300°C.
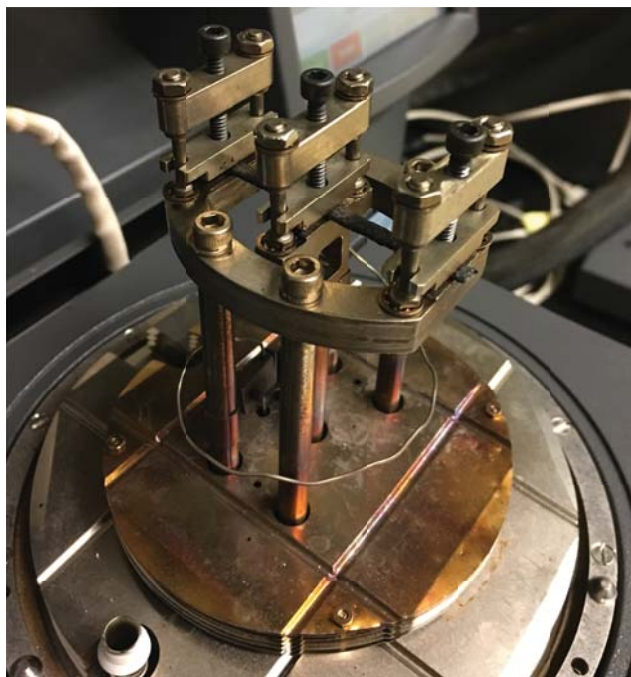
Figure 6.5.:   Sample loaded in the 35 mm span double cantilever clamp.

6.2.3 Experimental Results

Figure 6.6 shows the results of the DMA experiments.
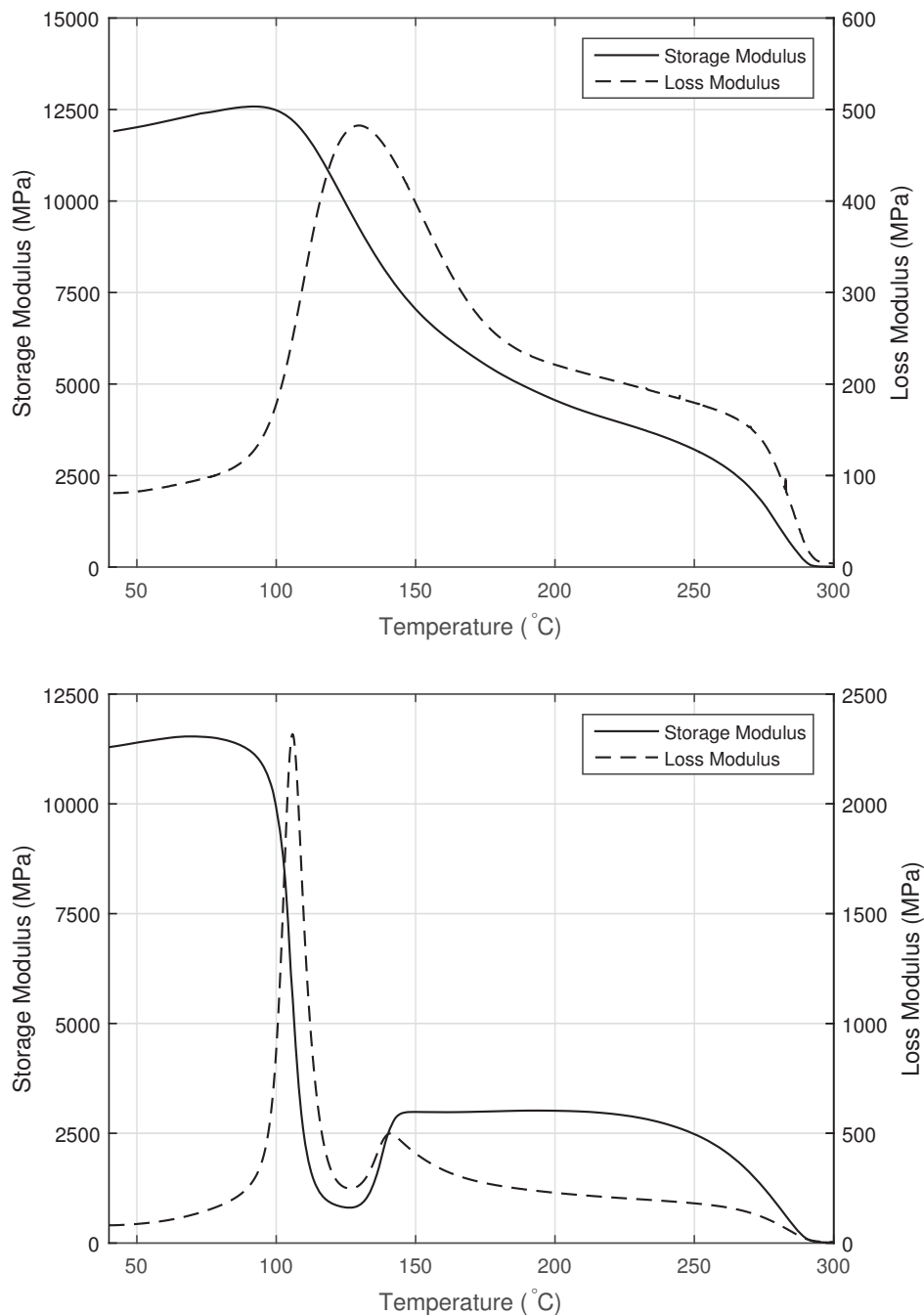
Figure 6.6.: DMA tests on carbon fiber-reinforced PPS printed filaments having 0.42 (top) and 0.12 (bottom) mass fraction crystallinity.

The greater crystallinity in the annealed sample significantly increased the properties of the reinforced PPS. If the T_g is taken to be the onset of the decay in the storage modulus, the greater crystallinity increased the T_g by approximately 10°C. More striking is the significant increase in properties above the T_g. Since the T_g is associated with the amorphous regions of the polymer, the change in properties observed at the T_g is strongly influenced by the degree of crystallinity. The modulus of the sample having max crystallinity does not experience the same dramatic drop above T_g as the sample having only 0.12 mass fraction crystallinity. As outlined in section 5.2, spherulites increase the modulus above T_g through at least two mechanisms [30]. In the first, the spherulites tie sections of molecules together, similar to cross-links. In the second, the spherulites with their high stiffness act as rigid fillers in the rubbery amorphous regions. The effects of spherulites last until T_m is approached, where irreversible flow behavior takes over.

The DMA test on the quenched sample captured the cold crystallization that occurred within the polymer at 125°C. Crystallinity quickly developed, resulting in a very stable rubbery plateau remaining until T_m was approached. An interesting observation is the lower magnitude of the plateau compared to the annealed sample. This could be attributed to the mass fraction of crystallinity not reaching the max level during cold crystallization, which was observed in cold crystallization experiments by Kenny et al. [22]. Since regions in printed parts that cool rapidly may be further crystallized through cold crystallization, this result could very well be observed. This observation is significant and illustrates that high temperature properties such as the heat distortion temperature (HDT) may vary within a printed part. This difference cannot simply be eliminated through further annealing, illustrated by the very flat modulus as the sample remained at elevated temperatures. For example, at 140°C, the storage modulus in the cold crystallized sample is 60% lower than that of the annealed sample. However, this is the extreme case, and the relatively rapid cooling rates experienced within certain regions of a part during printing result in a higher

degree of crystallinity than the quenched sample, meaning these regions begin cold crystallization with a greater initial crystallinity mass fraction.

Another interesting observation is the decay that continued through the rubber plateau region in the annealed sample. However, this is typically observed in crystalline polymers and attributed to small and/or imperfect spherulites melting before T_m, reducing the cross-link and rigid filler mechanisms [31].

Unfortunately, neat PPS could not be obtained for testing and comparison to the reinforced grade. The DMA plot of a neat PPS sample would be expected to be lower and shifted to the left of the annealed sample. Fibers both increase the modulus and shift the T_g to a higher value since the T_g of neat PPS is 85°C [22]. The slope in the transition region for the neat PPS may vary due to the neat polymer developing greater crystallinity than the reinforced grades [22].

6.3 Creep Behavior of Carbon Fiber-Reinforced PPS

6.3.1 Sample Preparation

For the creep experiment, a sample was prepared using the process outlined in section 6.2.1. Prior to testing, the sample was annealed at 150°C for one hour to ensure the max crystallinity was developed. This step was taken for two reasons. First, it ensured additional crystallinity did not develop during the experiment. In addition, printed parts that would serve as tooling should have the max crystallinity to achieve the highest performance. Therefore, creep experiments should be conducted on samples having the max crystallinity in order to accurately represent creep that could occur in use.

6.3.2 Experimental Procedure

A creep test was performed on the samples using a TA Instruments Q800 DMA. A sample was tested in the 50 mm span 3 point bending clamp shown in figure 6.7. During the test, the sample was heated to 180°C, held for 5 minutes, and a constant

stress of 10 MPa was applied. A test temperature of 180°C was chosen since it is the industry standard cure temperature for high performance composites. The time dependent strain was monitored for 280 minutes. The creep compliance D(t) was then calculated and plotted.

Figure 6.7.: Sample loaded in the 50 mm span 3 point bending clamp.

6.3.3 Experimental Results

Figure 6.8 shows the resulting creep compliance plot when tested at 180°C. The plot indicates that creep occurs rapidly in the first 10 minutes, then gradually slows. The creep compliance continued to rise throughout the 280 minutes. Although the carbon fiber-reinforced PPS retains mechanical properties at 180°C, the material creeps at this temperature rather significantly. It is important to note that like other properties, the creep compliance is highly anisotropic, and is likely significantly greater in the transverse direction. As a result, dimensional stability cannot be guaranteed under the high pressures in an autoclave at this temperature. If attempted, only the tool surface should be vacuum bagged, rather than the entire tool being envelope bagged. This allows pressure to surround the tool, rather than requiring the

tool surface to support the high pressure. However, even when taking this measure, the tool could still deform if the pressure forces material into the inter-bead voids between layers. Further creep experiments should be conducted at lower temperatures to test the feasibility of tooling applications.
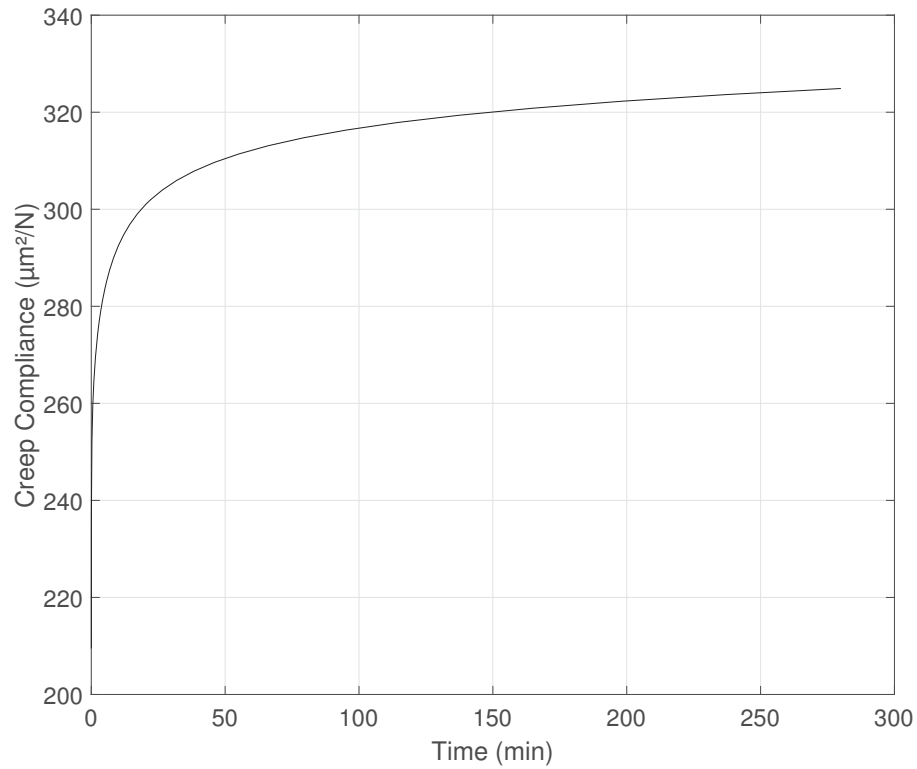
Figure 6.8.: Creep compliance at 180°C under a constant stress of 10 MPa.

6.4   Characterization and Modeling of Stress Relaxation in Carbon Fiber-Reinforced PPS

In this section, the experimental procedure and results from isothermal stress relaxation tests are presented. The results are then discussed in the context of relaxation in printed parts. Next, simple models used to represent stress relaxation were presented, and the need for more complex models to accurately describe real materials was discussed. Generalized Maxwell models were then fit to each of the relaxation

experiments, and a linear interpolation method was used to generate relaxation modulus and normalized relaxation modulus surfaces. These surfaces describe the modulus dependence on time and temperature, and could be used to predict deformations that could arise from residual stresses, as well as to quantify the amount of stress relaxation that occurs when a printed part cools.

6.4.1   Measuring Stress Relaxation

Prior to modeling the nonisothermal stress relaxation behavior of the 50 weight percent carbon fiber-reinforced PPS used in printing, isothermal relaxation experiments were carried out to measure the real response of the material. A series of stress relaxation experiments were conducted using a TA Instruments Q800 DMA in stress relaxation mode.

6.4.1.1. Sample Preparation

For the stress relaxation experiments, samples were prepared using the process outlined in section 6.2.1. Prior to testing, all samples were annealed at 150°C for one hour to ensure the max crystallinity was developed in each of the samples. This step was taken for two reasons. First, if the samples did not have the max crystallinity prior to testing, additional crystallinity would have developed during the relaxation experiments conducted at temperatures above the cold crystallization temperature. Second, since the max crystallinity is expected to exist in most of the volume of a printed part, the relaxation experiments should be conducted on samples having the max crystallinity to accurately represent the relaxation that would occur in a printed part. To eliminate variability in sample processing history, all samples were printed during the same session and annealed in the same batch.

6.4.1.2. Experimental Procedure

Samples were tested in the 50 mm span 3 point bending clamp shown in figure 6.7. This clamp was chosen not only because it is recommended for stiff samples, but

also due to bending most closely mimicking the actual loading mechanism introduced by residual stresses during printing.

Relaxation tests were conducted at temperatures ranging from 50°C to 300°C, however the 300°C test failed due to the sample yielding immediately upon application of the load. Below 50°C, negligible relaxation (less than 1%) occurs. The results from the DMA test on the sample having max crystallinity were used to identify the temperatures ranges where the greatest changes in properties occurred (i.e. glass transition and rubbery flow regions) to ensure relaxation tests were conducted at smaller temperature intervals in these regions. During each experiment, samples were ramped to the test temperature, held for 5 minutes, and displaced to a constant strain of 0.05%. The stress required to maintain the strain was then monitored for 30 minutes. The relaxation modulus E(t) was calculated from the stress data and plotted for each sample. Original runs were conducted for 90 minutes, however since nearly all relaxation occurred in the first 30 minutes, a test time of 30 minutes chosen.

6.4.1.3. Experimental Results

Figure 6.9 shows the models for seven of the relaxation experiments, with both the actual and normalized modulus models shown. The models used to fit the experimental data will be explained in detail in sections and . In each run, the stress and therefore relaxation modulus decayed exponentially from the initial value. As the the temperature increased, the initial modulus for each test decreased following the behavior in figure 6.6 (a). The rate and degree of relaxation also increased with increasing temperatures, attributed to the greater chain mobility afforded. The relaxation modulus for each sample decayed to a relaxed non-zero state. This is a characteristic of crystalline and cross-linked polymers. As discussed in sections 5.2 and 6.2.3, spherulites, like cross-links, tie segments of molecules together, limiting the amount of chain conformation and elongation that can occur to accommodate the load. The presence of fibers could also hinder chain mobility and limit the degree of relaxation.

At 50°C, little stress relaxation can occur, with the relaxation modulus decaying only slightly greater than 1%. At 290°C, relaxation occurs to a much greater extent, with the relaxation modulus decaying greater than 60%. During a printing process, previous layers will likely decay to temperatures between 90-220°C. The relaxed state of tests conducted at these temperatures was only 10-25% below the initial values. This is a significant finding and indicates that residual stresses introduced during printing processes will not relax during the printing process. This learning explains why it is not uncommon for parts exceeding 4 inches in height to warp upward during the printing process and dislodge from the table. Since the stresses decay to a relaxed value, a post-printing annealing process conducted at a temperature close to T_m may still leave residual stresses in the part. Therefore, further measures beyond heating the table surface may be required to keep the part at an elevated temperature during printing. This would not only maximize the relaxation that can occur, but more importantly lead to more uniform cooling and lessen the development of residual stresses that may not be able to be removed.

The presence of residual stresses in a composite tool could render the tool unsuitable for applications requiring tight dimensional stability. When raised to the temperatures between 100-180°C, typical in the manufacturing of composite components, residual stresses could cause the tool to warp.

Certainly a limitation of this data is that it only represents the properties in the print direction since transverse samples would be quite difficult to prepare and test. The modulus values in the transverse directions are significantly lower, but the expected relaxation behavior is not immediately obvious. More would need to be understood about the presence and orientation of the amorphous segments between the spherulites nucleated along the highly collimated fibers. However, it is still expected that the relaxation modulus would decay to a non-zero state due to the presence of spherulites.
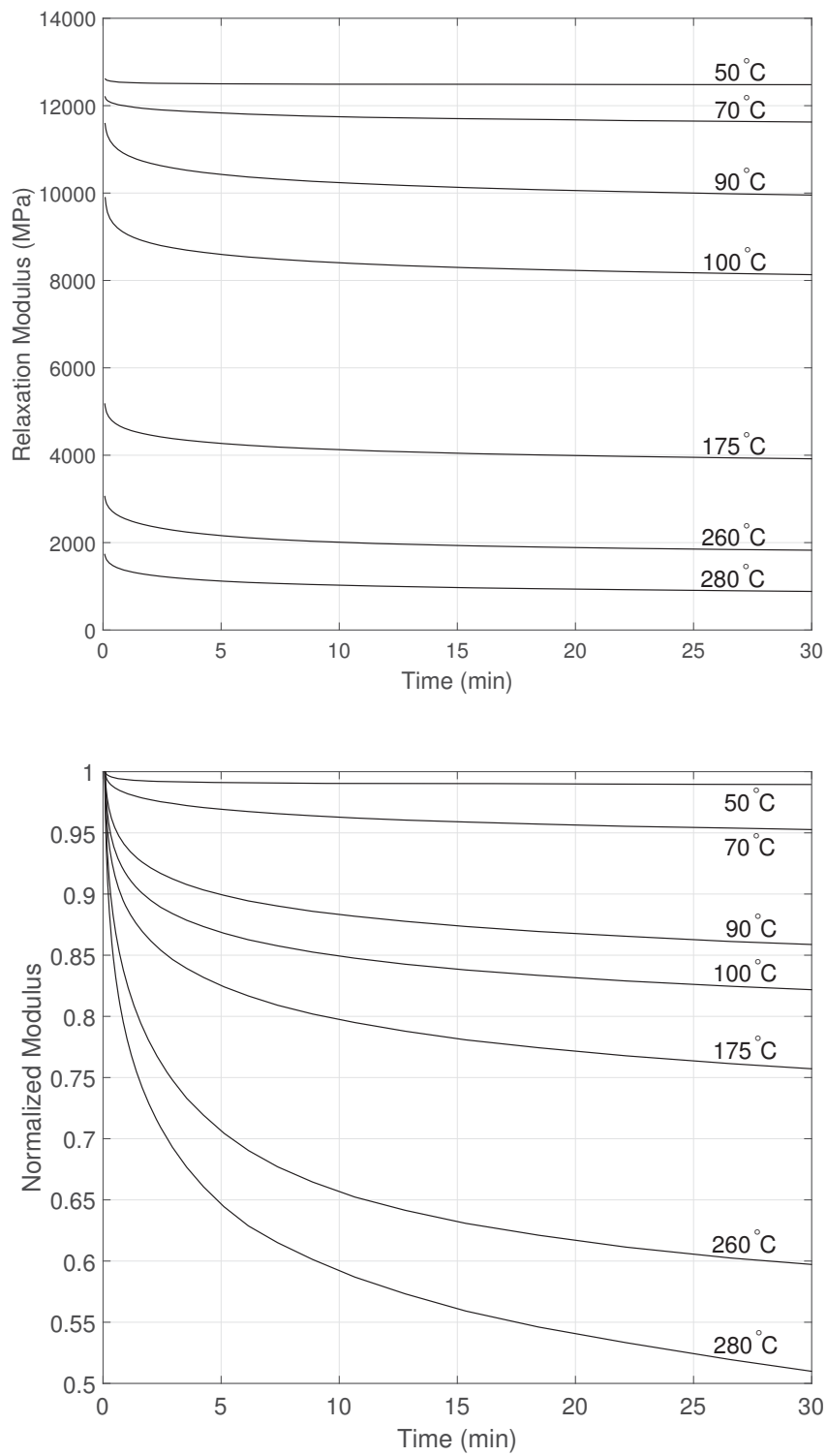
Figure 6.9.: Relaxation modulus (top) and normalized relaxation modulus (bottom) during relaxation experiments between 50°C to 280°C.

An isochronal plot of the 6 second relaxation modulus is shown in figure 6.10. The 6 second relaxation modulus was chosen since it was the earliest value the Q800 DMA accurately measured at the low temperatures. This plot shows the variation of the modulus in the print direction with temperature, and is essential when evaluating the material for high temperature applications, among other things. Although the storage modulus versus temperature plot follows a similar behavior, it is important to note that the plots are not one in the same. A sum of sines model was fit to both the isochronal relaxation modulus and normalized relaxation modulus data. The models and coefficients are shown in section A.4 in the appendix.

An important performance metric to consider when evaluating the use of reinforced polymers for high temperature applications is the heat distortion temperature (HDT), an ASTM standard which specifies the temperature at which a material will deflect under a load. Reinforcing PPS with carbon fiber is expected to significantly increase the HDT over that of the neat polymer. Although the plot in figure 6.10 illustrates that the reinforced PPS would have a high HDT, this may not be the case in the transverse direction. As stated in section 5.2, the increase in HDT observed in fiber-reinforced crystalline polymers is a result of the increased modulus [31]. Therefore, the HDT in the transverse direction is most likely far lower in the transverse direction since the fibers become highly collimated in the print direction during FDM. This fact again illustrates the need for a broader fiber orientation distribution in extruded beads.
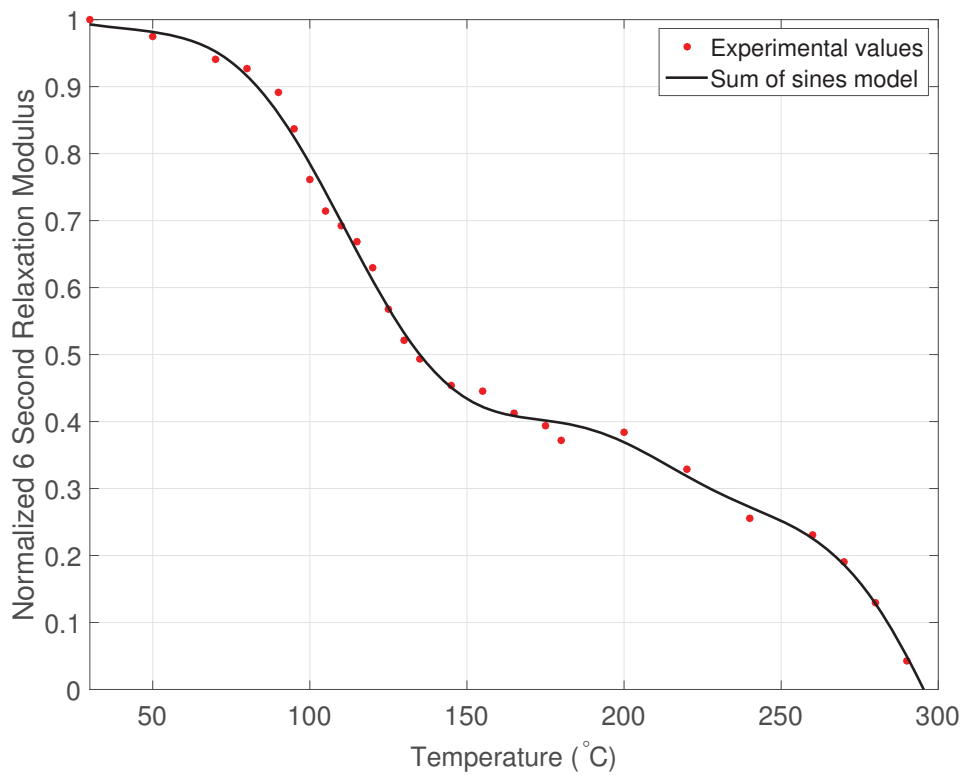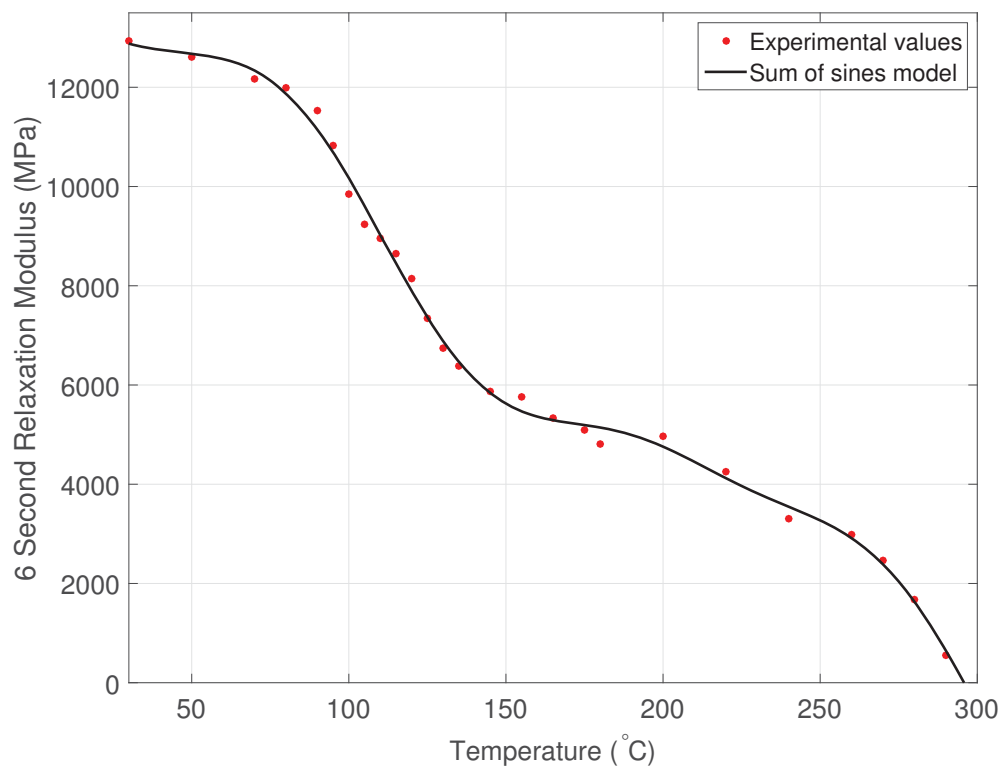
Figure 6.10.:   6 second relaxation modulus versus temperature.

6.4.2   Modeling Stress Relaxation

6.4.2.1. Maxwell Model

Models incorporating massless Hookean springs and Newtonian dashpots are often utilized to represent viscoelastic behavior [26]. A Newtonian dashpot is a fluid filled cylinder containing a piston. The rate of the pistons motion is determined by both the applied external load and the viscosity of the fluid within the cylinder. These spring and dashpot models are used to develop differential equations that represent viscoelastic behavior.
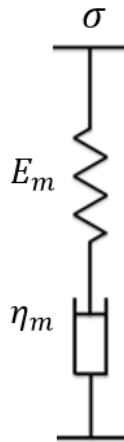
Figure 6.11.: The Maxwell model, consisting of a spring and dashpot in series.

The Maxwell model, shown in figure 6.11, is a simple unit consisting of a spring and dashpot in series. The spring represents the elastic contribution, with the stress-strain relationship given by

$$\sigma_1 = E_m \epsilon_1 \tag{6.2}$$

where σ_1 and ϵ_1 are the stress and strain in the spring, and E_m is the spring stiffness [26]. The dashpot gives the the viscoelastic contribution, with the stress-strain relationship given by

$$\sigma_2 = \eta_m \frac{d\epsilon_2}{dt} \tag{6.3}$$

where σ_2 and ϵ_2 are the stress and strain in the dashpot, and η_m is the viscosity of the fluid [26]. Since the elements are in series, the total stress in the Maxwell unit is equal to the stress in both the spring and dashpot, giving $\sigma = \sigma_1 = \sigma_2$. The total strain in the unit includes contributions from both the spring and the dashpot, giving $\epsilon = \epsilon_1 + \epsilon_2$. To determine a relationship between the total stress and strain in the unit, the derivative of equation 6.2 can be taken, giving

$$\frac{d\sigma}{dt} = E_m \frac{d\epsilon_1}{dt} \tag{6.4}$$

and combined with equation 6.3 to give

$$\frac{d\epsilon}{dt} = \frac{1}{E_m}\frac{d\sigma}{dt} + \frac{\sigma}{\eta_m} \tag{6.5}$$

Since a constant displacement is applied during a relaxation test, $\dfrac{d\epsilon}{dt} = 0$, therefore rearranging equation 6.5 gives

$$\frac{d\sigma}{\sigma} = -\frac{E_m}{\eta_m}dt \tag{6.6}$$

When $t = 0$, the stress is equal to the initial stress ϵE_m, and integrating gives

$$\sigma(t) = \epsilon \; E_m \; exp\left(\frac{-E_m t}{\eta_m}\right) \tag{6.7}$$

A constant τ is often inserted into this equation to give

$$\sigma(t) = \epsilon \; E_m \; exp\left(\frac{-t}{\tau}\right) \quad \text{where} \quad \tau = \frac{\eta_m}{E_m} \tag{6.8}$$

and is known as the relaxation time. Dividing both by sides by ϵ gives the relaxation modulus $E(t)$,

$$E(t) = E_m \; exp\left(\frac{-t}{\tau}\right) \tag{6.9}$$

which follows the same behavior as $\sigma(t)$. Similar to the stress in an ideal thermoplastic during a relaxation test, this equation decays to zero after some period of time.

Although simple models like Maxwell's are useful for describing general stress, strain, and time dependent responses in viscoelastic materials, as well as for developing simple differential equations to model the response, they often do not fully capture the behavior of linearly viscoelastic polymers [31]. In the simple models, the timescales where most changes occur in the material are collapsed, with most changes occurring over only one decade of time [31]. Real polymers typically undergo the same changes, however over a few or many decades of time. For this reason, more complex models have been developed that more accurately describe the behavior of real polymers.

6.4.2.2. Generalized Maxwell Model

Better representations of stress relaxation in real polymers can be obtained by using multi-element models, where additional units are added in series or in parallel to simulate relaxation events. The generalized Maxwell model, shown in figure 6.12 consists of multiple Maxwell units and a spring in parallel. The Maxwell units can represent a spectrum of relaxation times, and the spring limits the stress decay to the relaxed state.
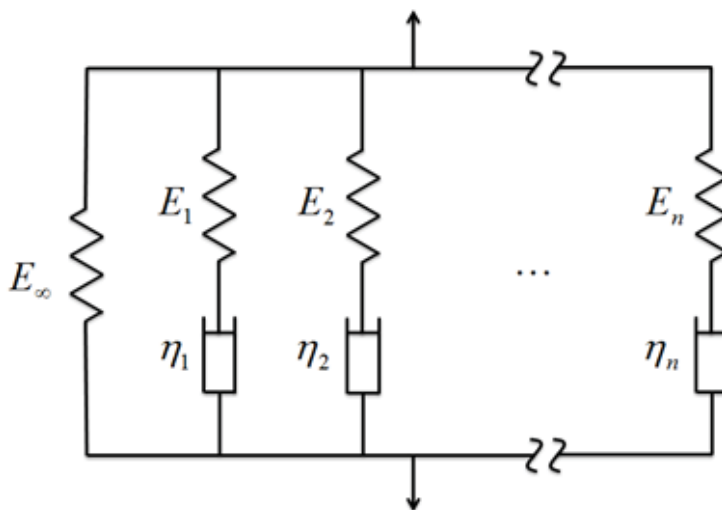
Figure 6.12.: The generalized Maxwell model consists of a multiple Maxwell units and a spring in parallel.

Stress relaxation in the generalized Maxwell model can be represented by

$$\sigma(t) = \epsilon \left(E_\infty + \sum_{i=1}^{n} E_i \ exp \left(\frac{-E_i t}{\eta_i} \right) \right) \tag{6.10}$$

where E_∞ defines the final relaxed state and the summation gives the contribution from n Maxwell units having spring stiffness E_i and fluid viscosity η_i. Plotting the above equation gives an exponential decay curve similar to the Maxwell model, however the relaxation is spread across a broader timescale. At $t=0$, ϵ is equal to the constant elongation, and $\sigma = \epsilon \ (E_\infty + E_1 + E_2 + ... \ E_n)$. As $t \rightarrow \infty$, $\sigma \rightarrow \epsilon E_\infty$.

6.4.3   Modeling Stress Relaxation in Carbon Fiber-Reinforced PPS

6.4.3.1. Developing Stress Relaxation Model

A generalized Maxwell model consisting of four Maxwell units in parallel with a spring was found to near perfectly model isothermal relaxation in reinforced PPS. MATLAB was utilized to determine the coefficients that fit the generalized Maxwell model, shown below, to the experimental data.

$$E(t) = E_\infty + E_1 \ exp \left(\frac{-t}{\tau_1} \right) + E_2 \ exp \left(\frac{-t}{\tau_2} \right) + E_3 \ exp \left(\frac{-t}{\tau_3} \right) + E_4 \ exp \left(\frac{-t}{\tau_4} \right) \tag{6.11}$$

where

$$\tau_i = \frac{\eta_i}{E_i}$$

The resulting plots, coefficients, and goodness of fit are shown in section A.3 in the appendix. The isothermal models were then plotted in 3D space, with time plotted along the x axis, temperature along the y axis, and relaxation modulus along the z axis. Linear interpolation was then used to approximate the relaxation modulus between the isothermal models, and a surface was plotted. A code was then written to allow the nonisothermal relaxation modulus curve to be plotted if the time and

temperature history are inputted. The same was process was completed to generate a surface plot for the normalized relaxation modulus. Figure 6.13 shows the resulting surface plots.

The code can be used to model nonisothermal stress relaxation that occurs in a part during the printing process. The time and temperature history can be used to determine the relaxation modulus curve, or the degree of stress relaxation if each modulus value is divided by the t=0 value for the corresponding temperature, as shown in the normalized surface plot. If the nonisothermal normalized relaxation modulus curve begins to increase, it is assumed that relaxation will cease, and the remainder of the curve can be neglected. This will occur when the material has relaxed at higher temperatures to an extent not possible at lower temperatures.
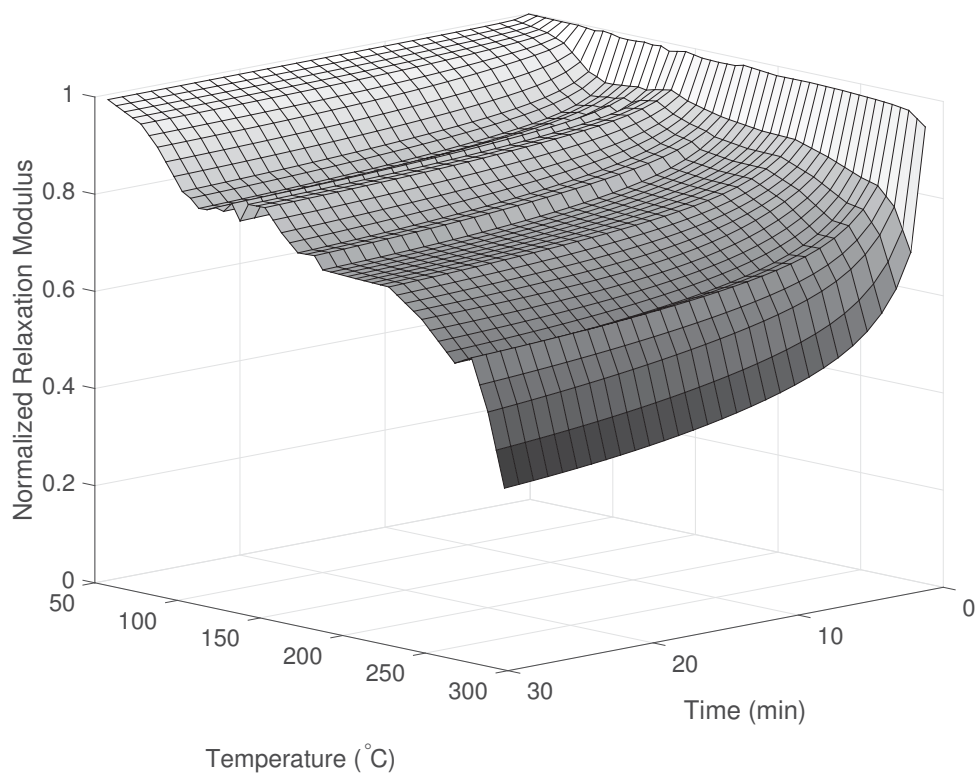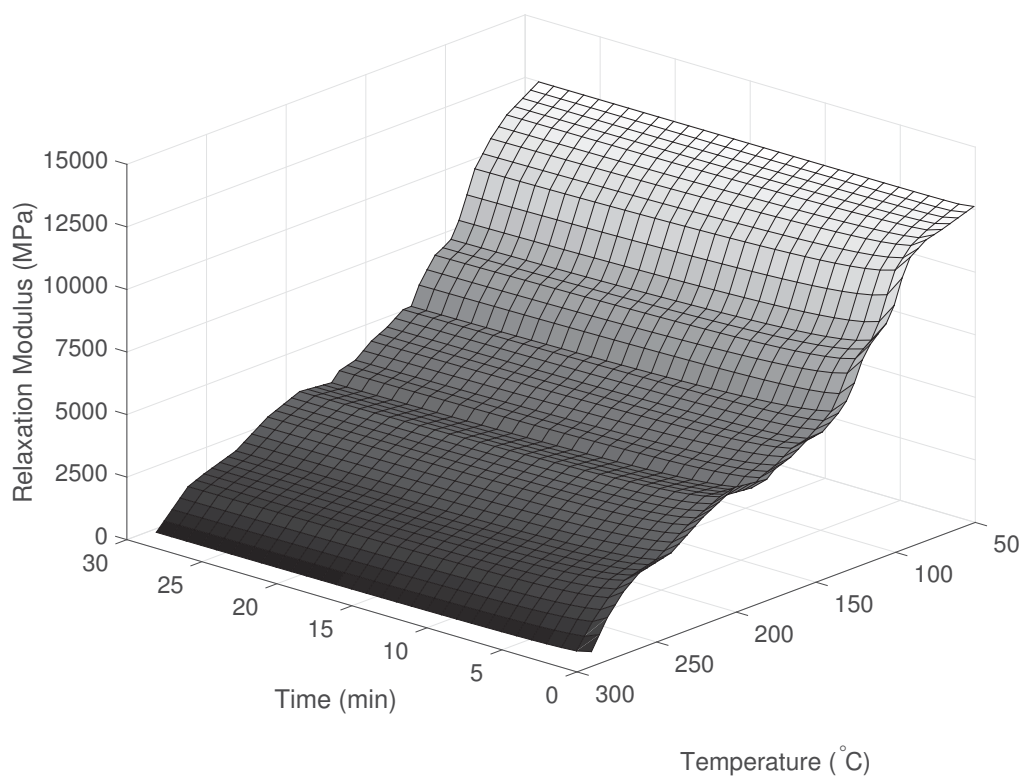
Figure 6.13.:   Relaxation modulus surface plots.

6.4.3.2. Validating Stress Relaxation Model

Relaxation samples were prepared using the process described in section 6.4.1.1. To conduct nonisothermal relaxation experiments, the Q800 DMA was operated in isostrain mode, where a constant strain is applied and the temperature varied. Unfortunately, the equipment does not have the capability to begin tests at high temperatures and ramp down, so tests were started at approximately 50°C and ramped to over 140°C.

Figure 6.14 shows the relaxation modulus plot for a nonisothermal relaxation test started at 45°C and ramped at approximately 3.5°C/min to 145°C. The time and temperature history was then inputted to the model to determine the relaxation modulus curve predicted by the surfaces, shown in figures 6.14 and 6.15. Since the model does not extend below 50°C, it was approximated that the early temperature values between 45°C and 50°C were equal to 50°C, a valid approximation due to the minuscule relaxation that occurs at these low temperatures. The measured values are in good agreement with the model, with the initial and final values lining up well and the general behavior being the same. It is important to note that the decay in modulus for these curves is not only due to relaxation but also due to the inherent decrease in modulus that results at higher temperatures. For this reason, it is necessary to normalize each relaxation modulus value with respect to the t=0 value at the corresponding temperature to quantify the actual stress relaxation that is occurring, as shown in the bottom right plot in figure 6.15. The plot indicates that approximately 20% of the stress was relaxed during the experiment.
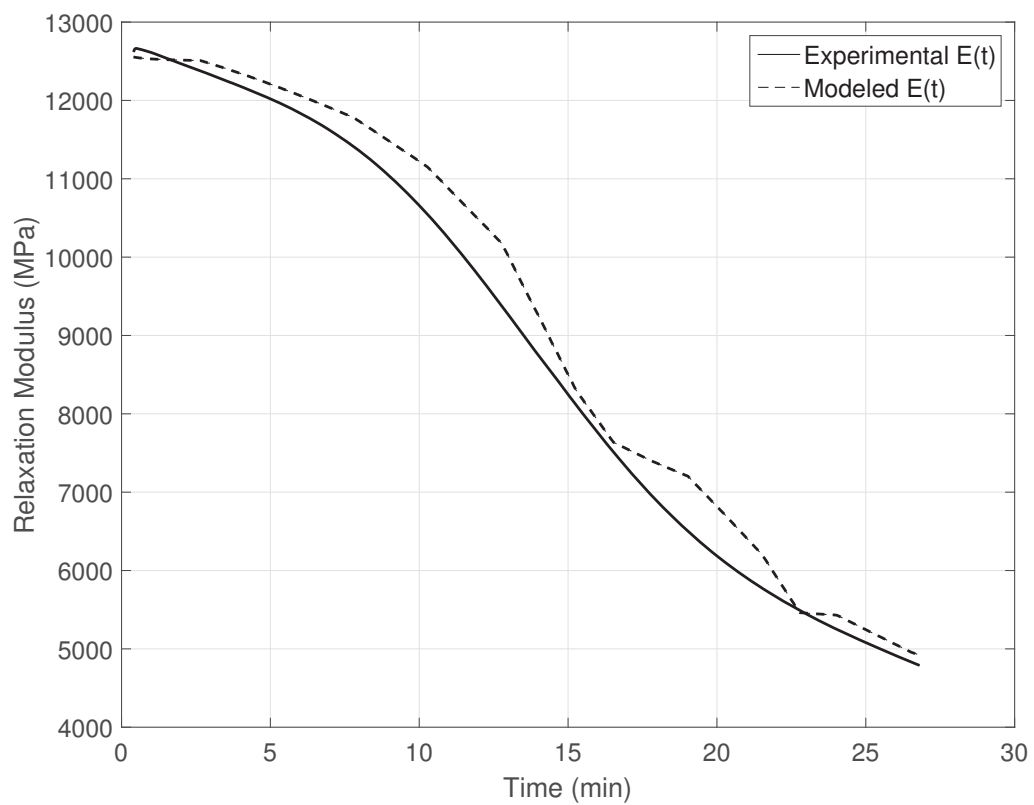
Figure 6.14.:   Experimental and modeled nonisothermal relaxation modulus curves.
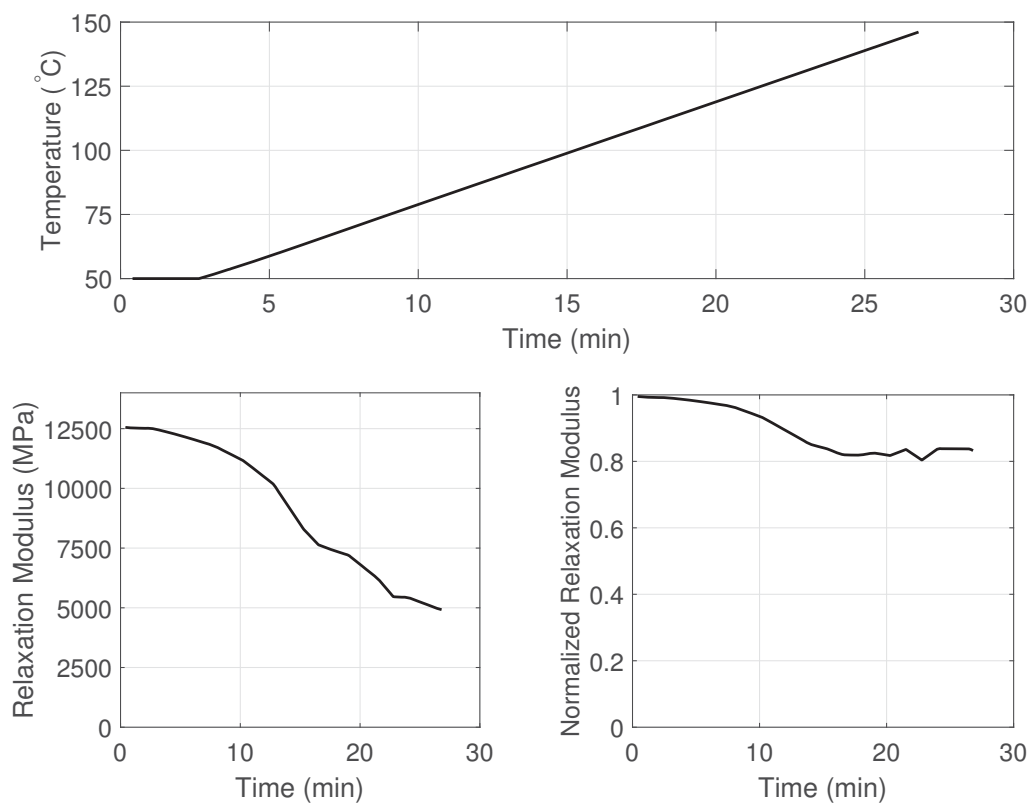
Figure 6.15.: Time-temperature history during nonisothermal relaxation experiment (top) and modeled relaxation modulus (bottom left) and normalized relaxation modulus (bottom right).

The same was repeated for a nonisothermal relaxation test started at 60°C and ramped at 3°C/min to 150°C. The results are shown in figures 6.16 and 6.17. The final values and general behavior of the modeled and measured values are in good agreement, however discrepancy exists at the early temperatures. This is attributed to the Q800 DMA malfunctioning during nonisothermal isostrain tests. Many tests failed due to the controllers not being optimized for temperature ramp isostrain tests.
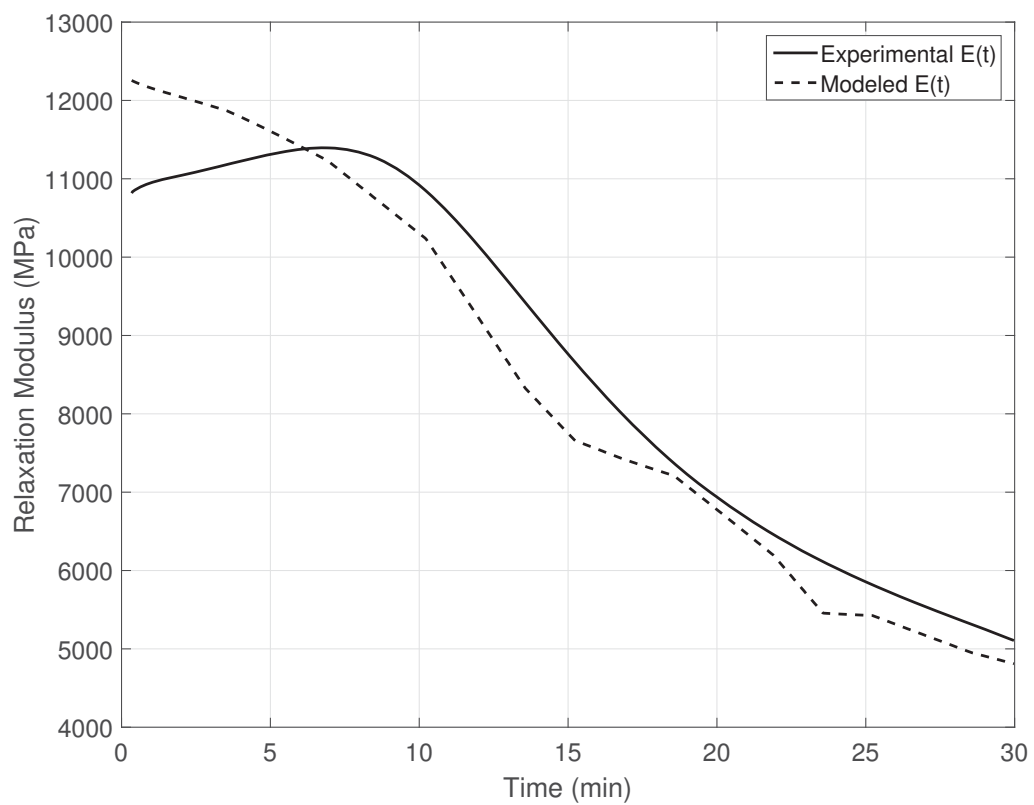
Figure 6.16.:   Experimental and modeled nonisothermal relaxation modulus curves.
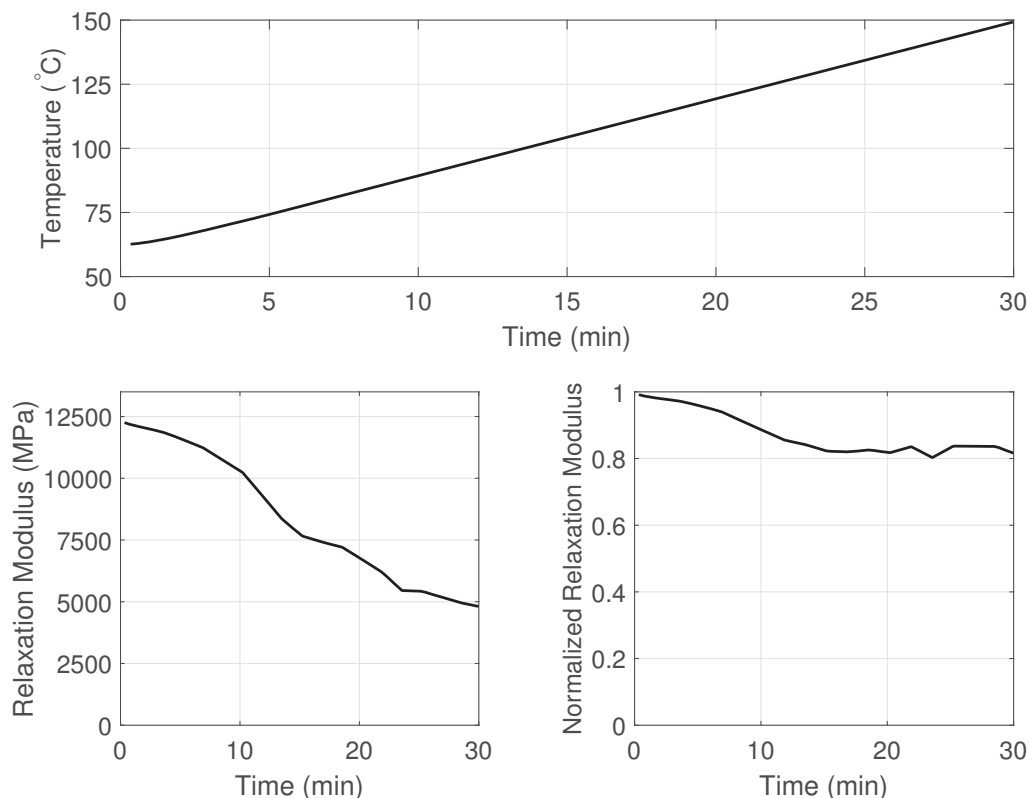
Figure 6.17.: Time-temperature history during nonisothermal relaxation experiment (top) and modeled relaxation modulus (bottom left) and normalized relaxation modulus (bottom right).

6.5 Summary

In this chapter, the viscoelastic properties of 50 weight percent carbon fiber-reinforced PPS were characterized and discussed in the context of stress relaxation during large-scale FDM and the target application of composite tooling. Temperature sweep DMA experiments were conducted and revealed the significant increase in high temperature properties arising from the crystallinity. A creep test revealed that the material creeps at 180°C, and that dimensional stability under the high pressures of an autoclave at this temperature may not be certain. Fortunately, 180°C is only used for curing high performance composites, and many other composite manufacturing processes are conducted at lower temperatures where the reinforced PPS is likely

suitable. Stress relaxation tests revealed that the stresses decay exponentially to a relaxed state, and that a post-printing annealing step should be conducted at a temperature approaching T_m in order to maximize relaxation. Generalized Maxwell models were fit to the relaxation experiments, and a linear interpolation method was used to generate relaxation modulus and normalized relaxation modulus surface plots over time and temperature. These surfaces can be used to reasonably predict nonisothermal stress relaxation that occurs as a printed part cools. In addition, the surfaces contain the required modulus versus time and temperature data that would be required to predict deformations that could arise from residual stresses.

CHAPTER 7. RECOMMENDATIONS

This work presents new opportunities made possible by AM of high temperature fiber-reinforced polymers, and also identifies challenges and the need for further research and advancement from groups like our own. One of the greatest challenges to overcome is the anisotropy that results in printed structures. For use in high temperature tooling applications, a combination of high stiffness, low CTE, and high HDT is required in all directions. This can be achieved by developing dies that result in broader fiber orientation distributions, or by truly printing in 3 dimensions rather than in 2 dimensions over and over. Specific print paths can likely result in near quasi-isotropic properties, however low stiffness and strength in the z direction will still exist. The development of extruder screws that inflict less damage on fibers would also be beneficial, however longer fibers would not address anisotropy, and may be more difficult for new dies to orient away from the print direction.

The presence of residual stresses introduces challenges with scaling the technology. Although the lab-scale system has the ability to print structures approximately a half meter tall, this may not be possible without greatly speeding up the process in order to lessen the temperature gradients. Currently, printing parts taller than 10 cm is challenging due to the resulting warpage. To date, only amorphous polymers (various grades of ABS) have been extensively tested on the large-scale. Since amorphous polymers do not experience crystallization shrinkage, lower residual stresses may arise when upper layers solidify and cool on top of previously cooled layers. Also, stress relaxation can likely occur to a greater extent in these polymers due to the absence of spherulites tying molecules together. Another distinguishing factor of amorphous polymers is their typically higher T_g than semicrystalline polymers due to their more bulky chain structure. Therefore, further work printing and investigating

reinforced polyetherimide (PEI) is recommended. PEI has a higher strength, lower CTE, and similar modulus to reinforced PPS, making the material very attractive for high temperature tooling applications.

LIST OF REFERENCES

LIST OF REFERENCES

[1] Mark Cotteleer. 3d opportunity for production: Additive manufacturing makes its (business) case. *Deloitte Review*, (15):146–161, 2014.

[2] Hybrid Manufacturing. 7 families of additive manufacturing quick reference guide. In *Additive Manufacturing Conference*.

[3] Halil L. Tekinalp, Vlastimil Kunc, Gregorio M. Velez-Garcia, Chad E. Duty, Lonnie J. Love, Amit K. Naskar, Craig A. Blue, and Soydan Ozcan. Highly oriented carbon fiberpolymer composites via additive manufacturing. *Composites science and technology*, 105:144–150, 2014.

[4] M. Nikzad, S. H. Masood, and I. Sbarski. Thermo- mechanical properties of a highly filled polymeric composites for fused deposition modeling. *Materials and Design*, 32(6):3448–3456, 2011.

[5] M. L. Shofner, K. Lozano, F. J. Rodrguezmacas, and E. V. Barrera. Nanofiber reinforced polymers prepared by fused deposition modeling. *Journal of Applied Polymer Science*, 89(11):3081–3090, 2003.

[6] Weihong Zhong, Fan Li, Zuoguang Zhang, Lulu Song, and Zhimin Li. Short fiber reinforced composites for fused deposition modeling. *Materials Science and Engineering A*, 301(2):125–130, 2001.

[7] W. Gray I. V. Robert, G. Baird Donald, and Bhn Jan Helge. Effects of processing conditions on short tlcp fiber reinforced fdm parts. *Rapid Prototyping Journal*, 4(1):14–25, 1998.

[8] Laboratory Oak Ridge National, United States. Dept. of Energy. Office of Energy Efficiency, and Renewable Energy. *Cincinnati Big Area Additive Manufacturing (BAAM)*. Washington, D.C. : United States. Dept. of Energy. Office of Energy Efficiency and Renewable Energy ; Oak Ridge, Tenn. : distributed by the Office of Scientific and Technical Information, U.S. Dept. of Energy, Washington, D.C. : Oak Ridge, Tenn., 2015.

[9] Tim A. Osswald. *Understanding polymer processing : processes and governing equations*. Munich : Hanser Publishers ; Cincinnati : Hanser Publications, Munich : Cincinnati, 2011.

[10] R. S. Dave and A. C. Loos. *Processing of composites*. Munich : Hanser Publishers ; Cincinnati : Hanser/Gardner Publications, Munich : Cincinnati, 2000.

[11] S. Y. Fu, B. Lauke, E. Mder, C. Y. Yue, and X. Hu. Tensile properties of short- glass- fiber- and short- carbon- fiber- reinforced polypropylene composites. *Composites Part A: Applied Science and Manufacturing*, 31(10):1117–1125, 2000.

[12] H. J. Wolf. Screw plasticating of discontinuous fiber filled thermoplastic: Mechanisms and prevention of fiber attrition. *Polymer Composites*, 15(5):375–383, 1994.

[13] Randy S. Bay and Charles L. Tucker. Stereological measurement and error estimates for three dimensional fiber orientation. *Polymer Engineering and Science*, 32(4):240–253, 1992.

[14] Baam fact sheet. http://wwwassets.e-ci.com/PDF/Products/baam-fact-sheet.pdf.

[15] Vlastimil Kunc. Advances and challenges in large scale polymer additive manufacturing. In *Society of Plastics Engineering*.

[16] Hongyu Cui. *Glass fiber reinforced biorenewable polymer composites and the fabrication with pultrusion process*. Thesis, 2013.

[17] A. Vaxman, M. Narkis, A. Siegmann, and S. Kenig. Short fiber reinforced thermoplastics. i. rheological properties of glass fiber reinforced noryl. *Polymer Composites*, 10(2):78–83, 1989.

[18] Wen-Yen Chiu and Goang-Ding Shyu. The study on die swell, fiber length distribution, and crystallinity of pp composite through extrusion. *Journal of Applied Polymer Science*, 34(4):1493–1501, 1987.

[19] A Vaxman, M Narkis, A Siegmann, and S Kenig. Short-fiber-reinforced thermoplastics. part iii: Effect of fiber length on rheological properties and fiber orientation. *Polymer composites*, 10(6):454–462, 1989.

[20] Jerry Sengshiu Chung and Peggy Cebe. Melting behaviour of poly (phenylene sulphide): 1. single-stage melt crystallization. *Polymer*, 33(11):2312–2324, 1992.

[21] L D'Ilario and A Martinelli. Glass transition and the origin of poly (p-phenylene sulfide) secondary crystallization. *The European Physical Journal E*, 19(1):37–45, 2006.

[22] JM Kenny and A Maffezzoli. Crystallization kinetics of poly (phenylene sulfide)(pps) and pps/carbon fiber composites. *Polymer Engineering & Science*, 31(8):607–614, 1991.

[23] Mark Cotteleer, Mark Neier, and Jeff Crane. 3d opportunity in tooling: Additive manufacturing shapes the future. *Deloitte Review*, 2014.

[24] Celanese. Celstran lfrt automotive powerpoint. 2013.

[25] Bill Macy. Rapid/affordable composite tooling strategies utilizing fused deposition modeling. *SAMPE Journal*, 47(4), 2011.

[26] I. M. Ward. *An introduction to the mechanical properties of solid polymers.* Hoboken, NJ : Wiley, Hoboken, NJ, 2nd ed.. edition, 2004.

[27] N. G. McCrum. *Principles of polymer engineering.* Oxford ; New York : Oxford University Press, Oxford ; New York, 2nd ed.. edition, 1997.

[28] David Roylance. Engineering viscoelasticity. *Department of Materials Science and Engineering–Massachusetts Institute of Technology, Cambridge MA*, 2139:1–37, 2001.

[29] H. F. Brinson and L. C. Brinson. *Polymer engineering science and viscoelasticity : an introduction.* New York : Springer, New York, 2008.

[30] Lawrence E Nielsen and Fred D Stockton. Theory of the modulus of crystalline polymers. *Journal of Polymer Science Part A: General Papers*, 1(6):1995–2002, 1963.

[31] Lawrence E. Nielsen. *Mechanical properties of polymers and composites.* New York : M. Dekker, New York, 2nd ed., rev. and expanded.. edition, 1994.

[32] DW Woods. Effects of crystallization on the glass-rubber transition in polyethylene terephthalate filaments. *Nature*, 174:753–754, 1954.

[33] S Newman and WP Cox. The glass temperature of semicrystalline polymers. *Journal of Polymer Science*, 46(147):29–49, 1960.

[34] AC Bernardo. How to get more from glass-fiber reinforced hdpe. *SPE JOURNAL*, 26(10):39, 1970.

[35] Michael T Takemori. Towards an understanding of the heat distortion temperature of thermoplastics. *Polymer Engineering & Science*, 19(15):1104–1109, 1979.

[36] EA Noga and RT Woodhams. Asbestos-reinforced thermoplastics. *SPE JOURNAL*, 26(9):23, 1970.

[37] FG Krautz. Glass fiber enhances high-temperature performance of thermoplastics. *SPE JOURNAL*, 27(8):74, 1971.

[38] Dynamic mechanical analysis. http://www.tainstruments.com/pdf/brochure.

[39] Edith A Turi. *Thermal Characterization of Polymeric Materials*, volume I. Academic Press, Brooklyn, New York, second edition, 1997.

[40] Hua Gao, Yong-ming Song, Qing-wen Wang, Zhen Han, and Ming-li Zhang. Rheological and mechanical properties of wood fiber-pp/pe blend composites. *Journal of Forestry Research*, 19(4):315–318, 2008.

APPENDIX

APPENDIX

A.1   Photographs
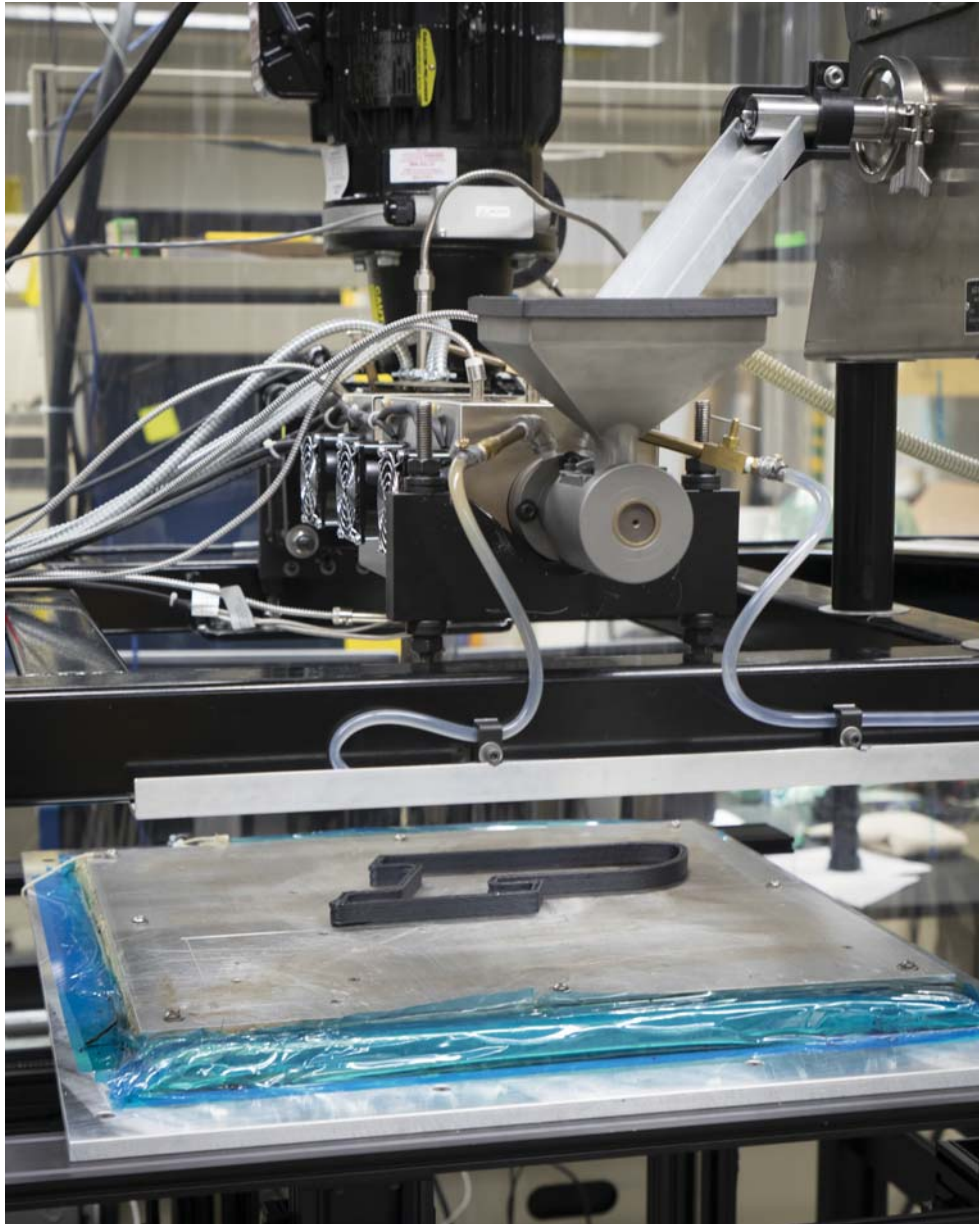
Figure A.1.:   Completed lab-scale FDM system.

Figure A.2.:   Completed lab-scale FDM system.

Figure A.3.:   Printed tool prior to machining.

A.2   DSC Thermographs
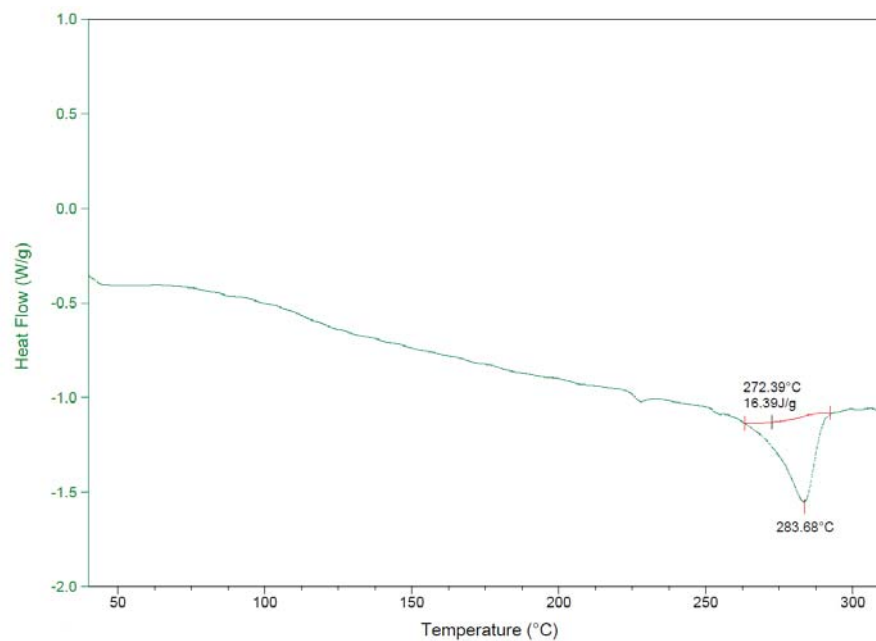
(a)
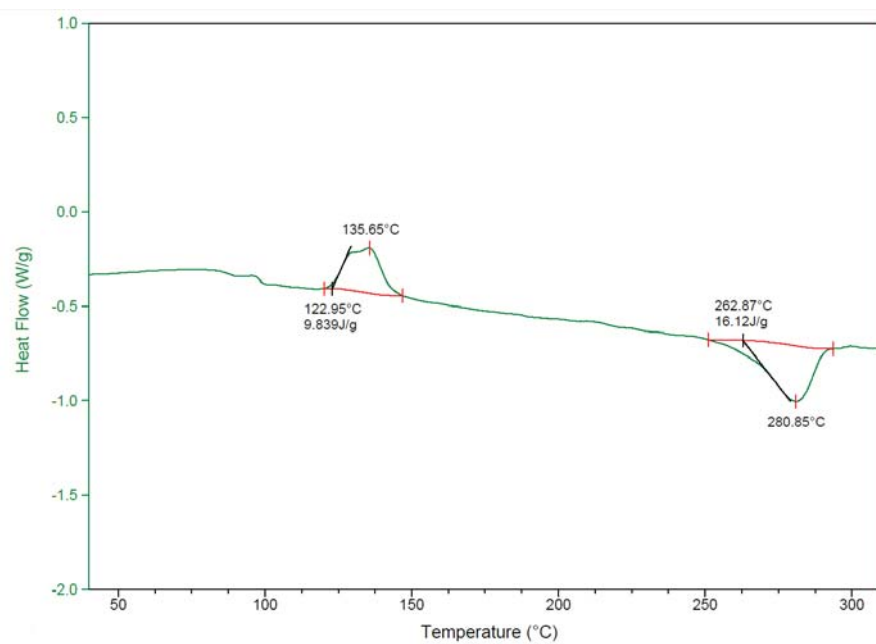
(b)

Figure A.4.: DSC thermographs of annealed (a) and quenched (b) samples used in DMA tests.

A.3   Stress Relaxation Models

A.3.1   Plots
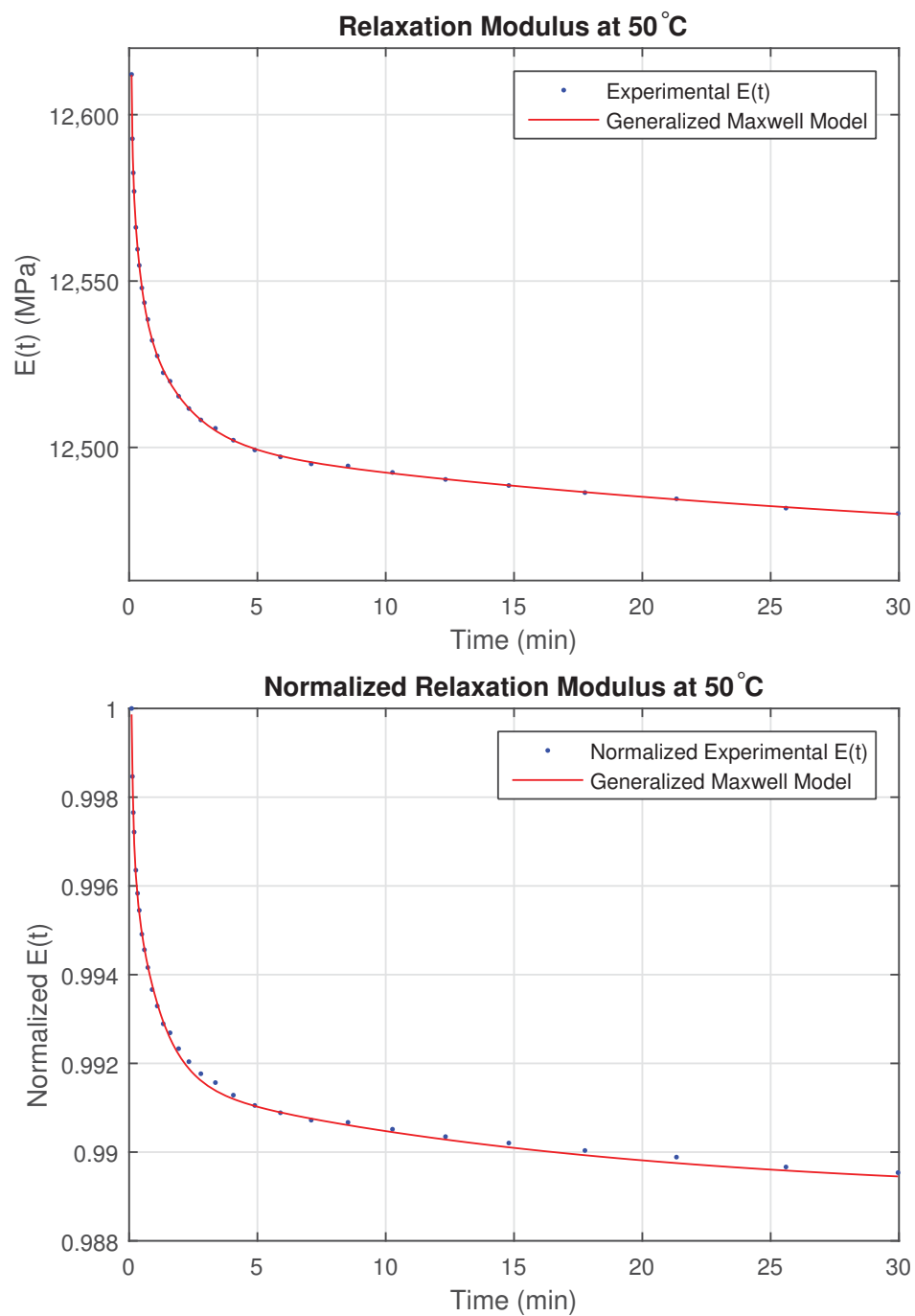
Figure A.5.: Relaxation modulus at 50°C.
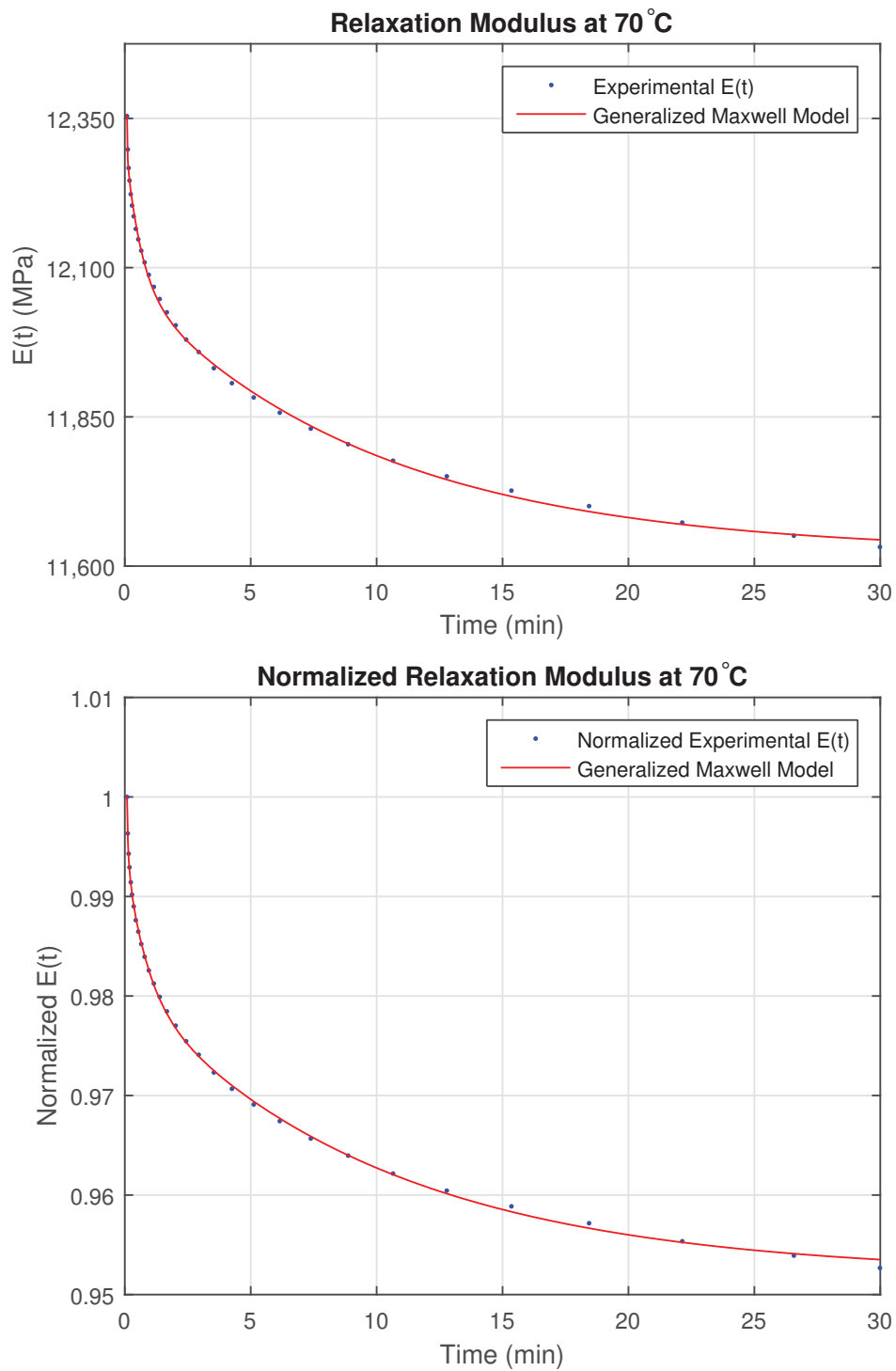
Figure A.6.: Relaxation modulus at 70°C.
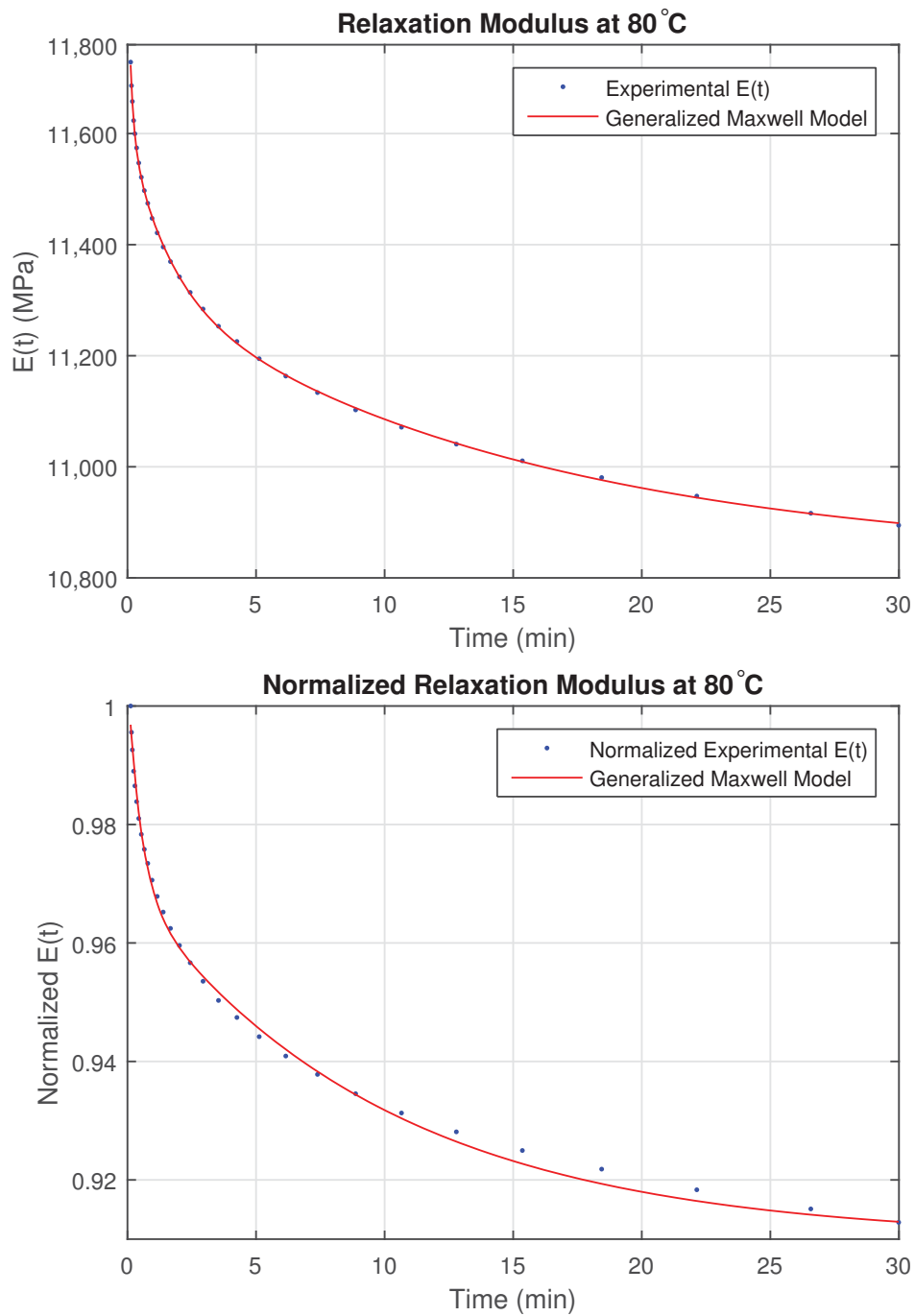
Figure A.7.: Relaxation modulus at 80°C.
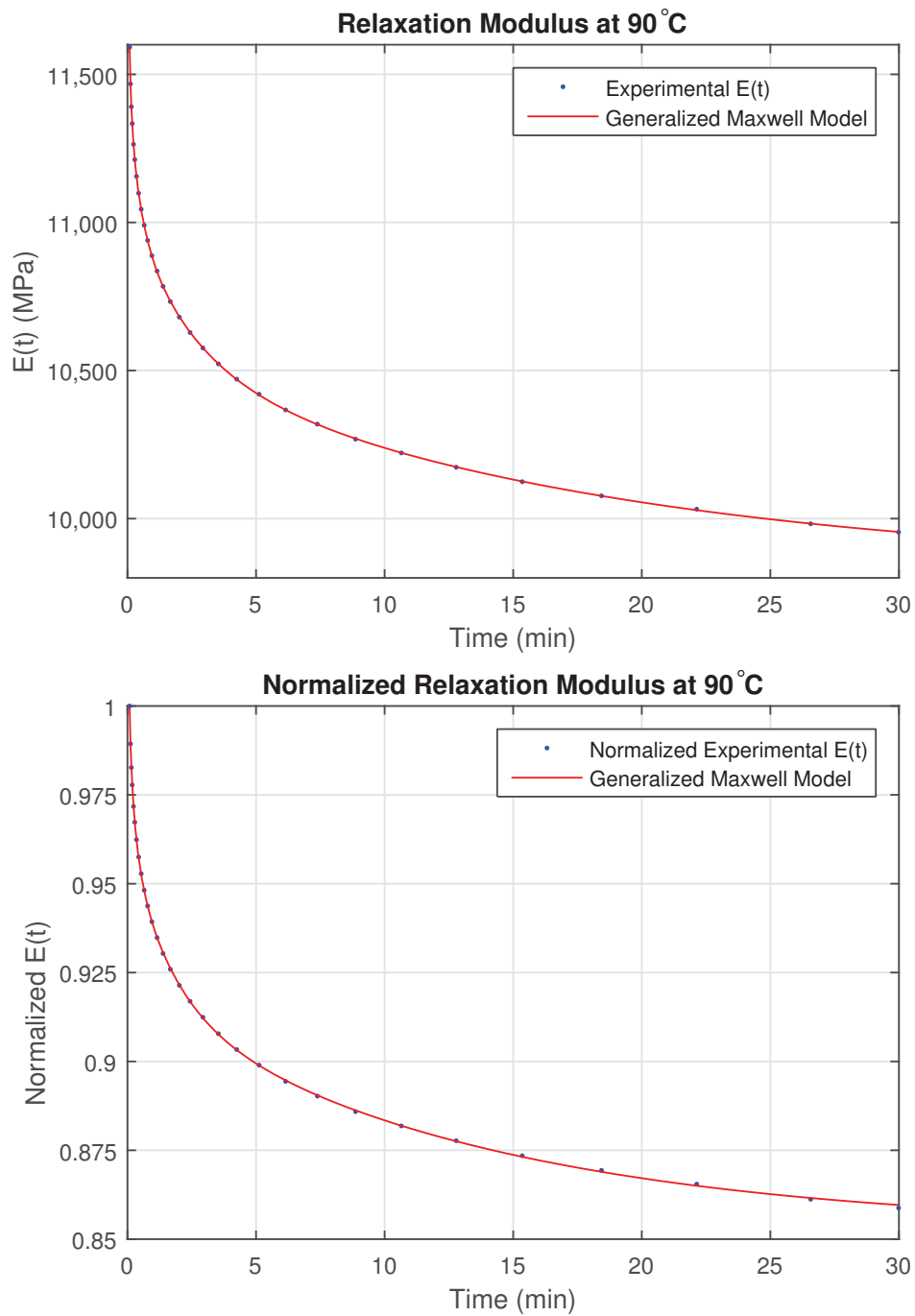
Figure A.8.: Relaxation modulus at 90°C.
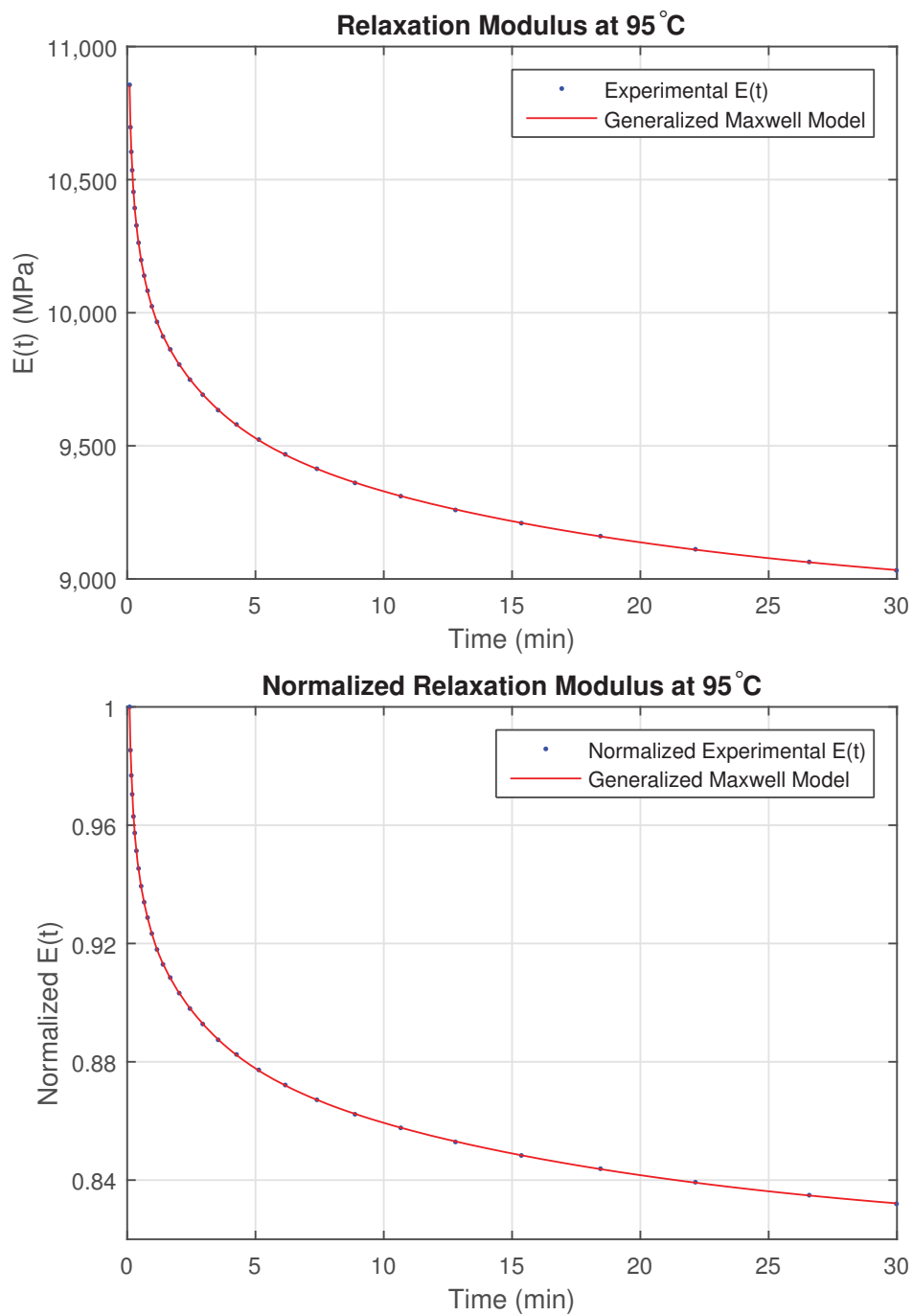
Figure A.9.: Relaxation modulus at 95°C.
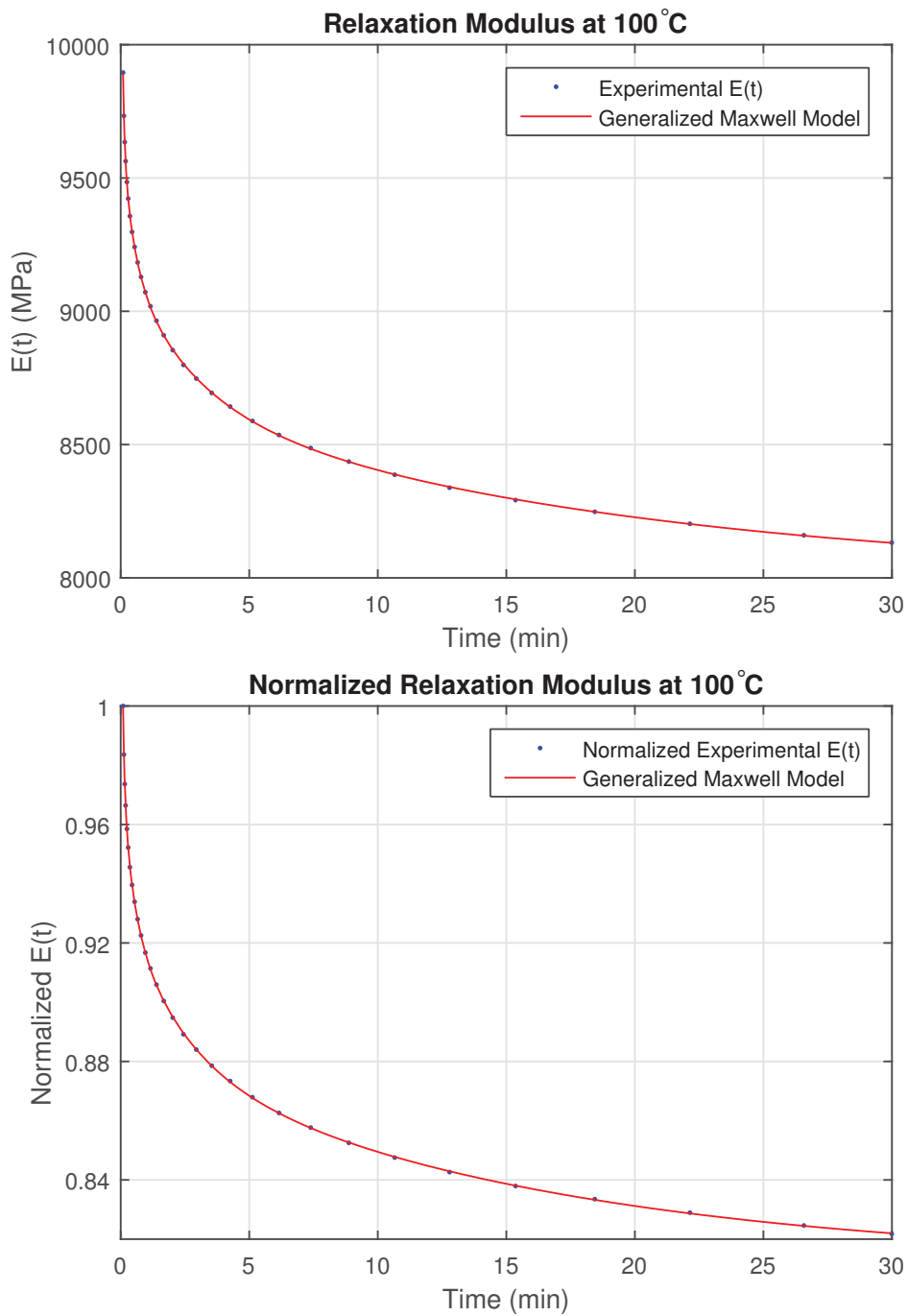
Figure A.10.: Relaxation modulus at 100°C.
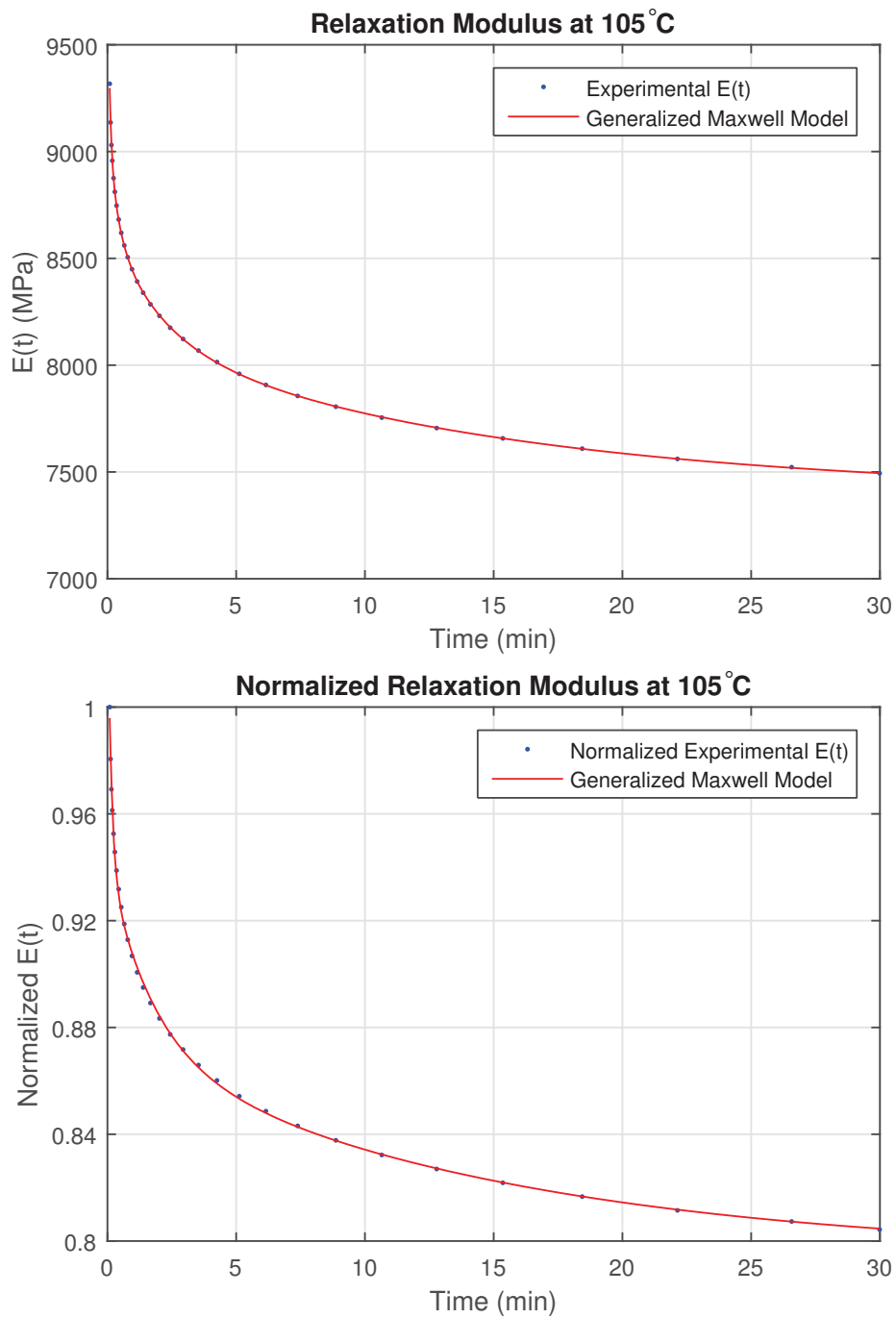
Figure A.11.: Relaxation modulus at 105°C.
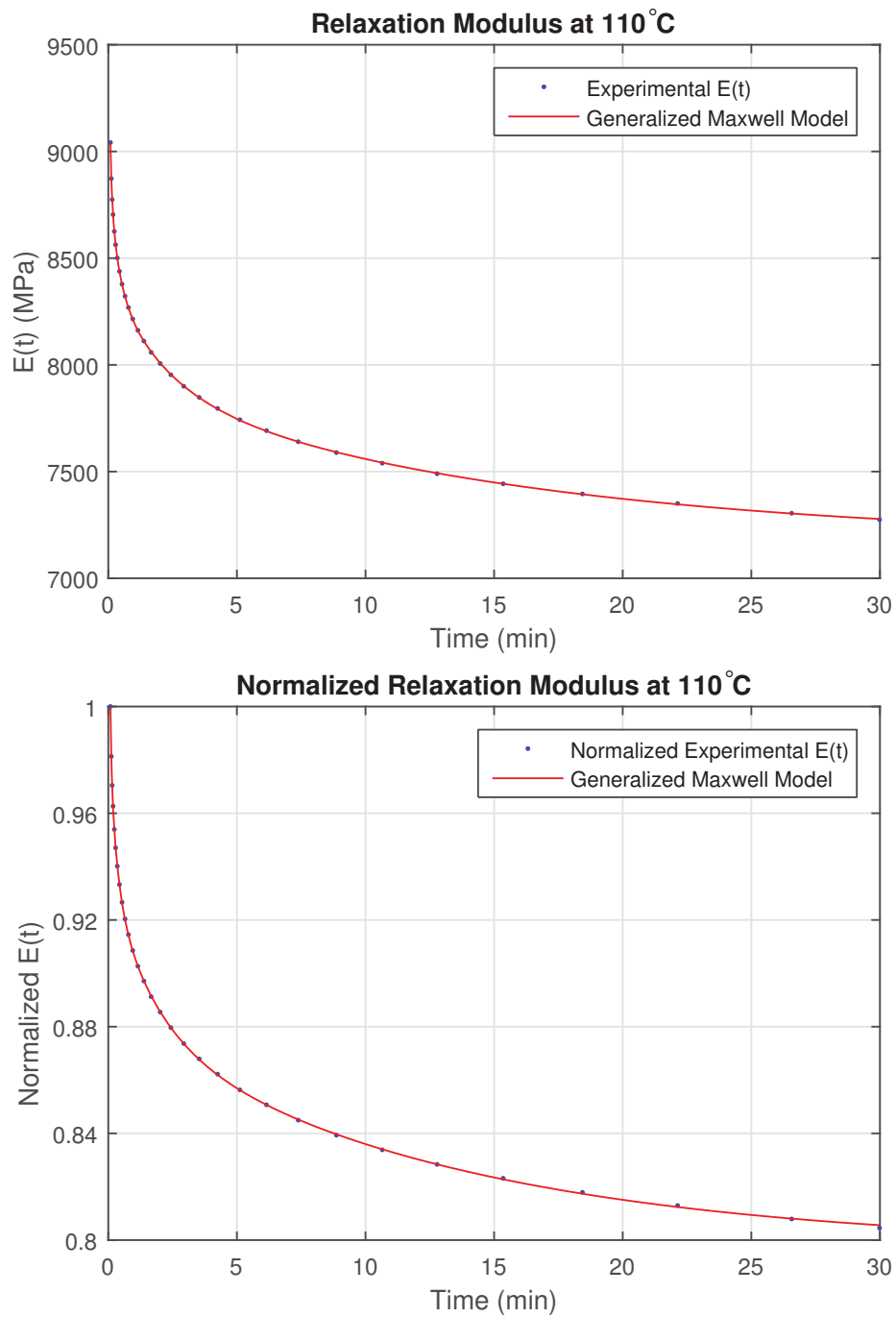
Figure A.12.: Relaxation modulus at 110°C.
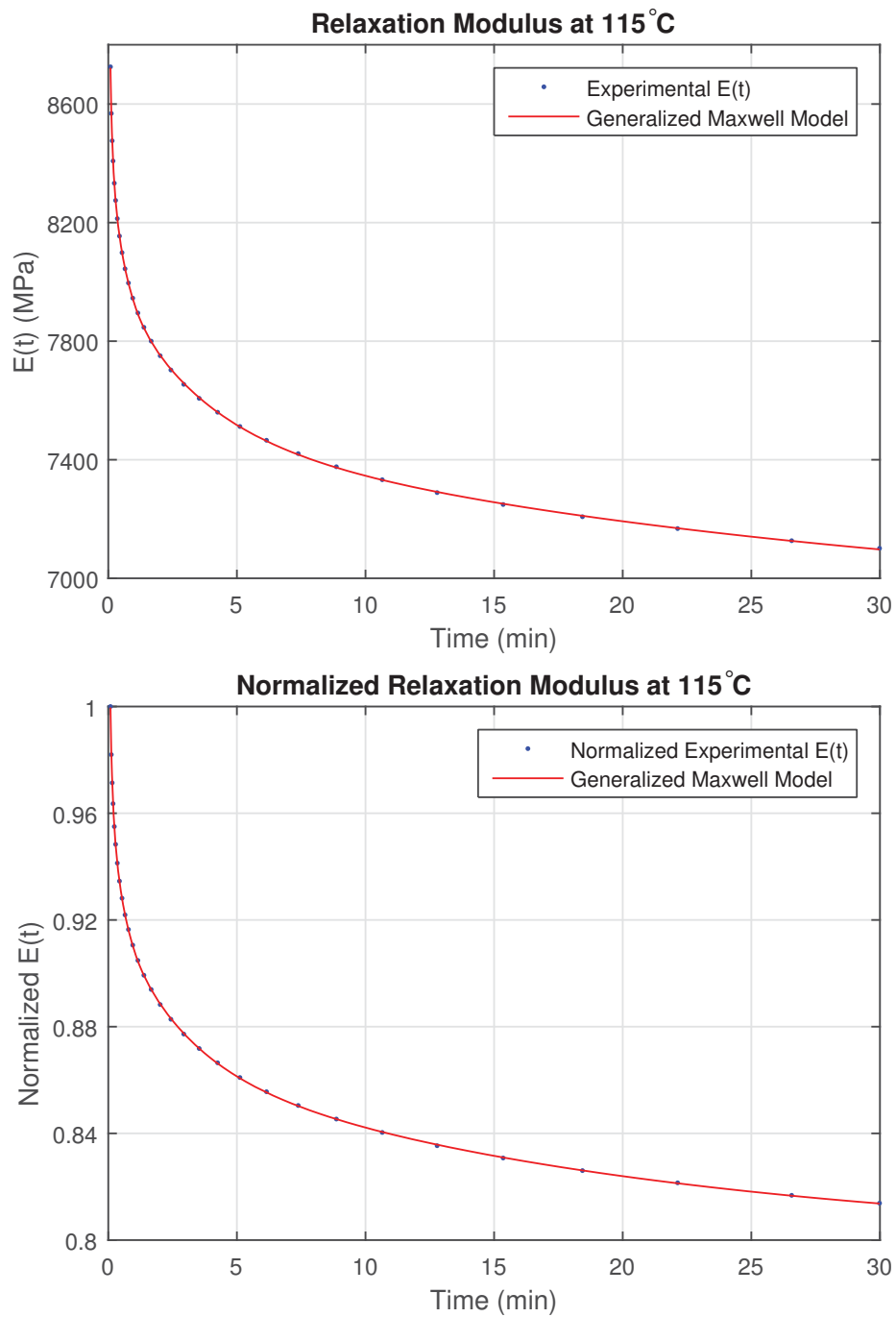
Figure A.13.: Relaxation modulus at 115°C.
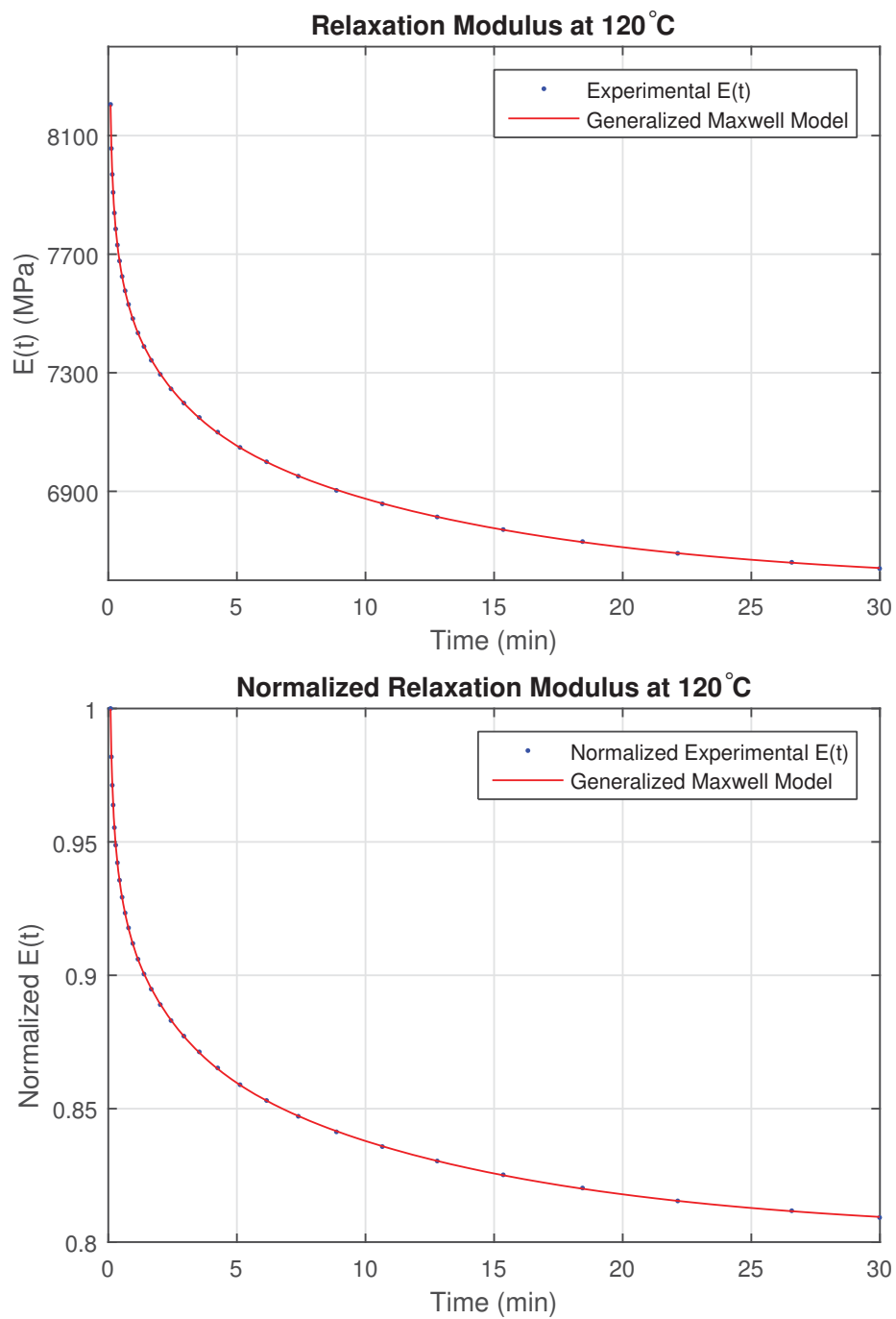
Figure A.14.: Relaxation modulus at 120°C.
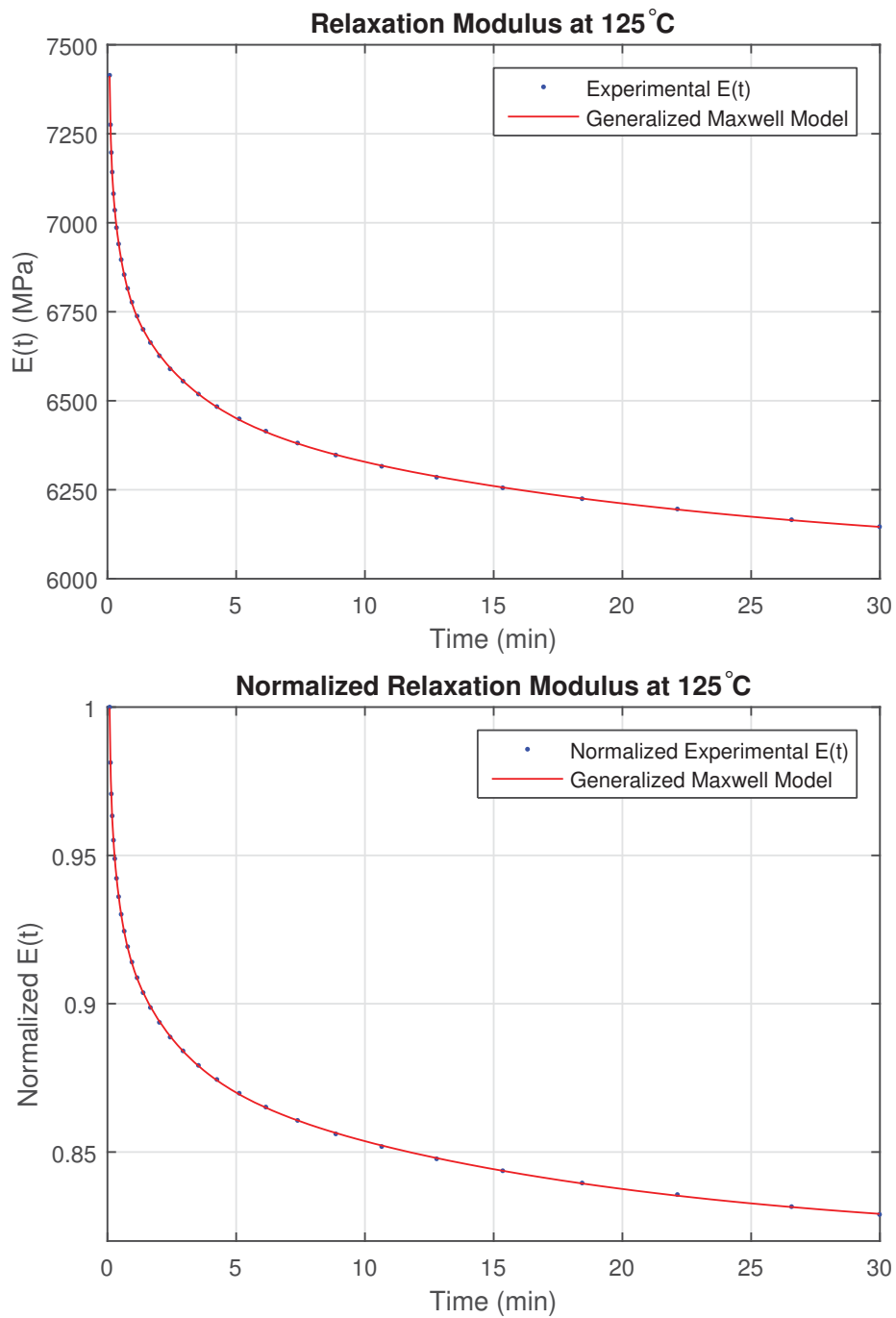
Figure A.15.: Relaxation modulus at 125°C.
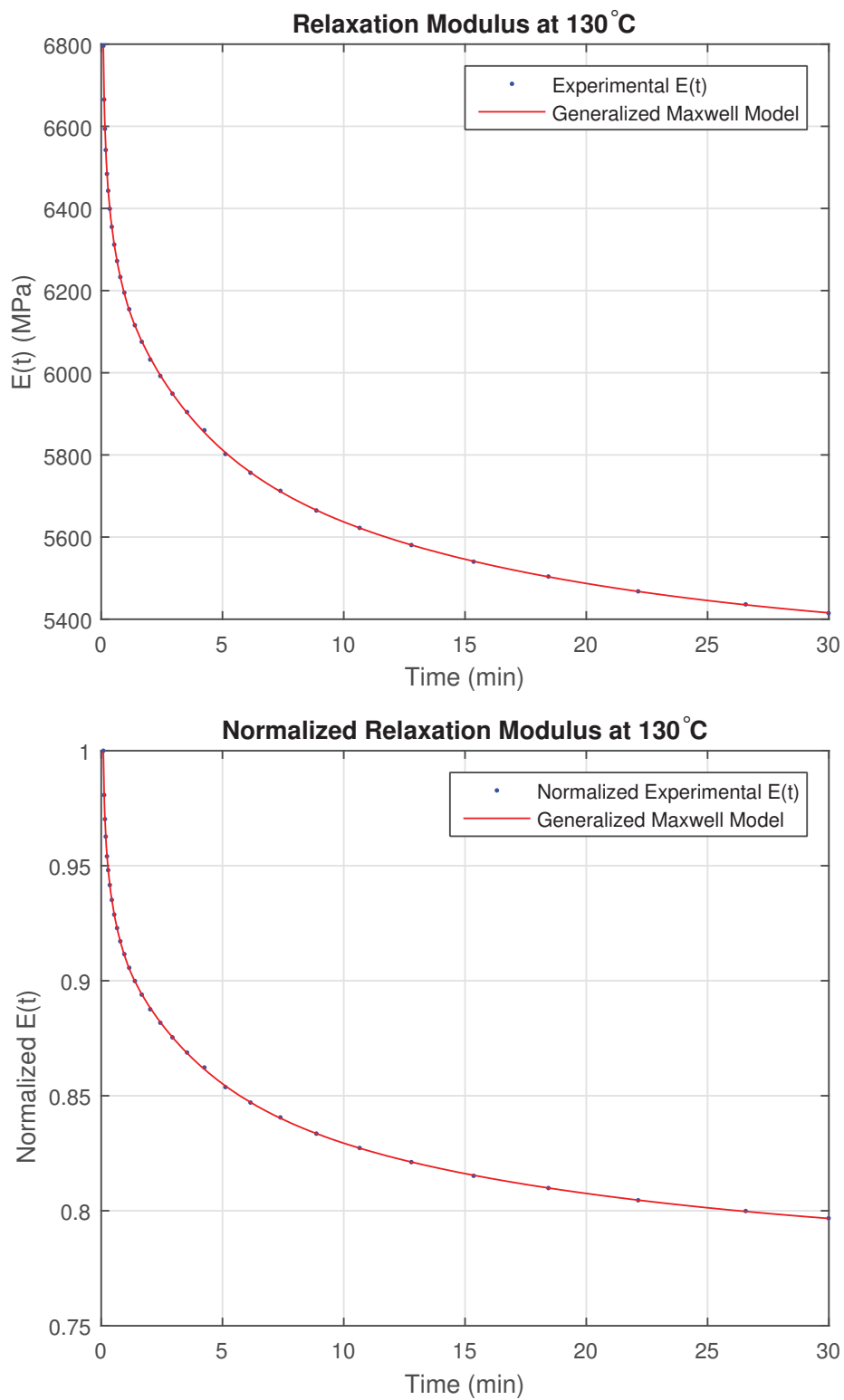
Figure A.16.: Relaxation modulus at 130°C.
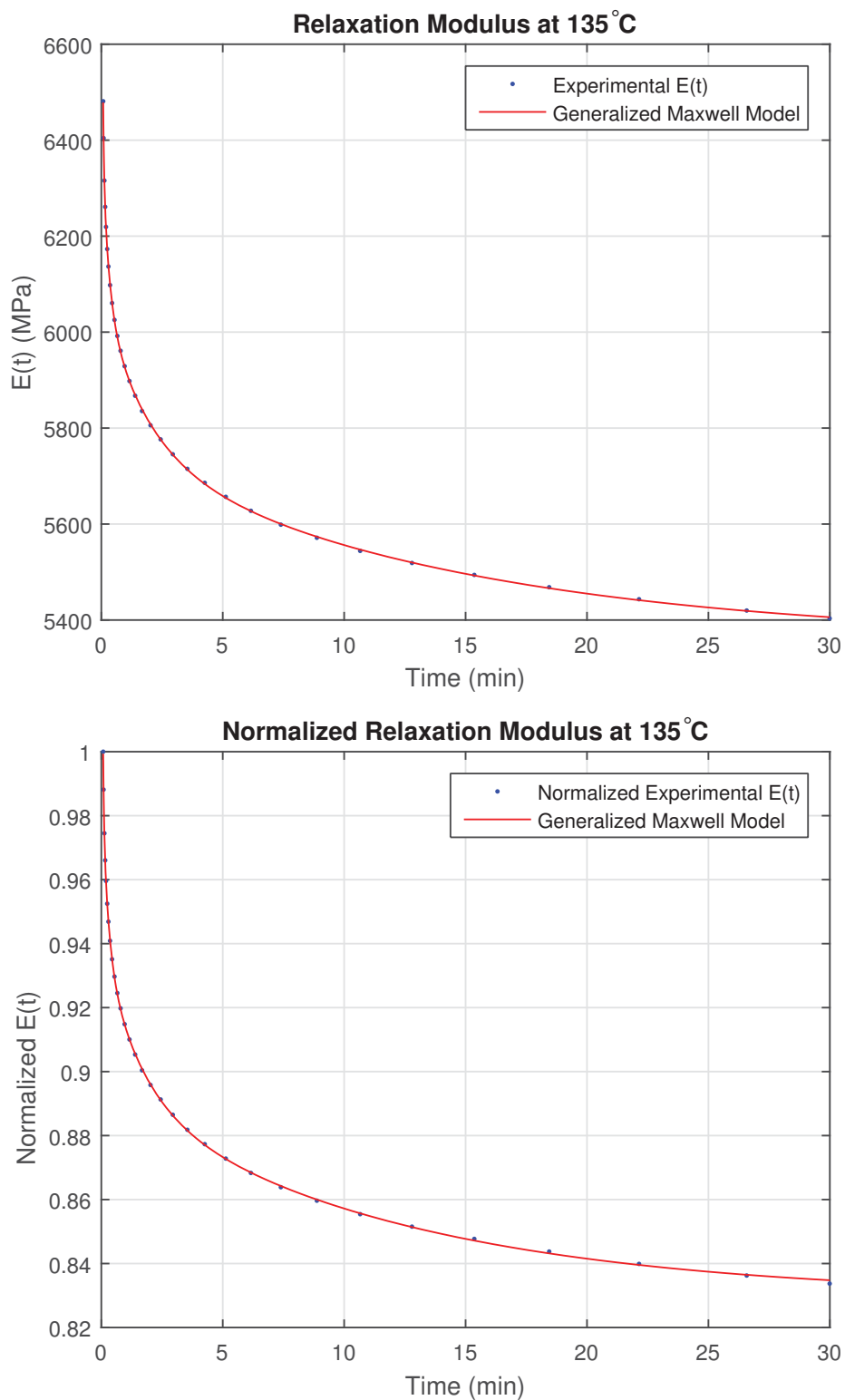
Figure A.17.: Relaxation modulus at 135°C.
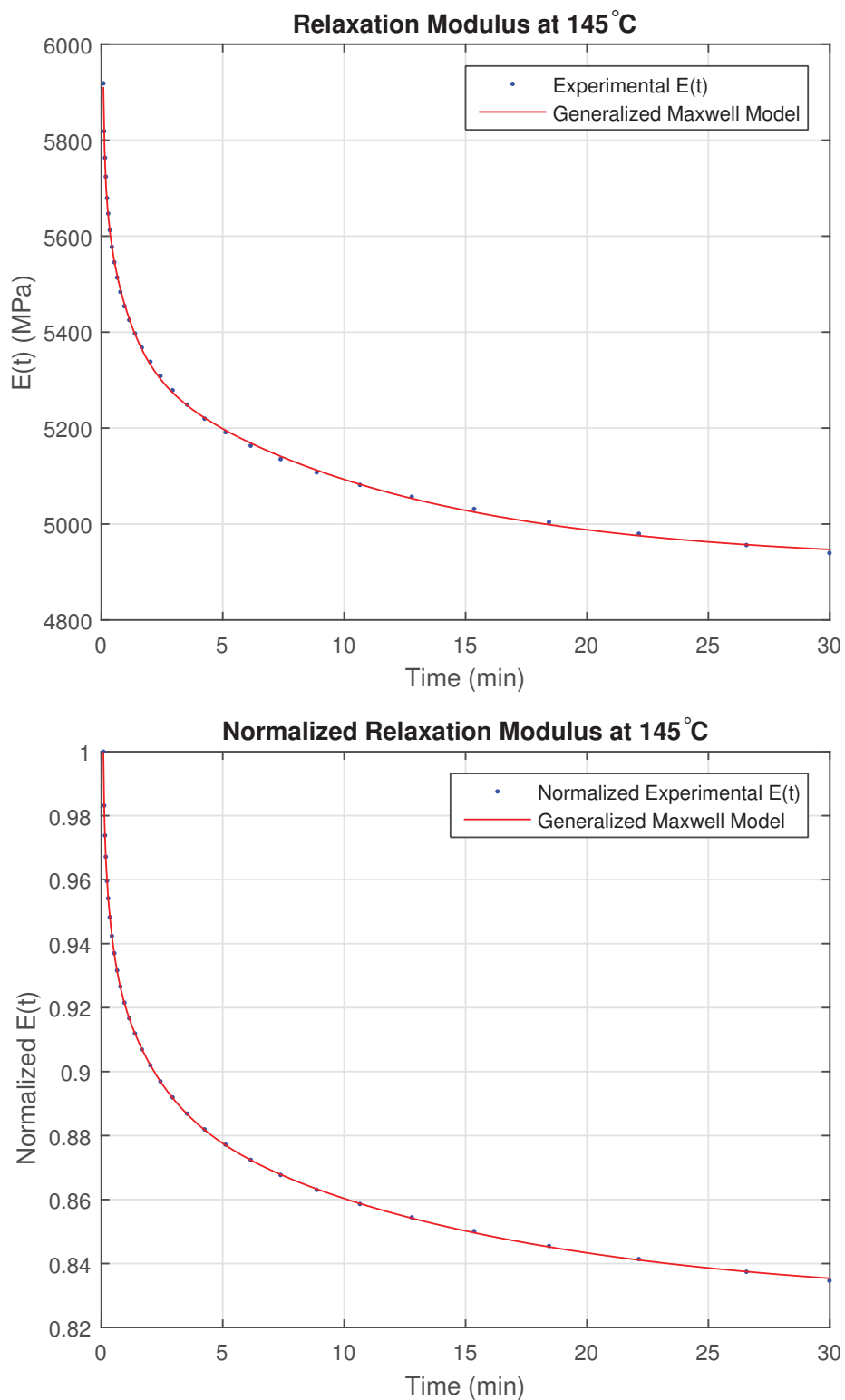
Figure A.18.: Relaxation modulus at 145°C.
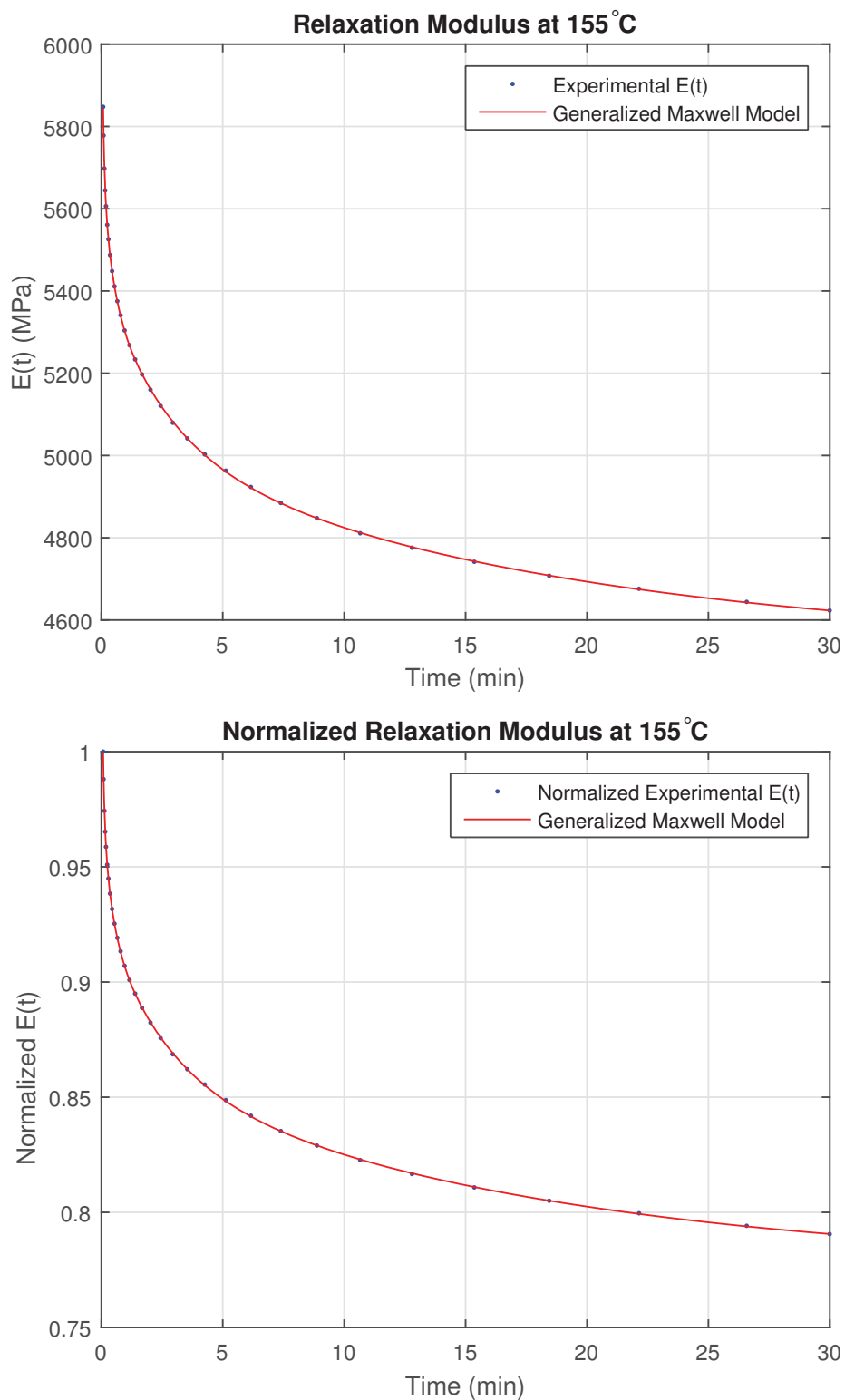
Figure A.19.: Relaxation modulus at 155°C.
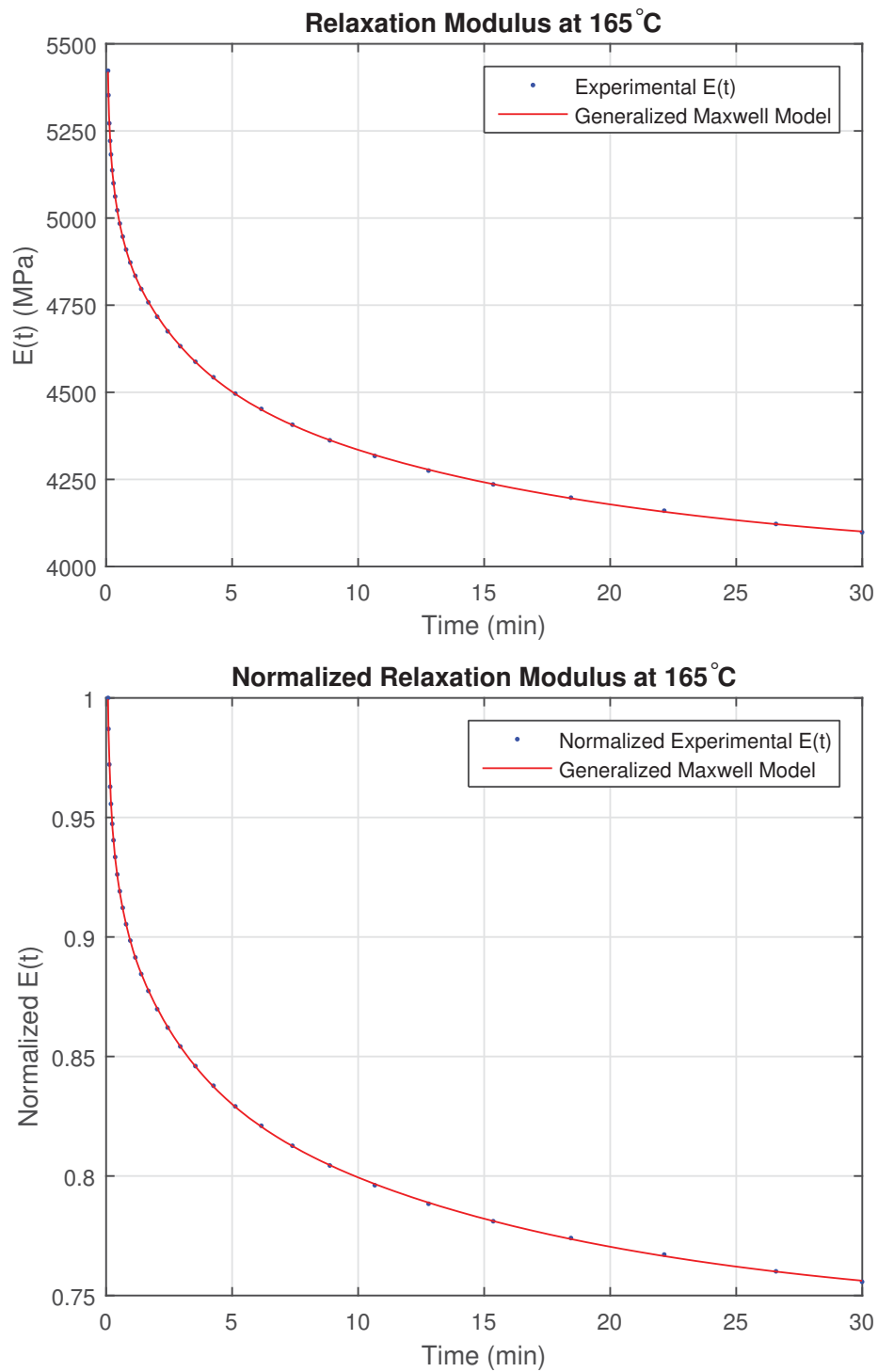
Figure A.20.: Relaxation modulus at 165°C.
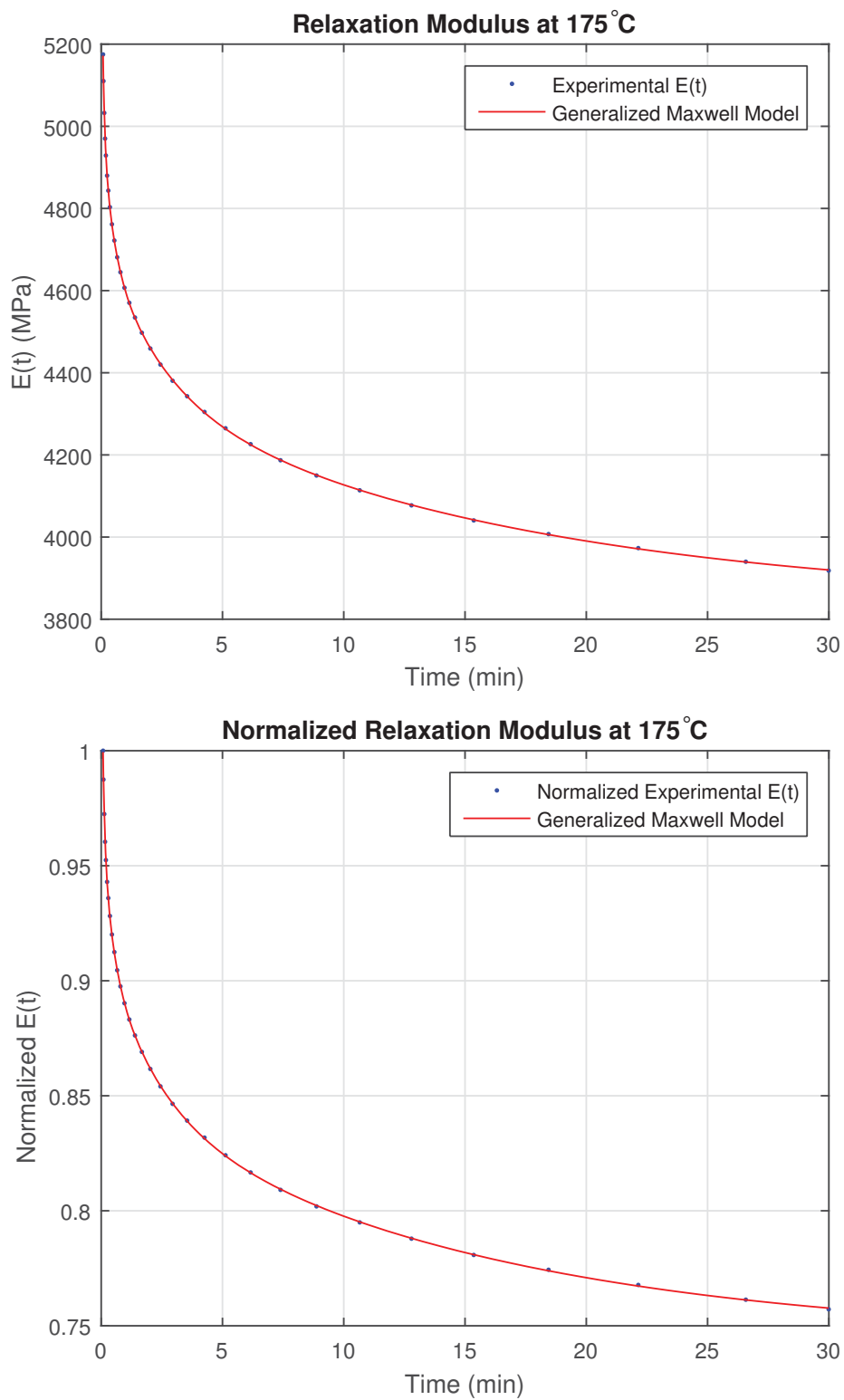
Figure A.21.: Relaxation modulus at 175˚C.
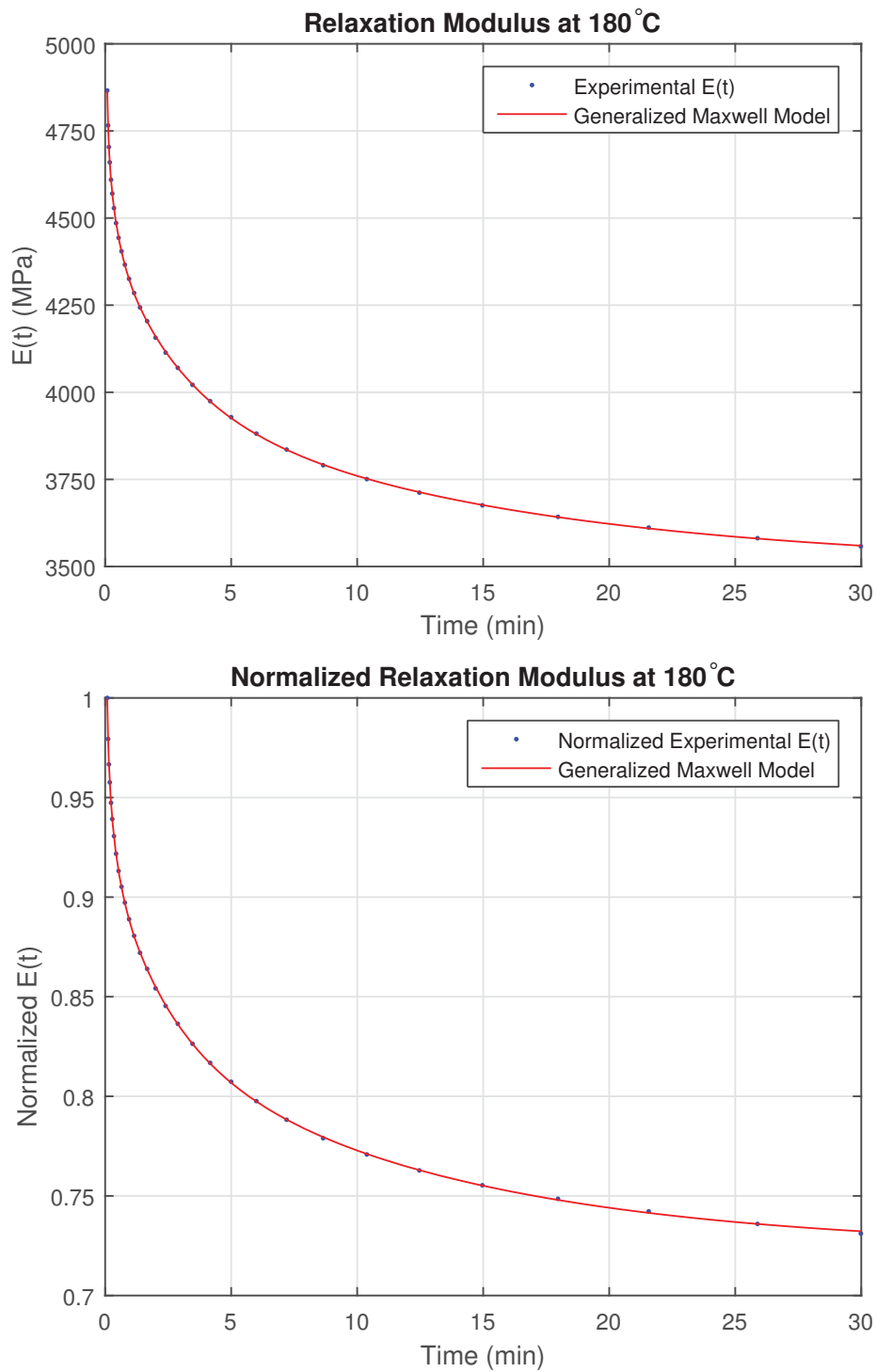
Figure A.22.: Relaxation modulus at 180°C.
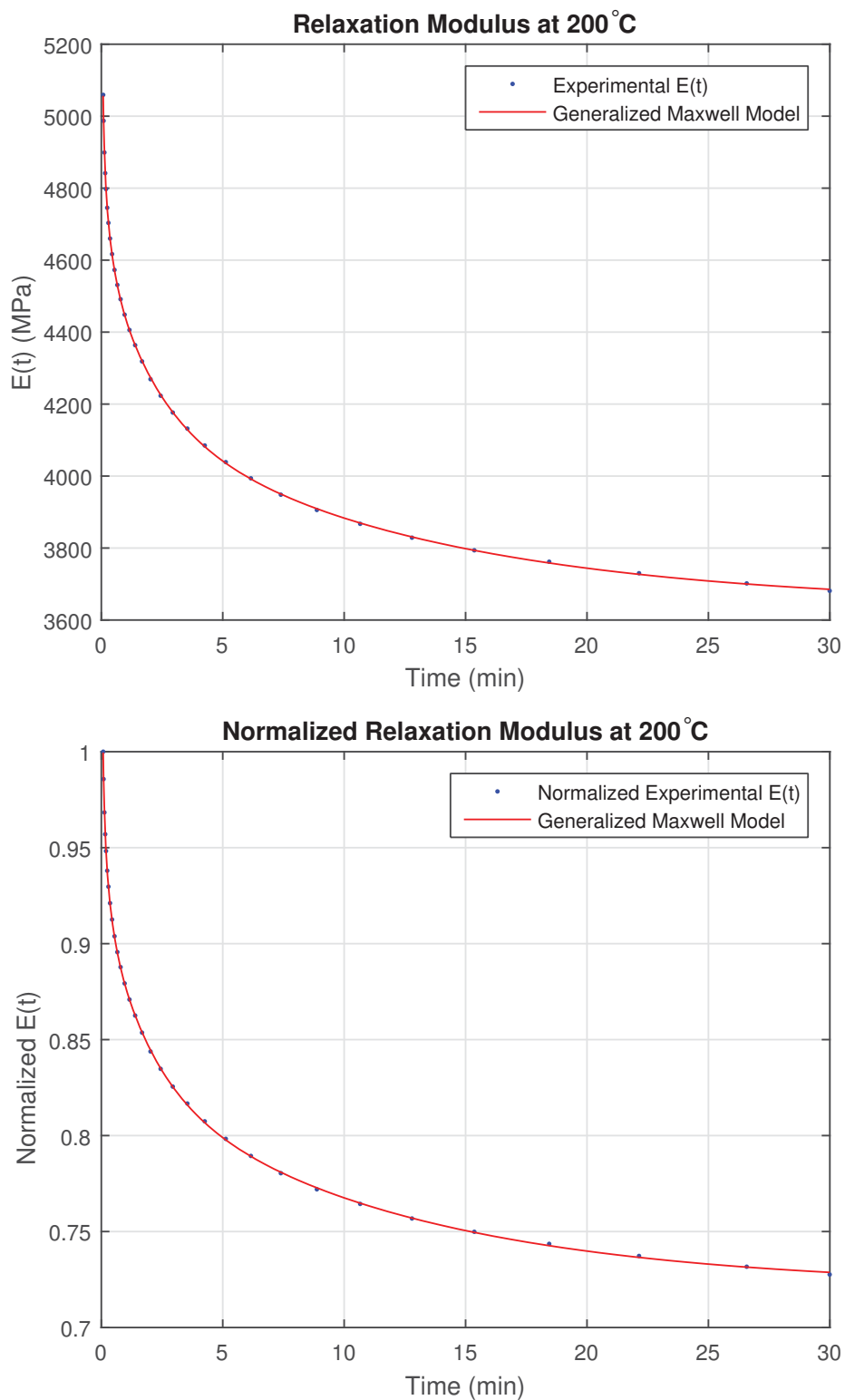
Figure A.23.: Relaxation modulus at 200°C.
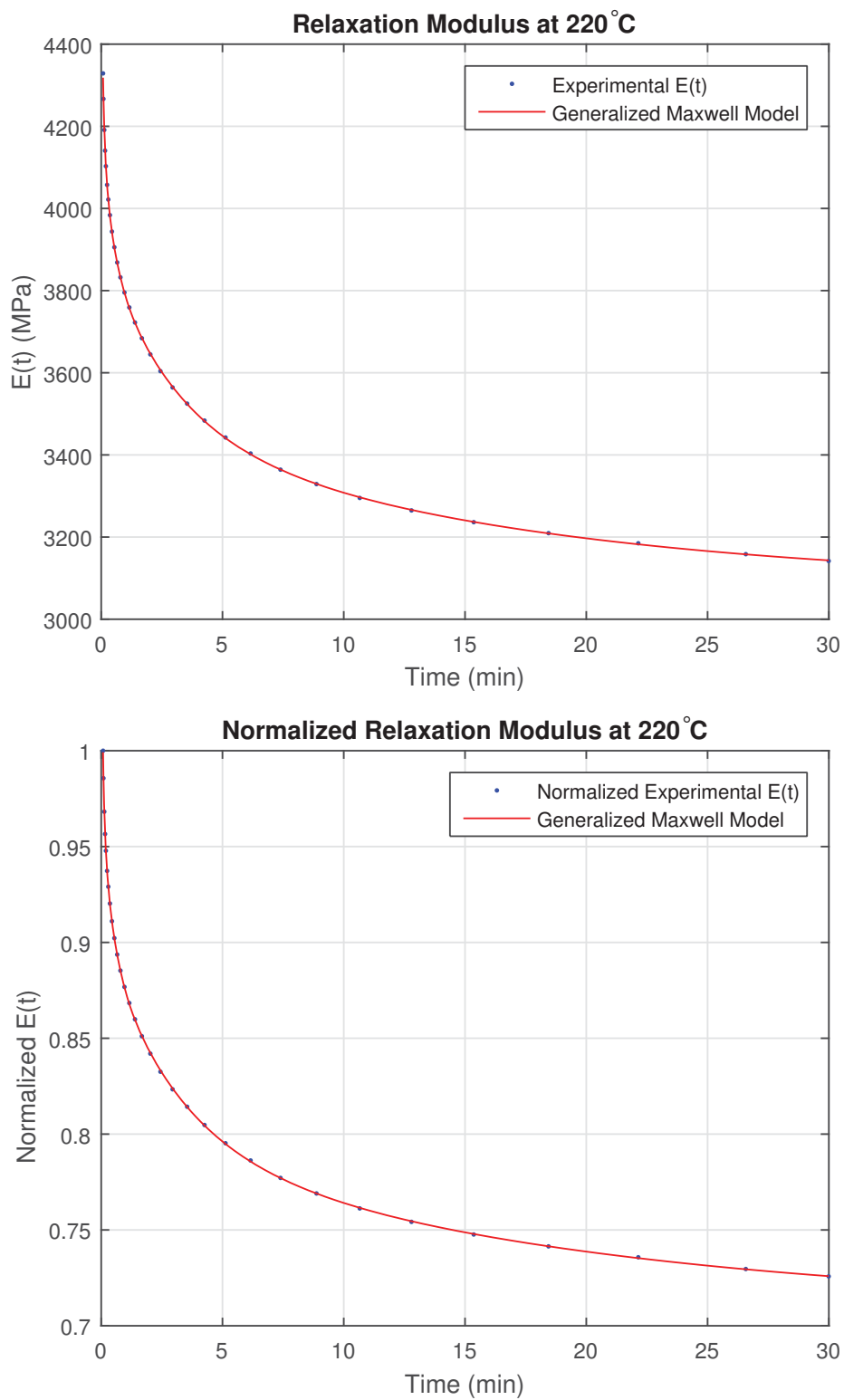
Figure A.24.: Relaxation modulus at 220°C.
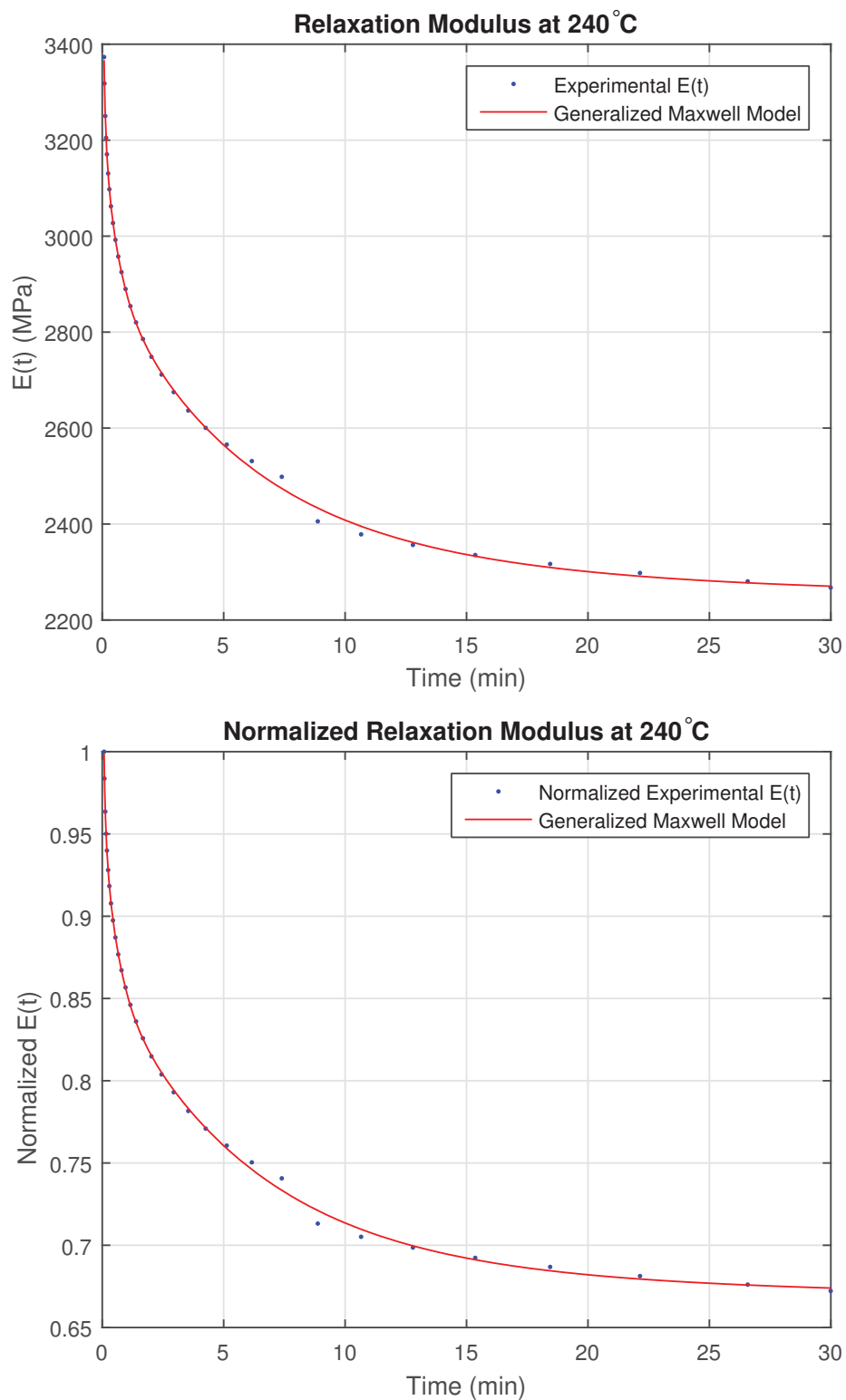
Figure A.25.: Relaxation modulus at 240°C.
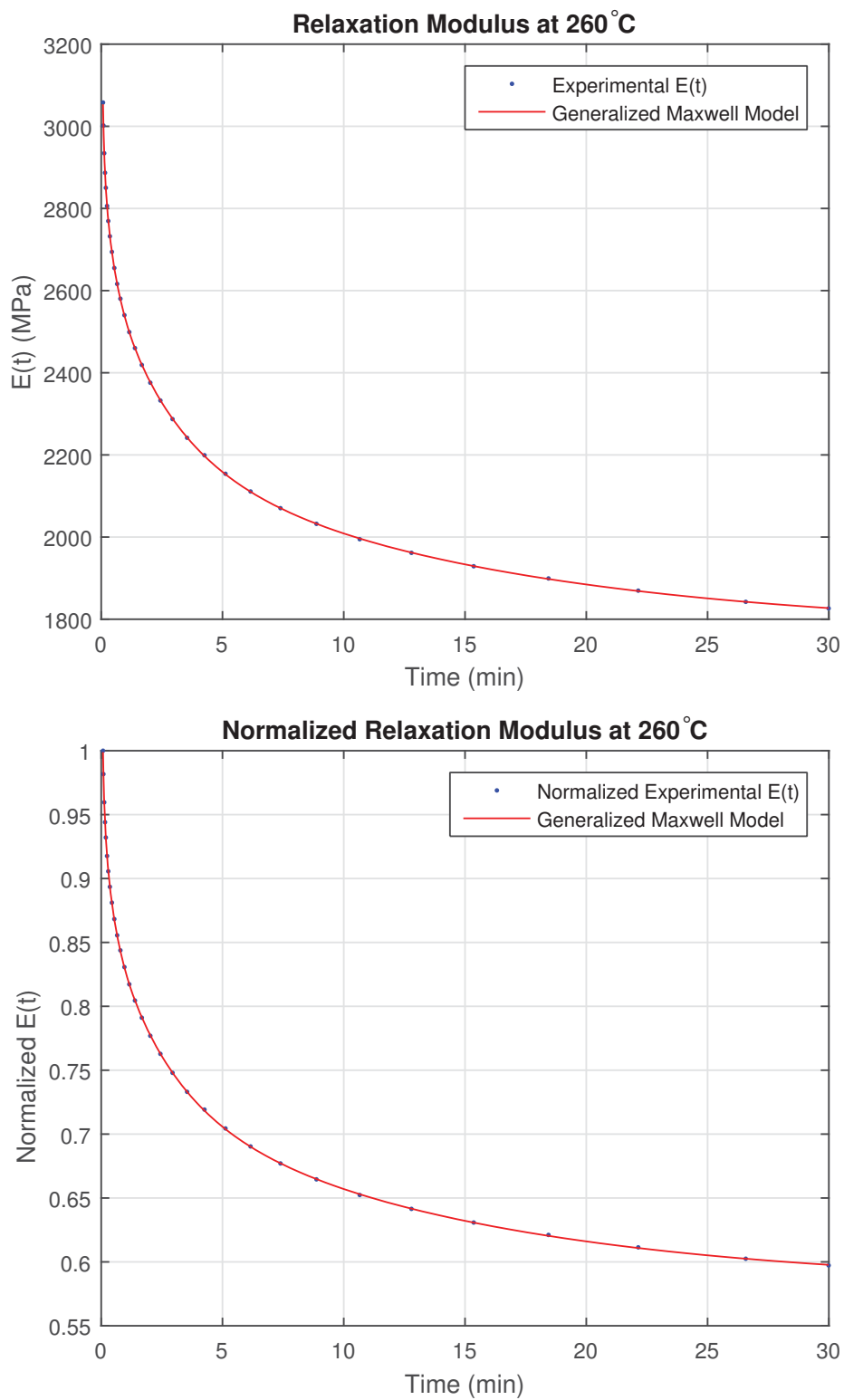
Figure A.26.: Relaxation modulus at 260°C.
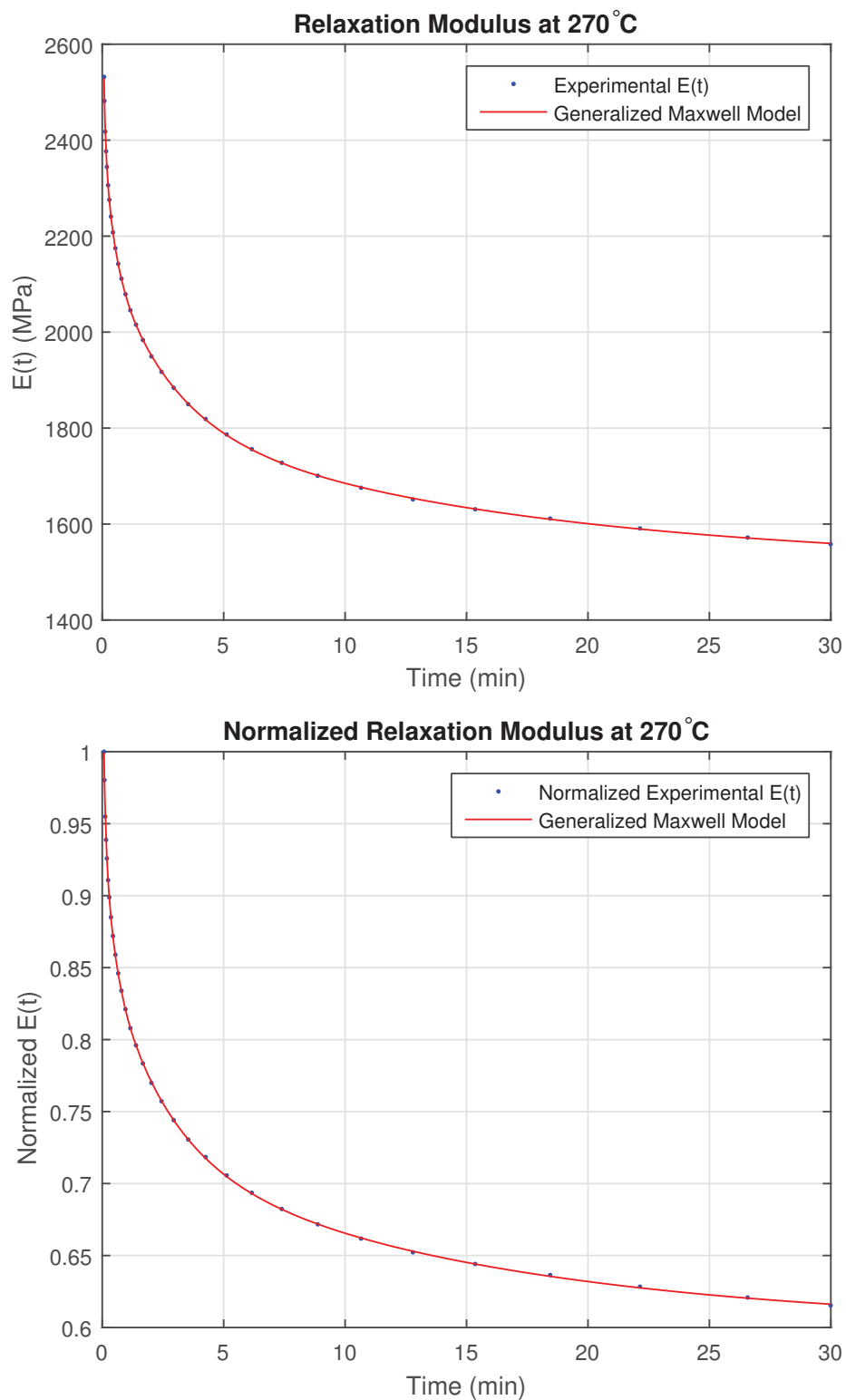
Figure A.27.: Relaxation modulus at 270°C.
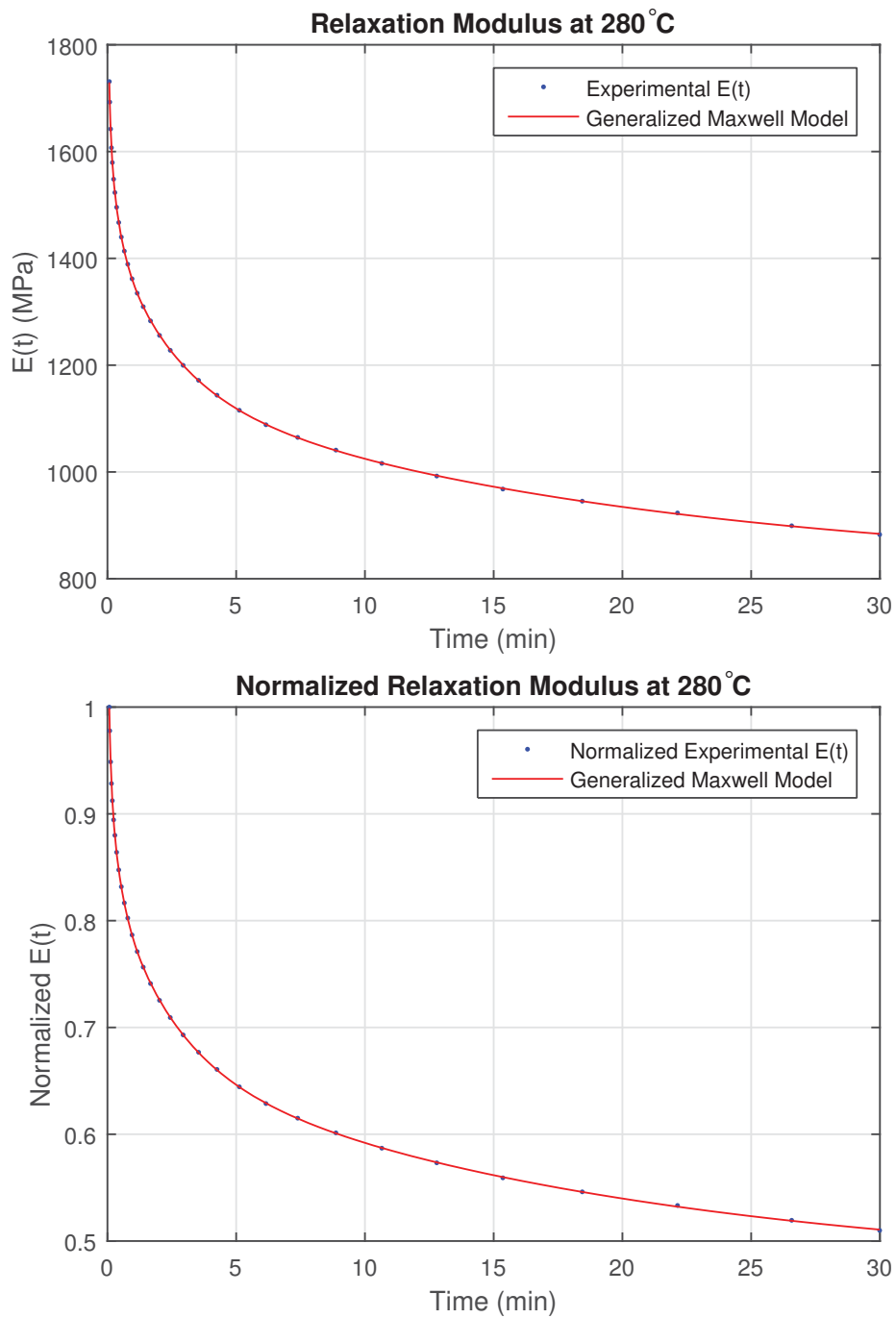
Figure A.28.: Relaxation modulus at 280°C.
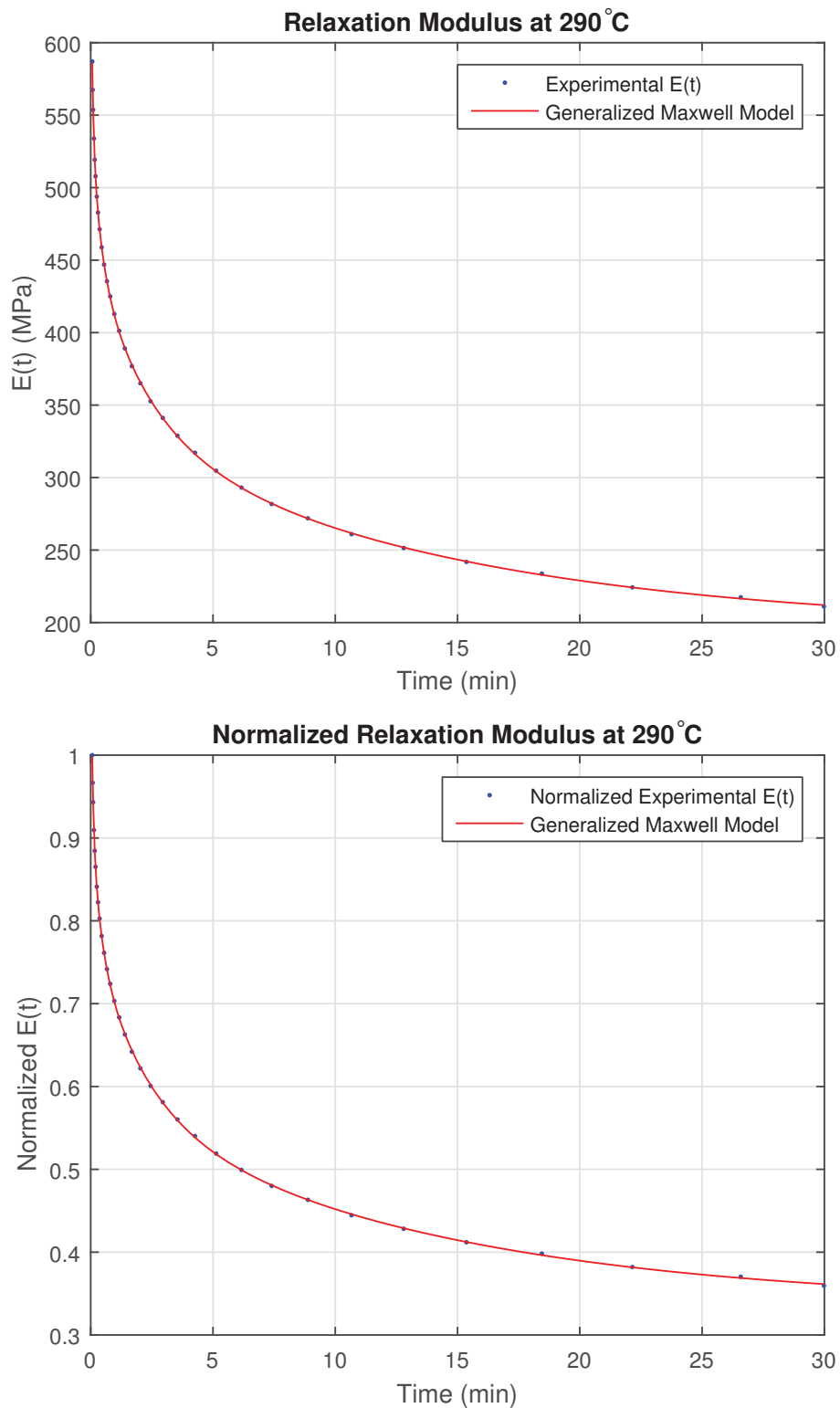
Figure A.29.: Relaxation modulus at 290°C.

A.3.2 Fitting Parameters

50C

E(t)

```
    General model:
    ans(x) = r+E*exp(-(x/t))+E_2*exp(-(x/t_2))+E_3*exp(-(x/t_3))
    +E_4*exp(-(x/t_4))
    Coefficients (with 95% confidence bounds):
      E =         294.8  (148.3, 441.4)
      E_2 =        48.63  (42.9, 54.36)
      E_3 =           36  (22.18, 49.82)
      E_4 =        55.67  (49.01, 62.32)
      r =    1.247e+04   (1.245e+04, 1.248e+04)
      t =       0.03844  (0.02858, 0.04831)
      t_2 =        1.682  (1.324, 2.04)
      t_3 =        31.34  (4.745, 57.93)
      t_4 =       0.2962  (0.2206, 0.3718)
```

Normalized E(t)

```
    General model:
    ans(x) = r+E*exp(-(x/t))+E_2*exp(-(x/t_2))+E_3*exp(-(x/t_3))
    Coefficients (with 95% confidence bounds):
      E =     0.002664  (0.002403, 0.002924)
      E_2 =    0.005377  (0.004971, 0.005782)
      E_3 =     0.01041  (0.008095, 0.01273)
      r =         0.989  (fixed at bound)
      t =         16.87  (14.09, 19.66)
```

```
t_2 =          1.03   (0.8681, 1.192)

t_3 =        0.0846   (0.06566, 0.1035)
```

70C

E(t)

```
    General model:
    ans(x) = r+E*exp(-(x/t))+E_2*exp(-(x/t_2))+E_3*exp(-(x/t_3))
    +E_4*exp(-(x/t_4))
    Coefficients (with 95% confidence bounds):
      E =     1.22e+04
      E_2 =      0.09236
      E_3 =        196.4
      E_4 =        360.8
      r =     1.162e+04
      t =      0.01629
      t_2 =      0.00567
      t_3 =       0.6037   (0.4549, 0.7524)
      t_4 =        9.759   (8.374, 11.14)
```

Normalized E(t)

```
    General model:
    ans(x) = r+E*exp(-(x/t))+E_2*exp(-(x/t_2))+E_3*exp(-(x/t_3))
    +E_4*exp(-(x/t_4))
    Coefficients (with 95% confidence bounds):
      E =      0.03534
      E_2 =      0.01431
```

```
E_3 =       0.02882

E_4 =       0.001969

r =         0.952

t =       0.05197

t_2 =       0.7951

t_3 =         10.07

t_4 =     0.003685
```

80C

E(t)

```
General model:

ans(x) = r+E*exp(-(x/t))+E_2*exp(-(x/t_2))+E_3*exp(-(x/t_3))

+E_4*exp(-(x/t_4))

Coefficients (with 95% confidence bounds):

  E =          1059  (-3.106e+07, 3.106e+07)

  E_2 =        357.3  (314.4, 400.1)

  E_3 =        617.2  (167.1, 1067)

  E_4 =        393.9  (350.5, 437.4)

  r =          9781  (-3.105e+07, 3.107e+07)

  t =     3.761e+06  (-1.03e+11, 1.031e+11)

  t_2 =        1.561  (1.251, 1.872)

  t_3 =        14.98  (3.381, 26.59)

  t_4 =       0.1493  (0.1213, 0.1772)
```

Normalized E(t)

```
General model:
```

ans(x) = r+E*exp(-(x/t))+E_2*exp(-(x/t_2))+E_3*exp(-(x/t_3))

+E_4*exp(-(x/t_4))

Coefficients (with 95% confidence bounds):

E =   0.03581

E_2 =   0.8254

E_3 =   0.0594

E_4 =   0.9961

r =   0.91   (0.9063, 0.9137)

t =   0.514   (0.3165, 0.7115)

t_2 =   0.005001   (-2.963e+20, 2.963e+20)

t_3 =   9.969   (8.051, 11.89)

t_4 =   0.004636   (-1.482e+21, 1.482e+21)

90C

E(t)

General model:

ans(x) = r+E*exp(-(x/t))+E_2*exp(-(x/t_2))+E_3*exp(-(x/t_3))

+E_4*exp(-(x/t_4))

Coefficients (with 95% confidence bounds):

E =   722.4   (707.9, 736.9)

E_2 =   448.7   (423.4, 474)

E_3 =   781.1   (700.5, 861.6)

E_4 =   515.3   (491.5, 539.1)

r =   9827   (9800, 9855)

t =   17.34   (15.31, 19.37)

t_2 =   0.3829   (0.3348, 0.4311)

t_3 =   0.05966   (0.05213, 0.06719)

```
    t_4 =         2.242  (1.984, 2.5)
```

Normalized E(t)

    General model:

    ans(x) = r+E*exp(-(x/t))+E_2*exp(-(x/t_2))+E_3*exp(-(x/t_3))

    +E_4*exp(-(x/t_4))

    Coefficients (with 95% confidence bounds):

     E =   0.06505 (0.06304, 0.06706)

     E_2 =   0.08489 (0.04426, 0.1255)

     E_3 =   0.03923 (0.03442, 0.04404)

     E_4 =   0.0446 (0.04146, 0.04774)

     r =   0.853 (0.8512, 0.8549)

     t =   13.08 (11.71, 14.45)

     t_2 =   0.04213 (0.02704, 0.05723)

     t_3 =   0.2637 (0.201, 0.3264)

     t_4 =   1.609 (1.356, 1.861)

95C

E(t)

    General model:

    ans(x) = r+E*exp(-(x/t))+E_2*exp(-(x/t_2))+E_3*exp(-(x/t_3))

    +E_4*exp(-(x/t_4))

    Coefficients (with 95% confidence bounds):

     E =   745.9 (727.2, 764.7)

     E_2 =   1394 (1176, 1611)

     E_3 =   563.3 (532.6, 594)

     E_4 =   590.2 (562, 618.4)
```

```
    r =           8897  (8860, 8933)

    t =          17.69  (15.04, 20.35)

    t_2 =      0.05154  (0.04517, 0.0579)

    t_3 =        2.401  (2.106, 2.696)

    t_4 =       0.3611  (0.3235, 0.3986)
```

Normalized E(t)


```
    General model:
    ans(x) = r+E*exp(-(x/t))+E_2*exp(-(x/t_2))+E_3*exp(-(x/t_3))
    +E_4*exp(-(x/t_4))
    Coefficients (with 95% confidence bounds):
      E =       0.1297  (0.1089, 0.1504)

      E_2 =    0.06888  (0.06713, 0.07063)

      E_3 =    0.05165  (0.04889, 0.0544)

      E_4 =    0.05434  (0.05172, 0.05696)

      r =         0.82  (0.8168, 0.8231)

      t =      0.05101  (0.04463, 0.05738)

      t_2 =      17.31  (14.84, 19.78)

      t_3 =      2.357  (2.069, 2.644)

      t_4 =     0.3565  (0.3191, 0.3938)
```


100C

E(t)


```
    General model:
    ans(x) = r+E*exp(-(x/t))+E_2*exp(-(x/t_2))+E_3*exp(-(x/t_3))
    +E_4*exp(-(x/t_4))
```

```
Coefficients (with 95% confidence bounds):
  E =          1203  (1078, 1327)
  E_2 =        527.3  (480.2, 574.4)
  E_3 =        681.4  (651.7, 711)
  E_4 =        509.4  (469.4, 549.4)
  r =          8000  (7943, 8057)
  t =      0.06447  (0.05673, 0.0722)
  t_2 =        2.584  (2.037, 3.132)
  t_3 =        18.21  (13.53, 22.89)
  t_4 =      0.4489  (0.3726, 0.5252)
```

Normalized E(t)

```
General model:
ans(x) = r+E*exp(-(x/t))+E_2*exp(-(x/t_2))+E_3*exp(-(x/t_3))
+E_4*exp(-(x/t_4))
Coefficients (with 95% confidence bounds):
  E =        0.1256  (0.1109, 0.1403)
  E_2 =      0.05251  (0.04874, 0.05628)
  E_3 =      0.04984  (0.04581, 0.05388)
  E_4 =      0.07119  (0.06836, 0.07403)
  r =        0.812  (0.8089, 0.8151)
  t =      0.06011  (0.05229, 0.06793)
  t_2 =        2.144  (1.764, 2.524)
  t_3 =      0.3869  (0.3173, 0.4565)
  t_4 =        15.26  (12.93, 17.59)
```

105C

E(t)

    General model:

    ans(x) = r+E*exp(-(x/t))+E_2*exp(-(x/t_2))+E_3*exp(-(x/t_3))

    +E_4*exp(-(x/t_4))

    Coefficients (with 95% confidence bounds):

      E =   526.6 (463.7, 589.5)

      E_2 =   734.9 (696.7, 773)

      E_3 =   494.3 (407.5, 581.1)

      E_4 =   1000 (fixed at bound)

      r =   7400 (fixed at bound)

      t =   1.994 (1.593, 2.395)

      t_2 =   14.61 (13.85, 15.37)

      t_3 =   0.3514 (0.2278, 0.4749)

      t_4 = 0.06923 (0.05383, 0.08463)

Normalized E(t)

    General model:

    ans(x) = r+E*exp(-(x/t))+E_2*exp(-(x/t_2))+E_3*exp(-(x/t_3))

    +E_4*exp(-(x/t_4))

    Coefficients (with 95% confidence bounds):

      E =   0.07828

      E_2 =   0.9543

      E_3 =   0.06917

      E_4 =   0.1061

      r =   0.7947

      t =   14.51

      t_2 = 3.28e-05

```
      t_3 =         1.726  (1.169, 2.283)

      t_4 =        0.1448  (0.1168, 0.1728)
```

110C

E(t)

    General model:

    ans(x) = r+E*exp(-(x/t))+E_2*exp(-(x/t_2))+E_3*exp(-(x/t_3))

    +E_4*exp(-(x/t_4))

    Coefficients (with 95% confidence bounds):

```
      E =           510.8  (482.9, 538.6)

      E_2 =         535.4  (502.3, 568.5)

      E_3 =          1325  (1128, 1522)

      E_4 =         732.2  (711.7, 752.8)

      r =            7177  (7152, 7202)

      t =           2.036  (1.766, 2.306)

      t_2 =        0.3223  (0.2798, 0.3648)

      t_3 =       0.04902  (0.04246, 0.05557)

      t_4 =         15.14  (13.39, 16.89)
```


Normalized E(t)

    General model:

    ans(x) = r+E*exp(-(x/t))+E_2*exp(-(x/t_2))+E_3*exp(-(x/t_3))

    +E_4*exp(-(x/t_4))

    Coefficients (with 95% confidence bounds):

```
      E =         0.05874  (0.05352, 0.06397)

      E_2 =       0.05526  (0.05161, 0.05891)
```

```
E_3 =      0.08359   (0.08096, 0.08621)

E_4 =       0.1579   (0.1207, 0.1951)

r  =        0.7975   (0.7954, 0.7996)

t  =        0.2784   (0.2286, 0.3281)

t_2 =         1.679  (1.425, 1.933)

t_3 =         12.82  (11.59, 14.05)

t_4 =       0.0446   (0.03604, 0.05316)
```

115C

E(t)

```
    General model:

    ans(x) = r+E*exp(-(x/t))+E_2*exp(-(x/t_2))+E_3*exp(-(x/t_3))

    +E_4*exp(-(x/t_4))

    Coefficients (with 95% confidence bounds):

     E =          644   (538.3, 749.6)

     E_2 =        531.5  (471.2, 591.9)

     E_3 =         1064  (937, 1191)

     E_4 =        523.7  (489.5, 558)

     r =          6868  (6682, 7054)

     t =         29.05  (11.21, 46.89)

     t_2 =        3.119  (2.46, 3.778)

     t_3 =      0.06104  (0.05271, 0.06937)

     t_4 =       0.4347  (0.371, 0.4984)
```

Normalized E(t)

```
    General model:
```

```
ans(x) = r+E*exp(-(x/t))+E_2*exp(-(x/t_2))+E_3*exp(-(x/t_3))
+E_4*exp(-(x/t_4))
```

Coefficients (with 95% confidence bounds):

```
  E =       0.07151  (0.06929, 0.07373)
  E_2 =        0.124  (0.1095, 0.1384)
  E_3 =      0.05695  (0.05296, 0.06095)
  E_4 =      0.05856  (0.0549, 0.06222)
  r =         0.7987  (0.7929, 0.8044)
  t =          19.22  (14.82, 23.61)
  t_2 =      0.05712  (0.04973, 0.06452)
  t_3 =        2.473  (2.076, 2.871)
  t_4 =       0.3763  (0.3248, 0.4279)
```

120C

E(t)

General model:

```
ans(x) = r+E*exp(-(x/t))+E_2*exp(-(x/t_2))+E_3*exp(-(x/t_3))
+E_4*exp(-(x/t_4))
```

Coefficients (with 95% confidence bounds):

```
  E =        653.4  (624.8, 682)
  E_2 =       1232  (1064, 1399)
  E_3 =      453.6  (425.1, 482.2)
  E_4 =      427.1  (400.6, 453.7)
  r =         6587  (6574, 6600)
  t =        12.06  (10.95, 13.18)
  t_2 =    0.05039  (0.04423, 0.05656)
  t_3 =      0.326  (0.2818, 0.3702)
  t_4 =      2.003  (1.71, 2.295)
```

Normalized E(t)

```
General model:
ans(x) = r+E*exp(-(x/t))+E_2*exp(-(x/t_2))+E_3*exp(-(x/t_3))
+E_4*exp(-(x/t_4))
Coefficients (with 95% confidence bounds):
  E =        0.1538   (0.1309, 0.1766)
  E_2 =      0.05553  (0.05191, 0.05914)
  E_3 =      0.05207  (0.04895, 0.0552)
  E_4 =      0.0804   (0.07709, 0.08372)
  r =        0.8031   (0.8015, 0.8046)
  t =        0.04895  (0.04264, 0.05526)
  t_2 =      0.3136   (0.2703, 0.3568)
  t_3 =      1.929    (1.654, 2.203)
  t_4 =      11.83    (10.81, 12.86)
```

125C

E(t)

```
General model:
ans(x) = r+E*exp(-(x/t))+E_2*exp(-(x/t_2))+E_3*exp(-(x/t_3))
+E_4*exp(-(x/t_4))
Coefficients (with 95% confidence bounds):
  E =        459.8  (443.3, 476.3)
  E_2 =      379.8  (350.9, 408.8)
  E_3 =      1092   (936.6, 1248)
  E_4 =      415.6  (388.7, 442.5)
```

```
  r =          6050   (6008, 6092)

  t =         19.11   (14.12, 24.1)

  t_2 =        2.393  (1.964, 2.821)

  t_3 =      0.05136  (0.04469, 0.05803)

  t_4 =       0.3658  (0.3132, 0.4184)
```

Normalized E(t)


```
   General model:
   ans(x) = r+E*exp(-(x/t))+E_2*exp(-(x/t_2))+E_3*exp(-(x/t_3))
   +E_4*exp(-(x/t_4))
   Coefficients (with 95% confidence bounds):
    E =       0.0507   (0.04748, 0.05391)

    E_2 =      0.1582   (0.1304, 0.186)

    E_3 =      0.0559   (0.052, 0.0598)

    E_4 =     0.06337   (0.06125, 0.06549)

    r =       0.8196   (0.8165, 0.8228)

    t =        2.006   (1.695, 2.318)

    t_2 =     0.04673   (0.03995, 0.05352)

    t_3 =      0.3163   (0.2691, 0.3635)

    t_4 =       15.82   (13.24, 18.39)
```


130C

E(t)


```
   General model:
   ans(x) = r+E*exp(-(x/t))+E_2*exp(-(x/t_2))+E_3*exp(-(x/t_3))
   +E_4*exp(-(x/t_4))
```

```
Coefficients (with 95% confidence bounds):
  E =        438.5  (365.4, 511.5)
  E_2 =       537.1  (480.8, 593.3)
  E_3 =       384.3  (359.3, 409.4)
  E_4 =        1129  (940.4, 1317)
  r =         5335  (5297, 5374)
  t =        3.059  (2.421, 3.697)
  t_2 =       15.76  (11.31, 20.21)
  t_3 =      0.3734  (0.3213, 0.4256)
  t_4 =     0.05037  (0.04353, 0.05721)
```

Normalized E(t)

```
  General model:
  ans(x) = r+E*exp(-(x/t))+E_2*exp(-(x/t_2))+E_3*exp(-(x/t_3))
  +E_4*exp(-(x/t_4))
  Coefficients (with 95% confidence bounds):
  E =     0.07663  (0.06949, 0.08377)
  E_2 =    0.06882  (0.05708, 0.08057)
  E_3 =    0.05711  (0.05351, 0.06072)
  E_4 =     0.1663  (0.1383, 0.1943)
  r =      0.7824  (0.7743, 0.7904)
  t =       17.86  (11.41, 24.32)
  t_2 =     3.273  (2.609, 3.937)
  t_3 =      0.38  (0.3288, 0.4312)
  t_4 =   0.05039  (0.04355, 0.05722)
```

135C

E(t)

General model:

ans(x) = r+E*exp(-(x/t))+E_2*exp(-(x/t_2))+E_3*exp(-(x/t_3))

+E_4*exp(-(x/t_4))

Coefficients (with 95% confidence bounds):

E =   1149   (837.4, 1461)

E_2 =   400.1 (385.1, 415.1)

E_3 =   359.8 (331.9, 387.8)

E_4 =   318.6 (298.4, 338.8)

r =   5359   (5342, 5375)

t =   0.0375   (0.03068, 0.04433)

t_2 =   14.06 (12.04, 16.07)

t_3 =   0.2614 (0.2211, 0.3018)

t_4 =   1.79 (1.517, 2.063)

Normalized E(t)

General model:

ans(x) = r+E*exp(-(x/t))+E_2*exp(-(x/t_2))+E_3*exp(-(x/t_3))

+E_4*exp(-(x/t_4))

Coefficients (with 95% confidence bounds):

E =   0.1767 (0.1147, 0.2387)

E_2 =   0.04767 (0.04394, 0.05139)

E_3 =   0.06368 (0.06093, 0.06644)

E_4 =   0.05431 (0.04853, 0.0601)

r =   0.8297 (0.8277, 0.8316)

t =   0.03657 (0.02795, 0.04518)

t_2 =   1.521 (1.25, 1.792)

```
t_3 =        11.89  (10.44, 13.33)

t_4 =        0.2385  (0.1897, 0.2872)
```

145C

E(t)

```
    General model:
    ans(x) = r+E*exp(-(x/t))+E_2*exp(-(x/t_2))+E_3*exp(-(x/t_3))
    +E_4*exp(-(x/t_4))
    Coefficients (with 95% confidence bounds):
      E =        351.3

      E_2 =        589.4

      E_3 =        440.6

      E_4 =        0.9961

      r =        4921

      t =        1.004

      t_2 =      0.09041

      t_3 =        10.65

      t_4 =     0.004634
```

Normalized E(t)

```
    General model:
    ans(x) = r+E*exp(-(x/t))+E_2*exp(-(x/t_2))+E_3*exp(-(x/t_3))
    +E_4*exp(-(x/t_4))
    Coefficients (with 95% confidence bounds):
      E =      0.04914  (0.04519, 0.05309)

      E_2 =      0.04914  (0.04635, 0.05194)
```

```
E_3 =        0.1528   (0.1195, 0.1861)

E_4 =        0.06751  (0.06538, 0.06965)

r =          0.8283   (0.8264, 0.8301)

t =          0.2805   (0.2351, 0.3259)

t_2 =         1.765   (1.526, 2.005)

t_3 =        0.04317  (0.03605, 0.05029)

t_4 =         13.32   (11.95, 14.69)
```

155C

E(t)

```
General model:

ans(x) = r+E*exp(-(x/t))+E_2*exp(-(x/t_2))+E_3*exp(-(x/t_3))

+E_4*exp(-(x/t_4))

Coefficients (with 95% confidence bounds):

  E =        504.5   (485.6, 523.5)

  E_2 =        332    (310.2, 353.8)

  E_3 =      810.1    (668.7, 951.4)

  E_4 =      398.6    (367.3, 429.8)

  r =        4532     (4499, 4565)

  t =        17.48    (13.89, 21.07)

  t_2 =      0.3447   (0.2951, 0.3943)

  t_3 =      0.04664  (0.03948, 0.0538)

  t_4 =       2.515   (2.132, 2.898)
```

Normalized E(t)

```
General model:
```

```
ans(x) = r+E*exp(-(x/t))+E_2*exp(-(x/t_2))+E_3*exp(-(x/t_3))
+E_4*exp(-(x/t_4))
Coefficients (with 95% confidence bounds):
  E =      0.06761  (0.06272, 0.07251)
  E_2 =     0.05716  (0.05352, 0.0608)
  E_3 =      0.1455  (0.1182, 0.1728)
  E_4 =     0.08689  (0.08372, 0.09007)
  r =        0.776  (0.7711, 0.7809)
  t =        2.429  (2.08, 2.777)
  t_2 =      0.3316  (0.2857, 0.3775)
  t_3 =     0.04451  (0.03766, 0.05137)
  t_4 =       16.83  (13.78, 19.89)
```

165C

E(t)

```
General model:
ans(x) = r+E*exp(-(x/t))+E_2*exp(-(x/t_2))+E_3*exp(-(x/t_3))
+E_4*exp(-(x/t_4))
Coefficients (with 95% confidence bounds):
  E =        342.5  (320.2, 364.9)
  E_2 =       922.1  (703.1, 1141)
  E_3 =       401.1  (365, 437.3)
  E_4 =       600.4  (571.8, 628.9)
  r =         4017  (3991, 4043)
  t =       0.3278  (0.2807, 0.3749)
  t_2 =     0.04155  (0.03436, 0.04874)
  t_3 =       2.455  (2.057, 2.853)
```

```
    t_4 =          15.2  (12.78, 17.62)
```

Normalized E(t)


```
    General model:
    ans(x) = r+E*exp(-(x/t))+E_2*exp(-(x/t_2))+E_3*exp(-(x/t_3))
    +E_4*exp(-(x/t_4))
    Coefficients (with 95% confidence bounds):
     E =       0.1789  (0.1317, 0.2261)
     E_2 =      0.06345  (0.05925, 0.06766)
     E_3 =      0.07324  (0.06704, 0.07944)
     E_4 =       0.1119  (0.1068, 0.117)
     r =       0.7416  (0.7372, 0.746)
     t =      0.03974  (0.03254, 0.04694)
     t_2 =        0.314  (0.2687, 0.3592)
     t_3 =        2.356  (1.984, 2.727)
     t_4 =        14.73  (12.59, 16.88)
```


175C

E(t)


```
    General model:
    ans(x) = r+E*exp(-(x/t))+E_2*exp(-(x/t_2))+E_3*exp(-(x/t_3))
    +E_4*exp(-(x/t_4))
    Coefficients (with 95% confidence bounds):
     E =       530.2  (512.5, 547.8)
     E_2 =      366.5  (343.4, 389.6)
     E_3 =      346.4  (325.2, 367.6)
```

```
E_4 =          660.9  (594.8, 727)

r =             3839  (3817, 3861)

t =            15.94  (13.73, 18.16)

t_2 =          2.308  (1.968, 2.648)

t_3 =         0.3708  (0.3202, 0.4215)

t_4 =        0.05623  (0.04912, 0.06333)
```

Normalized E(t)

```
    General model:
    ans(x) = r+E*exp(-(x/t))+E_2*exp(-(x/t_2))+E_3*exp(-(x/t_3))
    +E_4*exp(-(x/t_4))
    Coefficients (with 95% confidence bounds):
      E =      0.06991  (0.06575, 0.07408)

      E_2 =     0.1294  (0.1142, 0.1445)

      E_3 =     0.1048  (0.1015, 0.1081)

      E_4 =     0.0655  (0.06091, 0.07009)

      r =       0.7442  (0.7409, 0.7475)

      t =        2.061  (1.761, 2.361)

      t_2 =    0.05397  (0.04619, 0.06175)

      t_3 =      14.63  (12.96, 16.29)

      t_4 =     0.3417  (0.289, 0.3944)
```

180C

E(t)

```
    General model:
    ans(x) = r+E*exp(-(x/t))+E_2*exp(-(x/t_2))+E_3*exp(-(x/t_3))
```

```
+E_4*exp(-(x/t_4))
```

Coefficients (with 95% confidence bounds):

```
  E =        705.2  (600.8, 809.6)
  E_2 =        464.1  (425, 503.1)
  E_3 =        327.8  (306, 349.5)
  E_4 =        512.5  (476.3, 548.8)
  r =          3500  (3480, 3520)
  t =       0.05305  (0.04512, 0.06097)
  t_2 =        2.598  (2.245, 2.951)
  t_3 =       0.3564  (0.3061, 0.4068)
  t_4 =        13.93  (11.65, 16.2)
```

Normalized E(t)

General model:

```
ans(x) = r+E*exp(-(x/t))+E_2*exp(-(x/t_2))+E_3*exp(-(x/t_3))
+E_4*exp(-(x/t_4))
```

Coefficients (with 95% confidence bounds):

```
  E =       0.1527  (0.1209, 0.1844)
  E_2 =      0.06696  (0.06129, 0.07264)
  E_3 =      0.08741  (0.08037, 0.09446)
  E_4 =       0.1138  (0.1061, 0.1216)
  r =       0.7235  (0.7207, 0.7264)
  t =      0.04885  (0.03944, 0.05825)
  t_2 =       0.3148  (0.2606, 0.3689)
  t_3 =         2.21  (1.877, 2.542)
  t_4 =        11.67  (10.24, 13.09)
```

200C

E(t)

    General model:

    ans(x) = r+E*exp(-(x/t))+E_2*exp(-(x/t_2))+E_3*exp(-(x/t_3))

    +E_4*exp(-(x/t_4))

    Coefficients (with 95% confidence bounds):

      E =   356.9 (320.4, 393.4)

      E_2 =   556.9 (522.9, 590.9)

      E_3 =   458.6 (426.4, 490.8)

      E_4 =   860.9 (631.8, 1090)

      r =   3641 (3625, 3657)

      t =   0.2813 (0.2247, 0.338)

      t_2 =   11.85 (10.31, 13.4)

      t_3 =   1.956 (1.654, 2.258)

      t_4 =   0.04379 (0.03362, 0.05396)

Normalized E(t)

    General model:

    ans(x) = r+E*exp(-(x/t))+E_2*exp(-(x/t_2))+E_3*exp(-(x/t_3))

    +E_4*exp(-(x/t_4))

    Coefficients (with 95% confidence bounds):

      E =   0.0725 (0.06433, 0.08067)

      E_2 =   0.08952 (0.08378, 0.09526)

      E_3 =   0.1139 (0.1078, 0.12)

      E_4 =   0.192 (0.1204, 0.2636)

      r =   0.7212 (0.7186, 0.7238)

      t =   0.2468 (0.1967, 0.2969)

```
      t_2 =          1.77  (1.514, 2.027)

      t_3 =         11.04  (9.84, 12.24)

      t_4 =       0.03866  (0.02815, 0.04916)
```

220C

E(t)

```
    General model:
    ans(x) = r+E*exp(-(x/t))+E_2*exp(-(x/t_2))+E_3*exp(-(x/t_3))
    +E_4*exp(-(x/t_4))
    Coefficients (with 95% confidence bounds):
      E =           437  (378.1, 495.9)

      E_2 =         500   (fixed at bound)

      E_3 =       310.7  (278.6, 342.9)

      E_4 =       400.7  (354.3, 447)

      r =          3081  (3040, 3123)

      t =         2.762  (2.132, 3.392)

      t_2 =     0.06643  (0.05499, 0.07787)

      t_3 =      0.3911  (0.2977, 0.4844)

      t_4 =       16.04  (9.935, 22.15)
```

Normalized E(t)

```
    General model:
    ans(x) = r+E*exp(-(x/t))+E_2*exp(-(x/t_2))+E_3*exp(-(x/t_3))
    +E_4*exp(-(x/t_4))
    Coefficients (with 95% confidence bounds):
      E =        0.1051  (0.09483, 0.1154)
```

```
E_2 =      0.07776  (0.07311, 0.08241)

E_3 =       0.1534  (0.1301, 0.1767)

E_4 =      0.09059  (0.08462, 0.09656)

r =         0.7087  (0.6995, 0.718)

t =          2.902  (2.463, 3.341)

t_2 =       0.3792  (0.3289, 0.4296)

t_3 =      0.05125  (0.04346, 0.05904)

t_4 =        18.03  (12.1, 23.96)
```

240C

E(t)

```
General model:
ans(x) = r+E*exp(-(x/t))+E_2*exp(-(x/t_2))+E_3*exp(-(x/t_3))
+E_4*exp(-(x/t_4))
Coefficients (with 95% confidence bounds):
  E =           500  (fixed at bound)
  E_2 =          500  (-2324, 3324)
  E_3 =        177.7  (-2499, 2855)
  E_4 =        334.3  (257.1, 411.4)
  r =           2250  (2007, 2493)
  t =        0.06638  (0.04496, 0.0878)
  t_2 =        5.233  (-8.524, 18.99)
  t_3 =        13.39  (-138.4, 165.2)
  t_4 =        0.539  (0.2595, 0.8185)
```

Normalized E(t)

```
General model:
ans(x) = r+E*exp(-(x/t))+E_2*exp(-(x/t_2))+E_3*exp(-(x/t_3))
+E_4*exp(-(x/t_4))
Coefficients (with 95% confidence bounds):
  E =      0.03164  (-4.023, 4.087)
  E_2 =      0.1604  (0.08662, 0.2342)
  E_3 =      0.1024  (0.08281, 0.1219)
  E_4 =      0.1845  (-0.06162, 0.4306)
  r =       0.6498  (-3.667, 4.967)
  t =        92.97  (-1.713e+04, 1.731e+04)
  t_2 =     0.06176  (0.02901, 0.0945)
  t_3 =      0.5439  (0.3063, 0.7815)
  t_4 =       6.055  (-0.5801, 12.69)
```

260C

E(t)

```
General model:
ans(x) = r+E*exp(-(x/t))+E_2*exp(-(x/t_2))+E_3*exp(-(x/t_3))
+E_4*exp(-(x/t_4))
Coefficients (with 95% confidence bounds):
  E =          500  (fixed at bound)
  E_2 =       293.3  (274.3, 312.3)
  E_3 =       464.8  (433.8, 495.7)
  E_4 =       454.5  (422.3, 486.7)
  r =         1771  (1752, 1790)
  t =       0.05833  (0.05286, 0.0638)
  t_2 =      0.3828  (0.3231, 0.4425)
```

```
      t_3 =          14.19   (11.79, 16.59)

      t_4 =          2.487   (2.147, 2.828)
```

Normalized E(t)


```
      General model:
      ans(x) = r+E*exp(-(x/t))+E_2*exp(-(x/t_2))+E_3*exp(-(x/t_3))
      +E_4*exp(-(x/t_4))
      Coefficients (with 95% confidence bounds):
        E =      0.09728  (0.09005, 0.1045)

        E_2 =     0.1768  (0.1485, 0.2051)

        E_3 =     0.1465  (0.1369, 0.1561)

        E_4 =      0.157  (0.1473, 0.1668)

        r =      0.5816  (0.5764, 0.5867)

        t =      0.3422  (0.2866, 0.3978)

        t_2 =     0.05157  (0.04224, 0.06091)

        t_3 =      2.303  (2.003, 2.604)

        t_4 =      13.19  (11.31, 15.06)
```


270C

E(t)


```
      General model:
      ans(x) = r+E*exp(-(x/t))+E_2*exp(-(x/t_2))+E_3*exp(-(x/t_3))
      +E_4*exp(-(x/t_4))
      Coefficients (with 95% confidence bounds):
        E =       281.2  (265.6, 296.9)

        E_2 =      312.4  (291.5, 333.3)
```

```
E_3 =             500   (fixed at bound)

E_4 =           365.4  (339.6, 391.2)

r  =            1514  (1494, 1535)

t  =          0.3694  (0.3211, 0.4177)

t_2 =           15.53  (11.91, 19.16)

t_3 =         0.05239  (0.04847, 0.0563)

t_4 =           2.477  (2.131, 2.822)
```

Normalized E(t)

General model:

ans(x) = r+E*exp(-(x/t))+E_2*exp(-(x/t_2))+E_3*exp(-(x/t_3))

+E_4*exp(-(x/t_4))

Coefficients (with 95% confidence bounds):

```
E  =       0.1429  (0.1333, 0.1526)

E_2 =        0.1127  (0.1056, 0.1198)

E_3 =        0.2202  (0.1778, 0.2625)

E_4 =        0.1268  (0.1181, 0.1355)

r  =       0.6007  (0.5943, 0.6072)

t  =        2.317  (2.001, 2.633)

t_2 =        0.3382  (0.2909, 0.3856)

t_3 =       0.04639  (0.03826, 0.05451)

t_4 =        14.26  (11.43, 17.08)
```


280C

E(t)

General model:

```
ans(x) = r+E*exp(-(x/t))+E_2*exp(-(x/t_2))+E_3*exp(-(x/t_3))
+E_4*exp(-(x/t_4))
Coefficients (with 95% confidence bounds):
  E =        297.6  (285.6, 309.6)
  E_2 =         225  (212.6, 237.3)
  E_3 =       355.4  (348.4, 362.3)
  E_4 =       367.6  (327.3, 407.8)
  r =         812.5  (795.5, 829.6)
  t =         2.314  (2.096, 2.533)
  t_2 =      0.3431  (0.3027, 0.3834)
  t_3 =       18.71  (16.15, 21.27)
  t_4 =      0.0534  (0.04604, 0.06075)
```

Normalized E(t)


```
General model:
ans(x) = r+E*exp(-(x/t))+E_2*exp(-(x/t_2))+E_3*exp(-(x/t_3))
+E_4*exp(-(x/t_4))
Coefficients (with 95% confidence bounds):
  E =        0.1304  (0.1232, 0.1376)
  E_2 =      0.2145  (0.1897, 0.2393)
  E_3 =       0.172  (0.1651, 0.1788)
  E_4 =      0.2055  (0.2015, 0.2094)
  r =        0.4702  (0.4606, 0.4797)
  t =        0.3369  (0.2974, 0.3763)
  t_2 =     0.05234  (0.04497, 0.05971)
  t_3 =       2.289  (2.075, 2.502)
  t_4 =       18.48  (16.02, 20.94)
```

290C

E(t)

General model:

ans(x) = r+E*exp(-(x/t))+E_2*exp(-(x/t_2))+E_3*exp(-(x/t_3))

+E_4*exp(-(x/t_4))

Coefficients (with 95% confidence bounds):

  E =   98.05 (89.17, 106.9)

  E_2 =   161.4 (142.3, 180.5)

  E_3 =   140.1 (130.6, 149.6)

  E_4 =   122.9 (113, 132.8)

  r =   196.2 (189.6, 202.8)

  t =   0.3539 (0.2823, 0.4255)

  t_2 =   0.05487 (0.04494, 0.0648)

  t_3 =   13.76 (11.19, 16.33)

  t_4 =   2.175 (1.77, 2.58)

Normalized E(t)

General model:

ans(x) = r+E*exp(-(x/t))+E_2*exp(-(x/t_2))+E_3*exp(-(x/t_3))

+E_4*exp(-(x/t_4))

Coefficients (with 95% confidence bounds):

  E =   0.2821 (0.2413, 0.3229)

  E_2 =   0.2441 (0.2292, 0.2589)

  E_3 =   0.1679 (0.1525, 0.1834)

  E_4 =   0.21 (0.1946, 0.2253)

  r =   0.3368 (0.3273, 0.3464)

```
    t =      0.05065  (0.04052, 0.06077)

    t_2 =       13.08  (10.99, 15.16)

    t_3 =      0.3201  (0.2552, 0.385)

    t_4 =       2.022  (1.676, 2.369)
```

A.4   Isochronal Relaxation Modulus Models

```
6 Second Relaxation Modulus


General model Sin3:
    f(x) =  a1*sin(b1*x+c1) + a2*sin(b2*x+c2) + a3*sin(b3*x+c3)


Coefficients (with 95\% confidence bounds):
    a1 =   2.428e+04  (-2.224e+05, 2.709e+05)

    b1 =    0.002092  (-0.02139, 0.02558)

    c1 =        2.53  (-4.182, 9.242)

    a2 =        1294  (-181.5, 2770)

    b2 =     0.03392  (0.01426, 0.05358)

    c2 =     -0.5733  (-3.927, 2.78)

    a3 =       388.9  (243.7, 534.1)

    b3 =     0.06458  (0.05857, 0.0706)

    c3 =       2.265  (0.903, 3.628)
Goodness of fit:
  SSE: 9.412e+05

  R-square: 0.9971

  Adjusted R-square: 0.9957

  RMSE: 235.3


Normalized 6 Second Relaxation Modulus
```

```
General model Sin3:
    f(x) =  a1*sin(b1*x+c1) + a2*sin(b2*x+c2) + a3*sin(b3*x+c3)
Coefficients (with 95\% confidence bounds):
       a1 =        1.019  (-1.21, 3.249)
       b1 =     0.004526  (-0.01167, 0.02072)
       c1 =        1.865  (-2.338, 6.067)
       a2 =       0.1212  (-0.0989, 0.3413)
       b2 =      0.03105  (0.007841, 0.05425)
       c2 =     -0.08403  (-4.051, 3.883)
       a3 =      0.03032  (0.01838, 0.04227)
       b3 =      0.06461  (0.05876, 0.07047)
       c3 =        2.157  (0.9183, 3.396)
Goodness of fit:
  SSE: 0.005675
  R-square: 0.997
  Adjusted R-square: 0.9956
  RMSE: 0.01827
```

A.5   MATLAB Code

A.5.1   Isothermal Stress Relaxation Models, Surface Plots, and Non Isothermal Model

```
%%
clc, clear all, format long, format compact, close all

%%
% sheet, temp, rowend
filename = 'SRdata2.xlsx';
input = [ 2,  50 , 79;
```

```
           3,   70 , 80;
           4,   80 , 79;
           5,   90 , 80;
           6,   95 , 80;
           7,   100, 80;
           8,   105, 80;
           9,   110, 80;
          10,   115, 80;
          11,   120, 80;
          12,   125, 80;
          13,   130, 80;
          14,   135, 81;
          15,   145, 80;
          16,   155, 81;
          17,   165, 81;
          18,   175, 81;
          19,   180, 80;
          20,   200, 81;
          21,   220, 81;
          22,   240, 81;
          23,   260, 81;
          24,   270, 81;
          25,   280, 81;
          26,   290, 82];
timstr = @(x) sprintf('D50:D%02d',x);
modstr = @(x) sprintf('C50:C%02d',x);
N = 25;


%% Read in all data
```

```matlab
for i = 1:N
    data(i).T = input(i,2);
    data(i).time = xlsread(filename, input(i,1), timstr(input(i,3)));
    data(i).mod  = xlsread(filename, input(i,1), modstr(input(i,3)));
    data(i).nmod = data(i).mod / data(i).mod(1,1);
end


%% Fit all data
for i = 1:N
    fn = str2func(sprintf('fit%d', data(i).T));
    data(i).mod_fit_res = fn(data(i).time, data(i).mod);
    %close(gcf) % comment out line to produce all figures
    fn = str2func(sprintf('fit%dnorm', data(i).T));
    data(i).nmod_fit_res = fn(data(i).time, data(i).nmod);
    %close(gcf) % comment out line to produce all figures
end



%%
clear tt TT pmod pnmod
[tt, TT] = meshgrid(0.1:1:30, 50:5:290);
for i = 1:size(tt,1)
    for j = 1:size(tt,2)
        [temp1, temp2] = LinearInterp(data, tt(i,j), TT(i,j));
        pmod(i,j) = temp1;
        pnmod(i,j) = temp2;
    end
    disp(i/size(tt,1))
end
```

```
%%
figure(1001)
clf(1001)
mesh(tt,TT,pmod)
ylabel('Temperature (^{\circ}C)')
xlabel('Time (min)')
zlabel('Normalized Relaxation Modulus (MPa)')


figure(1002)
clf(1002)
surf(tt,TT,pmod)
ylabel('Temperature (^{\circ}C)')
xlabel('Time (min)')
zlabel('Normalized Relaxation Modulus (MPa)')


%% Nonisothermal Relaxation Model


%Insert Temperature History
%indata = [];

in_t = indata(:,1);
in_T = indata(:,2);
```

```
plot(in_t, in_T)


for i = 1:length(in_t)

    [temp1, temp2] = LinearInterp(data, in_t(i), in_T(i));

    m(i) = temp1;

    nm(i) = temp2;

end


figure(2001)

clf(2001)

subplot(2,1,1)

plot(in_t,in_T)

xlabel('Time (min)')

ylabel('Temperature (^{\circ}C)')

subplot(2,2,3)

plot(in_t,m)

xlabel('Time (min)')

ylabel('Relaxation Modulus (MPa)')

subplot(2,2,4)

plot(in_t,nm)

xlabel('Time (min)')

ylabel('Normalized Relaxation Modulus')
```

A.5.1.1. Linear Interpolation Function


```
function [mod, nmod] = LinearInterp(data, t, T)


    N = length(data);
```

```
Tmin = Inf;

Tmax = -Inf;

for i = 1:N

    if data(i).T < Tmin

        Tmin = data(i).T;

    end

    if data(i).T > Tmax

        Tmax = data(i).T;

    end

end

if Tmin > T || Tmax < T

    error('outside temp range')

end


% find temperatures that we're in between

for i = 1:N-1

    if T >= data(i).T && T < data(i+1).T

        k = i;

        break

    end

end

if T == data(N).T

    k = N - 1;

end


% linearly interpolate

T1 = data(k).T;

T2 = data(k+1).T;
```

```
    mod1 = data(k).mod_fit_res(t);

    mod2 = data(k+1).mod_fit_res(t);


    nmod1 = data(k).nmod_fit_res(t);

    nmod2 = data(k+1).nmod_fit_res(t);



    mod = mod1 + (mod2-mod1)*(T - T1)/(T2 - T1);

    nmod = nmod1 + (nmod2-nmod1)*(T - T1)/(T2 - T1);
end
```

A.6   Tensile Testing

Table A.1: Longitudinal tensile testing sample dimensions and results.

Longitudinal Sample	Average thickness (mm)	Average width (mm)	Average area (mm^2)	F$_{max}$ (N)	σ_{max} (MPa)	E (GPa)
1	7.58	19.98	151.45	10575.2	69.83	25.22
2	6.11	20.11	122.83	11387.6	92.71	25.56
3	6.20	20.19	125.18	12431.0	99.31	26.07
4	6.30	20.14	126.84	13583.8	107.10	27.69
5	6.42	20.03	128.59	11293.5	87.82	26.81
6	6.38	19.95	127.26	9184.2	72.17	27.45
7	6.34	20.12	127.54	12997.9	101.91	27.97
8	6.20	19.93	123.50	11593.5	93.87	27.48
9	7.04	19.88	139.87	13214.0	94.48	24.08
10	6.72	19.93	134.02	12490.7	93.20	24.96
11	6.37	20.15	128.40	13252.5	103.21	26.17
12	6.40	20.05	128.34	13226.5	103.06	27.12
Average	**6.50**	**20.04**	**130.32**	**12102.53**	**93.22**	**26.38**
Standard Deviation	**0.40**	**0.10**	**7.75**	**1269.83**	**11.27**	**1.18**

Table A.2: Transverse tensile testing sample dimensions and results.

Longitudinal Sample	Average thickness (mm)	Average width (mm)	Average area (mm^2)	F$_{max}$ (N)	σ_{max} (MPa)	E (GPa)
W1	6.29	35.67	224.22	1872.27	8.35	2.44
W2	6.26	35.01	219.07	1994.73	9.11	2.18
W3	6.45	35.16	226.64	2399.75	10.59	2.74
W4	6.82	35.21	240.27	2535.84	10.55	2.44
W5	6.67	35.18	234.79	2200.15	9.37	2.58
W6	6.25	35.03	218.84	2406.31	11.00	2.81
S1	6.74	20.15	135.77	1493.26	11.00	2.42
S2	6.76	20.16	136.35	1544.26	11.33	2.50
S3	6.80	20.18	137.25	1565.30	11.40	2.52
S4	6.83	20.11	137.28	1375.99	10.02	2.61
S5	6.79	20.14	136.75	993.91	7.27	2.40
S6	6.76	20.16	136.19	1483.97	10.90	2.74
S7	6.71	20.12	135.07	1084.41	8.03	3.03
S8	6.77	20.13	136.32	984.18	7.22	2.96
Average	**6.64**	**26.60**	**175.34**	**1709.59**	**9.72**	**2.60**
Standard Deviation	**0.21**	**7.46**	**45.30**	**512.64**	**1.44**	**0.23**